Mechanisms of Structure Evolution During Metal Deposition in Lithium- and Sodium-Metal Batteries

Zur Erlangung des akademischen Grades eines
Doktors der Ingenieurwissenschaften (Dr.-Ing.)

von der KIT-Fakultät für Maschinenbau des
Karlsruher Instituts für Technologie (KIT)

angenommene
Dissertation
von

M.Sc. Julian Becherer

Tag der mündlichen Prüfung:	06. Juni 2024
Hauptreferent:	Prof. Dr. Marc Kamlah
Korreferentin:	Prof. Dr. Bronislava Gorr

Abstract

Metal anodes have the potential to increase the energy density of rechargeable lithium- and sodium-based batteries significantly. However, safety concerns hinder their commercialization. They typically exhibit poor Coulombic efficiencies, and during the charging process, they tend to form dendritic deposits, which can result in internal short circuits. In spite of many detailed models of electrodeposition, the behavior of lithium still deserves further research: mechanisms described in literature are often contradictory and their application range is unclear. As alternative to lithium, sodium is promising since it is more abundant and hence cheaper. The goal of this work is to obtain a deeper understanding of the growth of lithium electrodeposits in liquid battery electrolytes and to compare the electrodeposition of lithium and sodium.

Operando light microscopy was used to gain insights into the fundamental mechanisms governing electrodeposition. Compared to other probes such as X-rays or electrons, visible light interferes very little with local electrochemistry, which makes it advantageous to observe metal surfaces underneath liquid electrolytes. A number of battery researchers have used light microscopy for recording overview images without aiming for the highest resolution, e.g., observing objects with the size of several micrometers. The setup developed in progress of this work enables microscopy close to the physical resolution limit of visible light in combination with fast image stacking to achieve an enhanced depth of field. This allows the observation of details of the growing structures, which are typically overlooked at lower resolutions or without image stacking. Although the resolution is maximized, relatively large volumes with statistically representative data can be observed. To study the morphology in further detail, additional scanning electron microscopy images of the same electrodeposits were recorded *post mortem*.

Electrolytes with either 1 M $LiPF_6$ or 1 M $NaPF_6$ in a mixture of dimethyl carbonate (DMC) and ethylene carbonate (EC) were used to compare the deposition and dissolution of lithium and sodium. While lithium showed a relatively stable cycling behavior, this electrolyte did not result in an acceptable cycling behavior for the cells with sodium metal electrodes. This clearly shows that it is not possible to simply transfer knowledge from lithium directly to sodium. Nevertheless, with other electrolyte formulations it was possible to observe the growth of individual sodium needles and a growth from its base was clearly shown for the first time. This growth was very similar to observations that have been made for lithium in the past, which indicates a similar growth mechanism for both metals.

To gain a deeper understanding of the fundamental growth mechanism, lithium was chosen for the further experiments since the cycling of lithium is more stable and reproducible. In the literature, most growth models predict that electrodeposits grow at their tip although experimental observations typically show a growth from the base. In this work, the electrodeposition of lithium was evaluated for various deposition rates between $-0.05\,\mathrm{mA\,cm^{-2}}$ and $-100\,\mathrm{mA\,cm^{-2}}$, which covers all rates relevant for practical battery applications. The results show different growth regimes depending on the rate, where needles, bushes, or accelerated bushes dominate the deposition. All these deposits are based on small crystalline needles and flakes. Little evidence for concentration gradient driven deposition was found. At the highest rate, the cell overpotential indicated an ionic depletion within the electrolyte. Under these conditions, a growth at the tip was expected based on growth models from literature. However, the electrodeposition continued by non-directional bush growth mainly from their insides. These results indicate that the safety of batteries depends less on transport limitations and the depletion of cations, but more on the prevention of the growth of bushes.

For lower deposition rates, the growth of a large number of individual needles and segments in kinked structures was analyzed. Here, the morphology of the evolving deposit reveals that besides electrochemistry, mechanics and crystalline defects play a major role in the growth mechanism. Based on these observations, a growth mechanism that involves the diffusion of lithium atoms from the surface into grain boundaries and the insertion into crystalline defects of the metal is proposed in this thesis. Crystalline defects are a result of plastic deformation and hence mechanical stimulation augments the insertion of lithium. The growth mechanism proposed in this thesis cannot only describe the observations made here, but also helps to explain experimental observations found in literature.

Kurzfassung

Metallanoden können die Energiedichte von Lithium- und Natrium-Ionen-Batterien deutlich erhöhen. Allerdings verhindern Sicherheitsbedenken bisher die Kommerzialisierung von Lithium-Metall-Batterien. Zellen mit Metallanoden haben typischerweise einen geringen Coulomb-Wirkungsgrad und neigen, während des Ladens, zur dendritischen Abscheidung, was zu einem Kurzschluss der Zelle führen kann. In der Literatur gibt es viele Modelle für die Metallabscheidung, allerdings sind die beschriebenen Mechanismen für das Wachstum von Dendriten häufig widersprüchlich und daher umstritten. Trotz jahrzehntelanger Forschung, ist es folglich wichtig, weitere Erkenntnisse über Wachstumsmechanismen zu gewinnen. Natrium ist eine Alternative zu Lithium, da es grundlegend ähnliche Eigenschaften hat, aber deutlich häufiger vorkommt und es daher günstiger ist. Das Ziel dieser Arbeit ist ein besseres Verständnis der Metallabscheidung von Lithium in flüssigen Batterieelektrolyten und der Vergleich der Elektrodeposition von Lithium und Natrium.

Als experimentelle Methode wurde die *operando*-Lichtmikroskopie genutzt, um Erkenntnisse über die grundlegenden Mechanismen der Lithiumabscheidung zu gewinnen. Im Vergleich zu röntgen- oder elektronenbasierten Verfahren beeinflusst sichtbares Licht die lokale Elektrochemie kaum. Daher ist die Lichtmikroskopie sehr vorteilhaft für die *operando*-Beobachtung der Metallabscheidung in flüssigen Elektrolyten. In einigen früheren Forschungsarbeiten zur Untersuchung der Lithium- oder Natriumabscheidung wurde die Lichtmikroskopie verwendet, um Übersichtsbilder aufzunehmen, ohne auf höchste Auflösungen abzuzielen. Damit konnten einige Mikrometer große Objekte aufgelöst werden. Für die vorliegende Arbeit wurde ein Messaufbau entwickelt, welcher Lichtmikroskopie nahe am physikalischen Auflösungslimit in Kombination mit der schnellen Aufnahme von Fokusstapeln für Bilder mit erweiterter Schärfentiefe ermöglicht. So können Details der wachsenden Strukturen beobachtet werden, die bei niedrigerer Auflösung oder geringer Schärfentiefe typischerweise übersehen werden. Das beobachtete Volumen ist trotz der optimierten Auflösung relativ groß und es werden statistisch relevante Daten gewonnen. Nach der *operando*-Lichtmikroskopie konnten die gleichen Abscheidungen im Rasterelektronenmikroskop abgebildet werden, um die abgeschiedene Morphologie im Detail zu untersuchen.

Elektrolyte mit 1 M $LiPF_6$ oder 1 M $NaPF_6$ in einer Mischung aus Dimethylcarbonat (DMC) und Ethylencarbonat (EC) wurden für den Vergleich der Abscheidung und Auflösung von Lithium und Natrium verwendet. Lithium konnte in diesem Elektrolyten relativ stabil zyklisiert werden, für Natrium war dieser Elektrolyt dagegen quasi unbrauchbar. Dieser Vergleich zeigt, dass vorhandenes Wissen nicht direkt von Lithium auf Natrium übertragen werden kann. In anderen Elektrolytzusammensetzungen war es möglich, das Wachstum einzelner Natriumnadeln zu beobachten. Hierbei wurde erstmalig eindeutig gezeigt, dass Natriumnadeln an der Basis wachsen können. Das beobachtete Wachstum ähnelt früheren Beobachtungen für Lithium deutlich, was darauf hindeutet, dass bei beiden Metallen ein ähnlicher Abscheidemechanismus wirksam ist.

Für ein tieferes Verständnis des grundlegenden Wachstumsmechanismus wurde in den weiteren Experimenten Lithium für die Metallabscheidung verwendet, da hier ein stabileres Verhalten und eine bessere Reproduzierbarkeit zu erwarten ist. Modelle in der Literatur sagen meist Spitzenwachstum voraus, obwohl Experimente typischerweise ein Wachstum an der Basis zeigen. In der vorliegenden Arbeit wurde Lithium bei verschiedenen Raten zwischen $-0.05\ \mathrm{mA\,cm^{-2}}$ und $-100\ \mathrm{mA\,cm^{-2}}$ abgeschieden, was alle relevanten Raten für praktische Batterieanwendungen abdeckt. In Abhängigkeit von der Stromdichte kommt es zu verschiedenen Wachstumsarten: je nach Rate dominieren Nadeln, Büsche oder schnell wachsende und poröse Büsche die Morphologie der Abscheidungen. Unabhängig davon bestehen diese Abscheidungen aus kleinen kristallinen Nadeln und kleinen Brocken, welche mit steigender Rate Agglomerate bilden und zu einer Lokalisierung der Abscheidung führen. In den durchgeführten Experimenten gibt es kaum Hinweise auf einen Einfluss des Konzentrationsgradienten im Elektrolyten auf die Abscheidung. Bei der höchsten Rate kommt es zu einem starken Anstieg des Überpotentials, was auf eine vollständige Verarmung im Elektrolyten hinweist. Unter solchen Bedingungen wird auf Grundlage der bestehenden Literatur ein klares Spitzenwachstum erwartet. Allerdings zeigen die Experimente weiterhin ein ungerichtetes Wachstum aus dem Inneren heraus. Diese Ergebnisse deuten darauf hin, dass die Sicherheit von Batterien weniger von Transportlimitierungen des Elektrolyten abhängt als vom Verhindern des Wachstums poröser Büsche.

Eine große Anzahl individueller Nadeln und Segmente geknickter Strukturen wurden bei niedrigen Abscheideraten detailliert analysiert. Die Entwicklung der Morphologie der Abscheidungen zeigt, dass neben der Elektrochemie auch Mechanik und Kristalldefekte eine wichtige Rolle im Wachstumsmechanismus spielen. Basierend auf diesen Beobachtungen wird in dieser Arbeit ein Wachstumsmechanismus vorgeschlagen: Dieser beinhaltet die Diffusion von Lithiumatomen von der Oberfläche in Korngrenzen hinein und eine Einlagerung in das Kristallgitter an Kristalldefekten. Mechanische Belastungen können plastische Verformung und somit Kristalldefekte erzeugen. Daher kann die Einlagerung von Lithiumatomen in das Kristallgitter mechanisch angeregt werden. Der Wachstumsmechanismus, der in dieser Arbeit vorgeschlagen wird, kann nicht nur die hier gemachten experimentellen Beobachtungen erklären, sondern darüber hinaus auch dabei helfen, andere Beobachtungen aus der Literatur besser zu verstehen.

Danksagung

Die vorliegende Dissertation dokumentiert meine Tätigkeit als wissenschaftlicher Mitarbeiter am Institut für Angewandte Materialien – Werkstoff- und Grenzflächenmechanik (IAM-MMI). Im Folgenden möchte ich den Personen danken, ohne die das Gelingen dieser Arbeit nicht denkbar gewesen wäre.

Bei Herrn Prof. Dr. Marc Kamlah bedanke ich mich für die Übernahme des Referats sowie für seine Unterstützung, die wissenschaftlichen Diskussionen und Beratung. Frau Prof. Dr. Bronislava Gorr danke ich für die Übernahme des Korreferats.

Weiter danke ich der Friedrich und Elisabeth Boysen-Stiftung, welche mich im Rahmen des Projektes BOY-161 in den Jahren 2021 und 2022 finanzielle unterstützte und meine Promotion somit ermöglicht hat.

Besonders danken möchte ich meinem direkten Betreuer Dr. Reiner Mönig sowie Dr. Dominik Kramer für freundschaftliche Zusammenarbeit. Die experimentelle Unterstützung sowie die wissenschaftlichen Diskussionen haben sehr großen Anteil am Gelingen dieser Arbeit. Des Weiteren bedanke ich mich bei allen Mitgliedern der Gruppe „Batteriematerialien: Reaktionen und Degradation“ für die tolle Zusammenarbeit, insbesondere gilt dies für meine Bürokollegen Manfred Janzen und Thimo Brendel. Bei Herrn Ewald Ernst und Herrn Edmund Böck bedanke ich mich für das jeder Zeit schnelle Anfertigen von Zellen, Messaufbauten und sonstigen Werkstücken, was die Durchführung meiner experimentellen Arbeit sehr erleichterte. Allen Mitarbeitern des IAM-MMI danke ich für die vielen fachlichen und persönlichen Gespräche, die dazu führten, dass ich eine sehr schöne und lehrreiche Zeit am Institut hatte.

Ich danke meiner Familie, die mich über die langen Jahre meiner Ausbildung unterstützt hat und mich stets darin bekräftigt hat, meinen Weg zu gehen.

Karlsruhe, im Juni 2024 Julian Becherer

Contents

1 Introduction

Lithium-ion batteries (LIBs) were commercialized in 1991 by Sony.[1] Nowadays, the use of LIBs in portable devices, power tools, and electric vehicles is ubiquitous as they outperform competing technologies such as nickel-metal hydride batteries by at least a factor of 2.5 in terms of the specific energy while additionally providing a significantly higher specific power.[2] Although lithium (Li) metal as anode material has the potential to increase the energy density, graphite is used as anode material in commercial LIBs. A few close to commercial secondary batteries with lithium metal anodes were introduced in the early 1990s, but they did not successfully enter the market due to safety concerns or very slow charging rates.[3] Since 2011 the French company Blue Solutions produces commercial cells with a lithium metal anode and a polymer electrolyte, but they can only be operated at elevated temperatures (typically 80 °C).[4] Lithium metal anodes typically have an instable solid electrolyte interphase (SEI), which results in an electrolyte decomposition that does not terminate.[5] Furthermore, cells with lithium metal anodes show often a low Coulombic efficiency and tend to form dendritic deposits during cycling.[6, 7] For the latter, different models and descriptions of the basic growth mechanisms were proposed in literature,[8–12] which are summarized in Section 2.2. The proposed models are often contradictory and so far, there is no general agreement on the relative importance of the underlying mechanisms.

The rising demand for lithium leads to a fear of lithium shortage and hence the interest in alternative technologies such as sodium-ion batteries (SIBs) is increasing.[13] Although sodium provides a smaller gravimetric capacity (1166 mAh g^{-1} vs. 3860 mAh g^{-1}) and a lower cell voltage (−0.33 V) than lithium, it is an interesting alternative as it is the sixth most abundant element in the earth's crust and hence it is inexpensive.[14, 15] The Coulombic efficiency of sodium deposition and dissolution was evaluated for various electrolytes[16–18] and the deposition in different electrolytes was also observed by *in situ* light microscopy[19–21], but only little research was performed to understand the basic mechanisms of the sodium electrodeposition. The mechanisms of sodium deposition and dissolution were studied and compared to lithium, but sodium showed very instable cycling behavior in the ester-based electrolytes used.[22, 23] In contrast, in an ether-based electrolyte, a stable cycling and the growth of ingot-type electrodeposits were observed.[21] Neither for lithium nor sodium, such deposits have been shown before.

In this work, *operando* light microscopy is used to study the fundamental mechanisms of the electrodeposition of lithium and sodium. Of interest are the differences between both metals and the influence of the deposition rate on the growth mechanism.

2 Fundamentals

2.1 Batteries

A battery is a device that consists of one or more electrochemical cells that can be connected in series or in parallel, depending on the desired voltage and capacity of the battery. In such an electrochemical cell, chemical energy can be directly converted to electric energy by the reduction-oxidation (redox) reaction at the positive and negative electrode of the cell. These electrodes are separated by an ionically conductive but electronically isolating electrolyte. The difference of the electrode potentials defines the cell voltage. During discharge, the reduction reaction takes place within the positive electrode while the oxidation occurs at the interface of the negative electrode and the electrolyte. If a battery contains electrochemical cells in which the reverse reactions can be performed reliably, the battery is considered a secondary battery. By definition of the International Union of Pure and Applied Chemistry (IUPAC),[24] the reduction reaction takes place at the cathode and the oxidation reaction at the anode, i.e., during discharge, the positive electrode is the cathode and the negative electrode is the anode, while the positive electrode is the anode and the negative electrode is the cathode when a cell charges. This work focuses on the electrodeposition of the metals, i.e., a reduction reaction at a negative electrode, which would be called cathode by the IUPAC definition. However, in battery terminology, the positive electrode is usually named cathode and the negative electrode is the anode. In the following, the typical battery terminology will be used, and lithium or sodium are called anode materials.

2.1.1 Lithium-Ion Batteries

Figure 2.1 shows a schematic of a LIB during discharge. A copper (Cu) foil is used as current collector at the anode and an aluminum (Al) foil at the cathode. During discharge, lithium atoms deintercalate and oxidize to Li^+-ions at the graphite anode, the Li^+-ions are solvated, and move in a solvation shell through the electrolyte-soaked separator towards the cathode. At the cathode, Li^+-ions remove their solvation shell and intercalate into the cathode

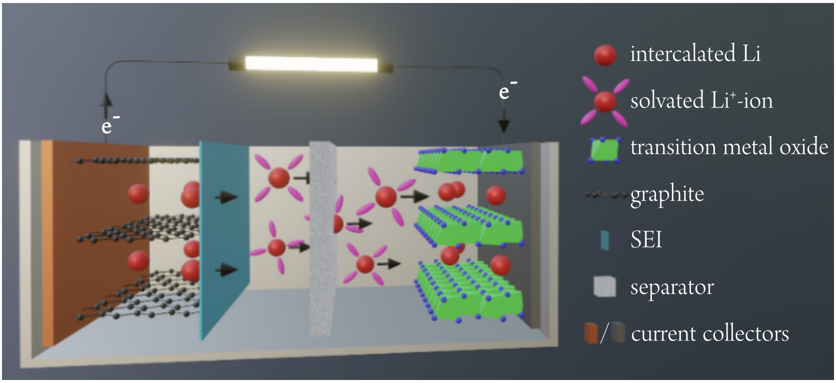

Figure 2.1: Schematic of a Li-ion cell during discharge.

structure where transition metal ions like Ni^{3+} or Ni^{4+} are reduced. While Li^+-ions are transferred through the electrolyte from the anode to the cathode, electrons flow through an external circuit – to power an electrical load (a light in Figure 2.1). To charge such a cell, an external power source is used and the reverse processes occur in the cell. The separator (gray, structured layer in the middle of the cell in Figure 2.1) in LIBs is typically a microporous membrane made from polyethylene (PE) and polypropylene (PP).[25]

A typical electrolyte used in LIBs is lithium hexafluorophosphate ($LiPF_6$) in a mixture of dimethyl carbonate (DMC) and ethylene carbonate (EC). For such an electrolyte, an electrochemical stability window was reported that ranges from 0.8 V to 4.5 V vs. Li^+/Li.[26] A lithiated graphite anode operates well below this range, and depending on the material, a delithiated cathode operates at the upper end of this range. Therefore, the electrolyte is thermodynamically unstable in a LIB cell and the electrolyte is reduced/oxidized at the anode/cathode. This is especially important at the anode where the electrode potential is far outside of the electrochemical stability window. During the initial charge of a cell, the reduction of the solvent and salt result in a film containing various organic and inorganic decomposition products.[27] This film is the so-called SEI, which is shown as blue layer on the graphite anode in Figure 2.1. An ideal SEI (i) is electronically isolating, (ii) has a cationic transference number $t_C = 1$, i.e., is a single ion conductor (iii) has a high conductivity for Li^+-ions, (iv) a uniform morphology and chemical composition, (v) a good adhesion to the anode, and (vi) a high mechanical strength and compliance.[28] Furthermore, the decomposition products should be insoluble in the electrolyte to ensure a stable SEI.

An electrode is typically manufactured by mixing the active material with a binder and a conducting additive. These components are homogenized in a solvent to a so-called electrode slurry, which is coated on the metal foil current collectors. For the commercial electrode production, slot die coating is typically used to coat the slurry onto the current collector.[29] After the coating has dried, it is usually compressed by a process called calendering. Graphite is the industrial standard material for the anode. It has a low intercalation potential between 0 V and 0.25 V vs. Li^+/Li[30] and a specific capacity of 339 mAh g^{-1} with respect to its lithiated state. To increase the gravimetric capacity of the anode, small amounts of silicon (Si) are added to the graphite in some commercially available cells.[31–34] While lithium cobalt oxide ($LiCoO_2$, LCO) was the market-dominating cathode material one decade ago, the production of lithium nickel manganese cobalt oxide ($LiNi_xMn_yCo_{1-x-y}O_2$, NMC) and lithium iron phosphate ($LiFePO_4$, LFP) was growing rapidly in recent years, resulting in a combined market share of approximately 75 % in 2018.[35] Additionally, the annual production of lithium nickel cobalt aluminum oxide ($LiNi_xCo_yAl_{1-x-y}O_2$, NCA) is growing fast.[35] Due to their high energy density and hence the potentially highest mileage, nickel-rich NMC and NCA cathode materials are of particular interest for electric vehicles (EVs).[36, 37] However, Tesla Inc., Ford Motor Co., and Volkswagen AG announced in 2021 that they plan to use LFP cathodes for a large fraction of their production.[38–40] The main advantages of LFP over NMC and NCA are the lower cost, long cycle life, higher safety, and the more environment friendliness of the elements used.[36, 37]

2.1.2 Lithium Metal Batteries and Comparison with Other Anode Materials

Figure 2.2 shows a schematic of a lithium metal battery (LMB). In contrast to a LIB, lithium is not intercalated into and deintercalated from an anode host structure, but is electrodeposited onto and dissolved from a lithium foil. Since the lithium metal anode does not necessarily remain flat during deposition and dissolution, the surface shape and area constantly changes. Therefore, a stable SEI is far more difficult to achieve than on a graphite anode of

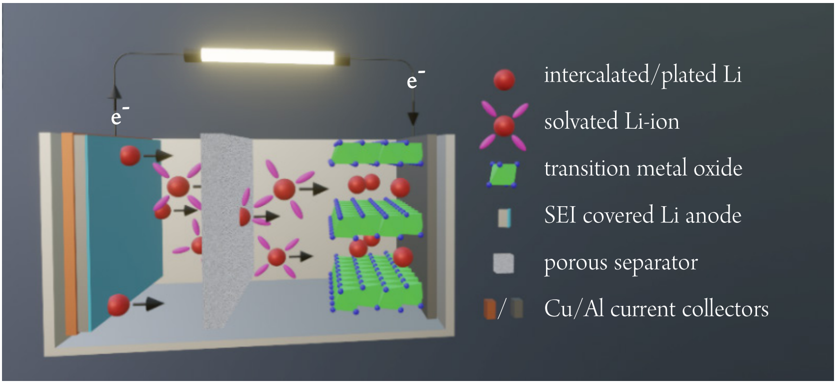

Figure 2.2: Schematic of a lithium metal cell during discharge.

a LIB, which exhibits only about 10 % volume change[41] during cycling.

Lithium metal is the ideal anode material for rechargeable batteries in the sense that it has the lowest electrode potential of −3.04 V vs. a standard hydrogen electrode and a high theoretical gravimetric capacity of 3862 mAh g^{-1}. Although the low density of 0.534 g cm^{-3} is often listed as another benefit, it is rather a drawback since it results in a theoretical volumetric capacity of 2062 mAh cm^{-3}, which is lower than the theoretical values of magnesium, calcium, zinc, or aluminum. Nevertheless, compared to the theoretical values of graphite as used in commercial LIBs, lithium metal anodes provide a more than tenfold higher gravimetric and an almost threefold higher volumetric capacity. Figure 2.3 shows the volumetric and gravimetric capacity of a selection of electrode materials that could potentially be used as anodes in lithium batteries. Commonly, the specific capacities of anode materials are given with respect to the delithiated state. However, the delithiated state of a lithium metal anode (no excess lithium) would result in infinite specific capacities; moreover, it seems more meaningful to compare electrodes with respect to their maximum volume instead of the minimum volume in the delithiated state. Therefore, the specific capacities were calculated with respect to the mass and volume of the lithiated anode materials. To calculate the volumetric capacities the densities found on the Materials Project[42] were used. The average electrode potentials[41, 43] versus Li^+/Li of the anode materials are also given to better compare the materials. Lithium titanate ($Li_4Ti_5O_{12}$, LTO) has the lowest volumetric and

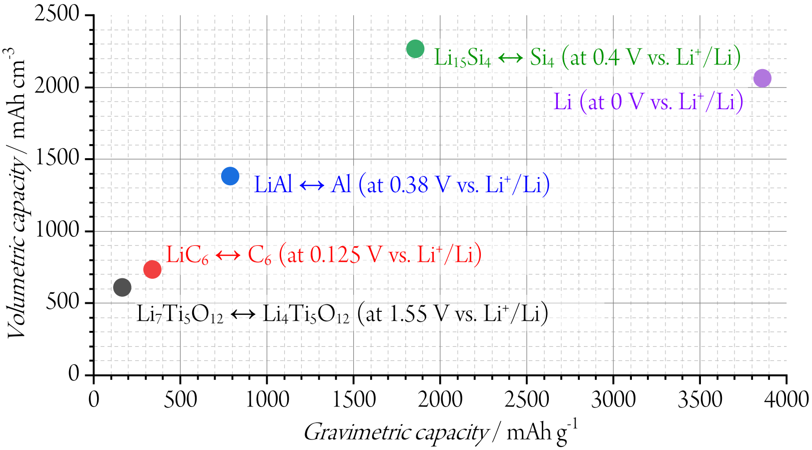

Figure 2.3: Volumetric and gravimetric capacities of various lithiated anode materials for lithium batteries. Volumetric capacities were calculated based on the densities of the lithiated materials from The Materials Project[42]. To better compare the materials, the average anode potentials[41, 43] are stated in the figure.

gravimetric capacity as well as the highest electrode potential of the anode materials shown. Therefore, high specific energy (Wh kg^{-1}) and energy densities (Wh l^{-1}) cannot be obtained with LTO. Nevertheless, LTO anodes are commercialized and used for applications where extreme safety or very long cycle life is indispensable.[31, 43] Since it has the highest volumetric and gravimetric capacity of all alloying-type anodes[41] and a reasonable low electrode potential versus Li$^+$/Li, silicon as anode material for LIBs is of high research interest and is added in small amounts to graphite composite anodes in commercial cells[31–34]. Due to the significantly higher density of $Li_{15}Si_4$ compared to lithium,[42] it even has a higher volumetric capacity than lithium metal. However, silicon expands by 280 % upon full lithiation,[44] preventing the commercialization of silicon anodes and limiting the Si content in Si-graphite composite anodes. Obrovac *et al.*[44] showed that the energy density of a cell hardly depends on the material when an alloying type anode is used and the lithiation is limited to a volume expansion of 100 %. Aluminum expands by approximately by 100 % when fully lithiated and has the advantage that it would not only replace the active material of a graphite anode but also the denser and more expensive copper foil as current collector.[45] Alloy-type anodes are typically plagued by high initial irreversible capacities and rapid capacity fade during cycling.[46] This is attributed to the extreme volume changes during lithiation and delithiation, resulting in cracking and pulverization of the anode material and hence the disconnection of alloy particles.[46] The volume changes also result in cracking of the SEI and consequently a permanent electrolyte decomposition and SEI formation.[46] Stable cycling of a full cell with a LiAl anode has been shown when the anode was only cycled within the lithium solubility range of the β-LiAl phase.[47] The obtained gravimetric capacity of approximately 242 mAh g^{-1} (187 mAh g^{-1} with respect to the mass of the fully lithiated β-LiAl phase) is not enough to significantly increase the specific energy of state-of-the-art LIBs, but when the replacement of the copper current collector is considered, it could result in a similar specific energy by possibly significantly reducing the costs. Since a lithium metal anode needs no host material, it has obviously the highest gravimetric capacity, which is more than twofold the theoretical capacity of $Li_{15}Si_4$. Although the theoretical volumetric capacity of $Li_{15}Si_4$ is by almost 10 % higher, the 0.4 V lower average electrode potential of lithium metal[41] will typically result in a higher theoretical energy density. Even when paired with a lithium manganese nickel oxide ($LiMn_{1.5}Ni_{0.5}O_4$, LMNO) high-voltage spinel oxide cathode, with an average electrode potential of 4.7 V versus Li^+/Li,[31] the cell with a lithium metal anode will have a more than 9 % higher average cell voltage and hence basically the same theoretical energy density as a cell with a $Li_{15}Si_4$ anode. Therefore, lithium metal is theoretically the ideal material to improve both the specific energy and energy density of lithium batteries. However, similar to alloy-type anodes, lithium metal anodes typically have a short cycle life.[48] When no excess lithium is used, the volume change of a lithium metal anode is infinite, but in contrast to alloy anodes, it does not mechanically stress the host material. Nonetheless, in such a configuration it is extremely challenging to obtain a stable SEI since the electrodeposition and dissolution are non-uniform. During charge, the electrodeposits usually do not form a flat film but instead particles/nodules, needles/whiskers/filaments, or moss/bushes form.[48, 49] These uneven deposits are often called dendrites and can pose safety hazards for LMBs.[7, 48, 50] The dissolution of these deposits can occur at their base and result in electronically or physically isolated lithium, so-called dead lithium, which results in capacity loss.[49, 51, 52] Models and descriptions of the growth mechanisms of electrodeposits are introduced in a brief literature review in Section 2.2.

More important than the increase in the volumetric and gravimetric capacity of an anode material is its impact on the energy density and specific energy of the electrochemical cell. Golubkov *et al.*[53] analyzed three consumer LIBs with different cathode materials in the 18650 cell design. Some properties of the three cells with an LCO/NMC blend, an NMC, and an LFP cathode are shown in Table 2.1. The cell capacity and the mass of the cell, the cathode material, and the anode material[1] are the values given by Golubkov *et al.*[53] The volume of the electrodes given by Golubkov *et al.*[53] is based on the thickness of the coating and hence includes the pore volumes of both electrodes. To exclude the pore volume, the volume of the cathode and anode materials shown in Table 2.1 are calculated from the

Table 2.1: Properties of three 18650 consumer LIBs with different cathode material, which were analyzed by Golubkov *et al.*[53] and the weight and volume of a lithium foil with the capacity of the cell in the last two rows.

		LCO/NMC (2:1)		NMC		LFP	
Cell capacity		2600 mAh[53]		1500 mAh[53]		1100 mAh[53]	
Cell mass		44.3 g[53]		43.1 g[53]		39.0 g[53]	
Cathode material	Mass	18.3 g[53]	41 *wt*%	11.3 g[53]	26 *wt*%	9.7 g[53]	25 *wt*%
	Volume	4.0 cm^3	24 *vol*%	2.6 cm^3	16 *vol*%	2.8 cm^3	17 *vol*%
Anode material	Mass	8.1 g[53]	18 *wt*%	6.2 g[53]	14 *wt*%	5.2 g[53]	13 *wt*%
	Volume	3.6 cm^3	22 *vol*%	2.8 cm^3	17 *vol*%	2.3 cm^3	14 *vol*%
Lithium metal anode	Mass	0.7 g	2 *wt*%	0.4 g	1 *wt*%	0.3 g	1 *wt*%
	Volume	1.3 cm^3	8 *vol*%	0.7 cm^3	4 *vol*%	0.5 cm^3	3 *vol*%

---

[1] Golubkov *et al.*[53] use the terms cathode and anode active material, but neither binder nor conductive additives are considered in the composition of the cell. Since it can be assumed that binder and conductive additives are used in the electrodes of these commercial cells, the terms cathode and anode material are used here.

weight of the coating, the densities of the active materials, and the density of a binder and conductive additive mixture of 10 *wt*% as described below.

The densities of the active materials are 4.92 g cm^{-3},[42] 4.7 g cm^{-3},[54] 3.6 g cm^{-3},[54] and 2.3 g cm^{-3}[54] for LCO, NMC, LFP, and graphite, respectively. The densities of the often used binder polyvinylidene fluoride (PVDF)[55] and carbon black powder as conductive additive (e.g., Super P® Li[56]) have similar densities of about 1.8 g cm^{-3}. For simplicity, a density of 1.8 g cm^{-3} and a content of 10 *wt*% of the binder and carbon black mixture is assumed for all electrodes. The mass fractions are calculated with respect to the cell mass and the volume fractions with respect to the 16.5 cm^3 volume of an 18650 cell. The last two rows show the mass and the volume of a lithium metal anode with the cell's capacity, which would result in 100 % excess lithium since the cathode is in the fully lithiated state when manufactured. For simplicity, the mass and the volume fractions of the metal anode are calculated with respect to the original cell mass and volume although a cell with a lithium metal anode would be lighter.

When comparing the cathode and anode material of all cells, it becomes clear that the cathode dominates the cells weight, while anode and cathode have similar influence on the volume. The mass fraction of the cathodes in these cells varies between 25 *wt*% and 41 *wt*% and is in all cases approximately twice the mass fraction of the anodes. The volume fractions of all electrodes vary between 14 *vol*% and 24 *vol*% but are very similar for cathode and anode in each cell. Therefore, the specific energy would mainly benefit from improvement at the cathode, while improvements at both electrodes could have similar influence on the energy density.

The benefits, with respect to the energy density and specific energy, of replacing a graphite anode with a lithium metal anode are estimated in Appendix A.1 for the cell with the LCO/NMC blend cathode. With the assumptions made in this estimation, the energy density would increase by approximately 27 % and the specific energy by 30 %. This example shows that, although the cathode dominates cell mass, lithium metal anodes can result in a significant increase not only of the energy density but also the specific energy. The specific energy increases even more than the energy density since the gravimetric capacity is more than tenfold higher, while the volumetric capacity increases by slightly less than three times. Since the study of Golubkov *et al.*[53] was published in 2014, the analyzed cells are not the state of the art anymore in 2023. Newer commercialized cells already have electrodes with higher capacities, e.g., due to higher nickel content in the cathode, small amounts of silicon in the anode, or optimized electrode designs. Therefore, replacing the anode in a newer 18650 cell will most likely result in lower improvements of the energy density and the specific energy. However, in other cell formats, such as pouch cells, large prismatic cells, or 4680 cells, which were introduced by Tesla Inc. in 2020[57, 58] and have an eight times larger volume than 18650 cells, the cell housing contributes less to the cell's mass and volume. In these cell designs, the energy density and specific energy benefit more from improvements of the electrodes. The impact of lithium metal anodes in prismatic cells with LFP cathodes was recently studied by Sripad *et al.*[38] They simulated the benefit of replacing the graphite anode with a lithium foil with a thickness of 20 µm to 100 µm and found improvements of the specific energy in the range of approximately 30 % to 35 %, depending on the thickness of the foil. The increase in the energy density varies between 5 % and 25 %. Due to the low density of lithium, the energy density strongly depends on the amount of excess lithium, while it has only a slight influence on the specific energy. The LFP cathodes used in these simulations have an area specific capacity of 4.49 mAh cm^{-2} (supplementary data of Sripad *et al.*[38]), which is the area specific capacity of a lithium foil with a thickness of approximatly 22 µm. Therefore, the variation of the thickness of the foil between 20 µm and 100 µm corresponds to an variation of the excess lithium between 90 % and 450 %. For 100 % excess lithium, the simulations for large prismatic cells and LFP cathodes result in very similar improvements as estimated for the 18650 cell with LCO/NMC blend cathodes in Appenix A.1. It is very clear that lithium metal anodes could significantly contribute to the increase of energy density and specific energy of lithium batterys when conventional cathodes are used, but especially for improvements of the energy density the excess lithium needs to be limited. The benefits of lithium metal anodes could be even higher in combination with sulfur or air cathodes in lithium-sulfur or lithium-air batteries.

2.2 Models for the Growth of Electrodeposited Metals

Many different models for the basic growth mechanisms of lithium dendrites have been proposed in the literature. A selection of these models is summarized in the following. Although the term dendrite originally describes a multi-branched structure and lithium deposits often do not show branching, the term dendrite is widely used in the literature for different forms of lithium deposits, e.g., whiskers. Therefore, this term will also be used in this work.

2.2.1 Transport Limitations of the Electrolyte

In 1990 Chazalviel[8] showed that metallic electrodeposition in dilute salt solutions is governed by the space charge created by the depletion of the active species in the vicinity of the electrode on which the metal is deposited. It was shown that the tips of the deposits grow at the velocity of the anions, which is determined by their mobility and the electric field in the neutral region of the electrolyte. The dendritic growth in lithium polymer cells was studied in the framework of Chazalviel's model.[59, 60] Brissot *et al.*[59] observed lithium dendrites to grow close to the velocity predicted by Chazalviel at high current densities and a large inter-electrode distance. Their cell potential exhibited Sand's behavior[61]: After the Sand time τ_{Sand}, the cationic concentration in the vicinity of the negative electrode drops to zero and the electrolyte becomes ionically depleted. The cationic concentration can only drop to zero if a limiting current density is exceeded. This limiting current density can be calculated by $J_{\text{lim}} = \frac{2 z_C c_0 F D}{L\,(1\text{-}t_C)}$[10, 62, 63] with the cationic charge number z_C, the initial salt concentration in the electrolyte c_0, the Faraday's constant F, the salt diffusion coefficient D, the inter-electrode distance L, and the cationic transference number t_C. If the current density j exceeds the limiting current density J_{lim}, the Sand's time can be calculated with $\tau_{\text{Sand}} = \pi D \left(\frac{z_C c_0 F}{2j\,(1\text{-}t_C)}\right)^2$[62–64]. In the experiments of Rosso *et al.*,[60] Sand behavior was not expected due to their lower current densities but dendritic growth was still observed at onset times similar to Sand's time.[60] These surprising results were attributed to local inhomogeneities at the surface of the electrode and hence a non-uniform distribution of the concentration.

Barton and Bockris[65] studied the growth of silver dendrites and showed that growth is preferred at the tip of protrusions. They explained this by the fact that spherical diffusion is faster than linear diffusion. At the tip of a protrusion, a spherical diffusion layer can form around the tip. In such a layer, the active species can diffuse to the tip from all directions, while the diffusion occurs only from one direction in a diffusion layer on a flat surface. Therefore, more electrolyte volume per area of growing surface is available to deliver the ions required for the growth. This model was later adapted for lithium polymer cells[10] and lithium deposition in liquid electrolytes[66]. In contrast to Chazalviel's model based on the ionic concentration gradient, dendritic growth caused by spherical diffusion can occur at current densities below the limiting current density at which the cationic concentration drops to zero at the negative electrode.

2.2.2 Non-Uniformity of the SEI

Cohen *et al.*[9] attributed the formation of lithium dendrites to the non-uniformity of SEI. Due to the lower ionic conductivity of the SEI compared to the liquid electrolyte, the metal will preferably deposit at locations with cracks in the SEI, under thin SEI layers, and regions in which the non-uniform SEI has the highest ionic conductivity. Wood *et al.*[67] also described fractured and thinned SEI layers as dominant factors for the deposition and dissolution behavior of lithium.

2.2.3 Transport Limitations Within the Solid Electrolyte Interphase

In Akolkar's group[68, 69], the transport limitations within the SEI have been studied in recent years. They compared the onset time of dendritic growth from various experiments found in literature with a lower bound of the calculated Sand's time within the liquid electrolyte and found that the onset times are one to two orders of magnitude too small compared to the calculated values.[69] A model based on the multi-phase diffusion through the liquid electrolyte and the SEI was used to predict the onset time more precisely.[68, 69] The simulations of the concentration profiles at a current density of $-0.5\,\mathrm{mA\,cm^{-2}}$ show that the concentration at the Li-SEI interface can drop to zero when the SEI has grown thick enough (~20 nm), although the concentration at the electrolyte-SEI interface has hardly changed.[69] Since the Li^+ concentration drops to zero at the Li-SEI interface, they expect the onset of dendritic growth within the SEI similar to the model from Chazalviel in liquid electrolytes (see Section 2.2.1).[68] The subsequent dendrite growth results in a rupture of the SEI and the lithium is directly exposed to the liquid electrolyte that is not depleted.[68] The growth after the rupture of the SEI is only vaguely described by the exposure of lithium metal to the electrolyte in the work of Akolkars's group.[68, 69] Due to the faster kinetics of the SEI-free lithium surface, this will result in a growth similar to the growth mechanism based on the non-uniformity of the SEI as proposed by Cohen *et al.*[9] and described in the previous section. Since this model describes the growth within a few tens of nanometers thick SEI layer, the growing structures have to be very small. Therefore, the model could be considered rather as nucleation model than a growth model.

Chen *et al.*[70] used electrolytes with various contents of lithium nitrate ($LiNO_3$) to obtain different ionic conductivities in the SEI and found a spherical electrodeposition for high ionic conductivities, while lower conductivities resulted in needle-like deposits. They propose that a diffusion-controlled process in the slow SEI results in the depletion of Li^+-ions at the Li-SEI interface and the growth of needles, while reaction-controlled process generates spherical electrodeposits when the SEI has a higher conductivity.[70]

2.2.4 Growth by Release of Mechanical Stress

Yamaki *et al.*[11] were the first group that reported that lithium deposits grow from the base and not at the tip and compared the growth mechanism to that of tin whiskers. They assumed that the non-uniform deposition of lithium under the SEI induces stress to the lithium anode that causes the transport of lithium atoms within the electrode. The SEI breaks at a certain point due to stresses in the electrode caused by the SEI confinement and lithium is extruded through these cracks in the form of whiskers.[11] Also a more recent work describes the growth of lithium whiskers by a similar mechanism.[71]

2.2.5 Insertion at Defects

In a previous work of our group, it was shown by Steiger *et al.*[12] that the insertion into lithium filaments can occur at different sites. Filaments can grow from the base, at kinks, or in a region close to the tip and even directly at the tip. It was suggested that the insertion at defects is the dominant growth mechanism. Different types of defects that can enhance the deposition were considered: SEI defects, defects in the crystal structure such as grain boundaries (GBs), and contaminations that could act as nucleation sites.[12] To support the defect-based insertion mechanism, Steiger *et al.*[72] compared the electrochemical deposition of lithium with lithium deposition by thermal evaporation in vacuum. In both cases, similar needle-like deposits evolve. This shows that neither an electrolyte nor an SEI are necessary for lithium to form needle-like deposits, which indicates that there is an intrinsic tendency of lithium to form such structures.

The importance of crystalline defects on the cycling behavior of lithium metal has also been suggested by other groups. Yamaki *et al.*[11] proposed that lithium is deposited into crystalline defects of whiskers after a long time of electrodeposition when the electrode is covered with whiskers, grown by the extrusion mechanism (see Section 2.2.3), and the Li^+-ion transport to the electrode surface becomes obstructed. Gireaud *et al.*[73] showed that lithium dissolution occurs preferentially at slip lines at the bulk surface, which they explained by the higher interfacial energy at these defect lines. The subsequent electrodeposits nucleated inside of surface cracks, generated by the dissolution along the slip lines.[73] Rulev *et al.*[74] observed that lithium grains grow from their "root" when lithium was deposited onto a lithium foil and attributed this observation to the diffusion of lithium atoms into GBs.

2.3 Countermeasures Against Dendrite Growth

Various approaches to suppress the growth of dendrites and hence to improve the cycle life, the Coulombic efficiency, and safety of LMBs are proposed in the literature. A selection of these approaches is summarized in this section. To obtain an overview on the multitude of suggested options, they are categorized into topics (headings) in the following text. It should be noted that such a classification can be sometimes useful and straightforward, but may be difficult in other cases. For example, an electrolyte component present in low concentration is usually called additive. If it is present in higher concentration, it might be difficult to distinguish between an organic additive and a (co)solvent or between an in inorganic additive and a conducting salt.

2.3.1 Additives for Conventional Liquid Electrolytes

Many of the approaches to suppress the formation of dendrites are based on the modification of the liquid electrolyte. One way of modification is the admixture of an additive to a conventional carbonate-based electrolyte. Frequently used additives for LMBs are fluoroethylene carbonate (FEC)[75, 76] and vinylene carbonate (VC),[75, 77] which are also used in commercial LIBs. Another additive that has been shown to significantly increase the performance of LMBs is $LiNO_3$.[78–81] $LiNO_3$ can improve the performance of cells with conventional carbonate-based electrolytes, but due to its low solubility in carbonates, it is more frequently used in ether-based electrolytes.[78, 79] All of these additives are so-called film-forming additives and modify the SEI. An effective film forming additive reacts with the lithium anode faster than the other electrolyte components to form a stable interface between the lithium metal and the electrolyte.[7] FEC as additive results in a lithium fluoride (LiF)-rich SEI film that contributes to a dense and uniform morphology of the lithium electrodeposits.[76] The fast polymerization of FEC and VC can result in a more stable SEI film than the short oligomer products formed without the additives.[82] Michan *et al.*[83] found almost the same reduction products when the reaction of FEC and VC were compared. The only difference was the presence of LiF when FEC was used. They proposed a reduction of FEC to LiF, VC, and hydrogen and a subsequent polymerization of VC. $LiNO_3$ forms an SEI that contains lithium nitride (Li_3N) and lithium oxynitrides (LiN_xO_y).[78–80] Li_3N has a high ionic and a low electronic conductivity,[84, 85] and nitrides are very stable against lithium metal.[86] These properties result in superior SEIs when $LiNO_3$ is used as additive. Laboratory cells often have excessive amounts of lithium and electrolyte. Since lithium metal anodes have an infinite volume change during cycling, they should be cycled in a way that they only grow and shrink in thickness to allow for a stable and non-changing SEI that only moves up and down. When the electrodeposition is not homogenous, the SEI may permanently fracture and lithium reacts with the additives. While relatively large amounts of additives in the large electrolyte volume in a lab cell may enable hundreds of cycles, the additives can easily deplete after a few cycles in cells with technically relevant electrolyte-to-capacity ratios.

Ding *et al.*[87] proposed additives with a very different working principle: In low concentrations, specific cations such as Cs^+ (cesium) have a lower reduction potential than lithium. When the deposition potential is below the reduction potential of lithium but above of the reduction potential of the additive, only lithium will be deposited and form protrusions. According to Ding *et al.*, the stronger electric field at edges and protrusions results in an accumulation of the additive cations at these tips without their electrodeposition. They suggest that these cations form an electrostatic shield that prevents deposition at the tips.[87] The idea of this additive is based on the assumption that dendrites and needles would grow at their tips; then reducing the electric field at tips and protrusions might result a flat film.[87] Less than two years later, the same group showed that the cesium hexafluorophosphate ($CsPF_6$) additive modifies the SEI and enhances the formation of LiF already at potentials above 2 V vs. Li^+/Li and hence in the initial SEI layer.[88] Therefore, $CsPF_6$ acts as film-forming additive and it is difficult to differentiate which process is responsible for the enhanced cycling performance. Rulev *et al.*[89] used indifferent (non-electroactive) cations to nearly fully exclude electromigration currents and found no influence on the whisker-like electrodeposits. Therefore, the suppression of dendrites with $CsPF_6$ as additive is most likely not related to a shielding mechanism but rather related to other effects,[89] e.g., the aforementioned enhanced formation of LiF.[88]

2.3.2 Electrolyte Composition

Not only additives can influence the composition of the SEI and the stability of LMBs, also the lithium salt and the solvent of the electrolyte have a strong influence. Lithium salts that are considered to form a good SEI are $LiPF_6$, $LiAsF_6$ (lithium hexafluoroarsenate), $LiN(CF_3SO_2)_2$ (lithium bis(trifluoromethanesulfonyl)imide, LiTFSI), and $LiB(C_2O_4)_2$ (lithium bis(oxalato)borate; LiBOB).[90] Another widely used salt is $LiN(FSO_2)_2$ (lithium bis(fluorosulfonyl)imide, LiFSI) since it results in a LiF-rich SEI.[91, 92] Ether solvents have typically a higher reduction stability than carbonate solvents and hence ether electrolytes have a better intrinsic stability against lithium metal.[90, 91] However, ether solvents typically have a lower oxidation stability.[90, 91] This is rather unproblematic for cells with low voltage cathodes such as conversion-type cathodes (e.g., sulfur or oxygen). Some ether solvents with rather high oxidation stability may even be used in cells with LFP cathodes, but they are typically not suitable for high-voltage materials such as NMC, NCA, or LMNO. In this thesis, the electrodeposition of lithium and sodium is studied and hence the oxidation stability of the electrolyte is not relevant. However, using electrolytes with high reduction stability for an improved performance of the lithium anode but without considering the oxidation stability may be not very beneficial for possible future use in full cells. Therefore, both the reduction as well as the oxidation stability should be considered when electrolytes are optimized. Miao *et al.*[93] showed an ether-based electrolyte with a high oxidative stability when 1,4-dioxane (DX) was used as co-solvent. They reported an anodic stability of ~4.87 V vs. Li^+/Li for a 1 M LiFSI in 1,2-dimethoxyethane (DME)/DX (2:1) electrolyte, while only ~3.58 V vs. Li^+/Li were reached for 1 M LiFSI in the more commonly used DME/1,3-dioxolane (DOL) solution. They used LFP cathodes for full cell experiments and did not test the electrolyte with high-voltage electrodes.[93] Another approach to improve the electrochemical stability window of ether-based electrolytes are highly concentrated electrolytes. In a highly concentrated electrolyte, there is only a limited number of free ether molecules, and ether molecules coordinated to Li^+ cations can significantly lower the highest occupied molecular orbital (HOMO) level and thus enhance the oxidative stability.[94–96] Equimolar mixtures of LiTFSI with triethylene glycol dimethyl ether (triglyme) and LiTFSI with tetraethylene glycol dimethyl ether (tetraglyme) have significantly higher oxidative limits than LiTFSI in lower concentrations in these ether solvents.[95] Especially the triglyme electrolyte could significantly enhance the cycling stability with the higher concentration when lithium metal was paired with an LCO cathode.[95] Jiao *et al.*[96] used a highly concentrated dual-salt electrolyte with 2 M $LiBF_2C_2O_4$ (lithium difluoro(oxalato)borate, LiDFOB) and 2 M LiTFSI in DME and significantly outperformed highly concentrated electrolytes with both individual salts in Li||NMC cells. The LiDFOB was used for its ability to suppress the oxidation of the electrolyte at the cathode, but due to the low Coulombic efficiency in cells with LiDFOB, LiTFSI was added.[96] In addition to the enhanced oxidation stability, highly concentrated electrolytes can also (i) improve the reduction stability at the anode, (ii) form thin and compact SEI films, and (iii) result in a denser morphology of the electrodeposits.[94] Therefore, they are used in many experimental studies with lithium metal anodes and show enhanced cycling performance in various salt-solvent combinations.[95–100] In spite of these benefits, the use of highly concentrated electrolytes for practical applications is difficult. They typically have various disadvantages such as poor processability due to their high viscosity and poor wettability, extremely low ionic conductivity at low temperatures, and higher costs.[101–103] To overcome these challenges but retain the benefits of concentrated electrolytes, Chen *et al.*[102] proposed the concept of localized high-concentration electrolytes. For such an electrolyte, a highly concentrated electrolyte is mixed with a diluent that has the following characteristics: (i) an electrochemical stability window that is similar or wider than that of the concentrated electrolyte, (ii) does not dissolve the salt, and (iii) has a good miscibility with the solvent and the solvated L^+-ions.[102] They used a 5.5 M LiFSI in DMC electrolyte and diluted in bis(2,2,2-trifluoroethyl) ether (BTFE) to a 1.2 M-solution and even improved the performance of the 5.5 M LiFSI in DMC electrolyte in Li||NMC cells.[102] Similar results have been demonstrated for other electrolyte-diluent combinations, including a combination with a fire-retardant electrolyte to increase the safety of LMBs.[103–105]

2.3.3 Preformed Artificial SEI

Most of the modifications of the liquid electrolyte aim on enhancing the properties of the SEI. An alternative to modify the metal-electrolyte interphase is the formation of a protective layer or so-called artificial SEI before a cell is assembled. Various methods to form such layers are proposed in literature. In electrochemical pretreatments, the formation cycles of the lithium anodes are performed in separate cells with electrolytes that can differ from the electrolyte of the final cell. This has the advantage that film-forming additives, solvents, salts, and concentrations can be chosen without considering the rate performance, long-term cycling, or the stability of the cathode.[7] An example for this strategy shows a superior cycling performance of Li||NMC cells with a conventional carbonate-based electrolyte without additives, when the anode was cycled for one cycle in a symmetrical cell with in a LiTFSI-DOL/DME electrolyte with $LiNO_3$ and lithium polysulfide (Li_2S_5) as additives.[106] Although such an approach can be beneficial, scaling up such a process for commercialization may be challenging, especially if washing steps are required to remove components, which should not contaminate the final electrolyte. A possibly more feasible process could be the chemical reaction of a lithium anode with a gas or liquid before a cell is assembled. A Li_3N layer on lithium can be obtained by the direct reaction of lithium and nitrogen and results in an improved cycling behavior.[107, 108] The reaction of lithium in a polyphosphoric acid solution results in a dense lithium phosphate (Li_3PO_4) layer, which improved the cycling stability of Li||LFP cells with a conventional carbonate electrolyte.[109] Furthermore, various coating methods are used for physical pretreatments. An example for surface films coated in physical pretreatment that increase the cycle stability of lithium anodes are aluminum oxide (Al_2O_3) films. They can be beneficial as porous surface films obtained with spin-coating[110] or as thin and dense films from atomic layer deposition.[111, 112]

2.3.4 Solid Electrolytes

Nowadays, there is a focus on the research on solid electrolytes to enable the use of lithium metal anodes. Compared to liquid electrolytes, solid-electrolytes typically have a better thermal stability, some of them are non-flammable, and exclude the risk of leakage.[113] Furthermore, solid electrolytes with a high shear modulus are reported to suppress the growth of dendrites.[114] Solid electrolytes can be classified as inorganic electrolytes (oxides and sulfides), organic polymer electrolytes, and hybrid solid electrolytes with organic and inorganic components. Inorganic solid electrolytes are typically single ion conductors ($t_C \approx 1$) and hence do not exhibit losses caused by concentration polarization,[113, 115, 116] which means that they cannot show Sand's behavior as described in Section 2.2.1. Oxide electrolytes show a good stability against air, water, and high temperature, but have rather low ionic conductivity (typically between 10^{-6} S cm^{-1} and 10^{-3} S cm^{-1}), high interfacial resistance, poor wetting abilities, and can hardly accommodate volume changes due to their low compliance.[117] In contrast to the low ionic conductivity of oxide electrolytes, some sulfide solid electrolytes reach and even surpass the conductivity of conventional liquid electrolytes for LIBs (in the order of 10^{-2} S cm^{-1}[118]).[117] Another benefit of sulfide electrolytes is their low strength and high ductility that enables better interfaces to the electrodes than the brittle oxide electrolytes.[115] However, their bad stability against air and water complicates the preparation conditions.[117] Furthermore, in contact with lithium metal, the solid sulfide electrolytes typically decompose to lithium sulfide (Li_2S), which has a poor conductivity and even thin passivation layers can significantly increase the interfacial resistance.[113, 119, 120] On the cathode, the solid sulfide electrolytes can also form a highly resistive decomposition interphase when the solid electrolyte is oxidized.[121] Additionally, the contraction of cathode particles can result in contact loss between electrolyte and cathode.[121] The decomposition of the electrolyte at both electrodes is in contradiction to the large electrochemical stability window obtained by cyclic voltammetry (CV) for various solid sulfide electrolytes.[122–126] Zhu *et al.*[127, 128] and Richards *et al.*[129] used *ab initio* calculations to investigate the electrochemical and chemical stability of various solid electrolytes and their interfaces with different electrodes. They found electrochemical stability windows that are considerably smaller than the ones obtained by CV. Especially for solid sulfide electrolytes, small stability rages were found, which are even significantly smaller than those of conventional liquid electrolytes (e.g., 1.71 V to 2.14 V for $Li_{10}GeP_2S_{12}$[127]).[127, 129] The larger stability windows that were experimentally obtained may be a combination of the intrinsic electrochemical window of the solid electrolyte plus the electrochemical stability window of the interphases at both electrodes, which are similar to the SEI in LIBs with liquid electrolytes.[127] Due to the instability of the inorganic solid electrolytes at least at the potential of one electrode, the stability and the properties (no electronic and high ionic conductivity) of the decomposition products in the electrode-electrolyte interphase is crucial to improve the performance of solid-state batteries. On the cathode side, where various electrode materials can be used, each combination of electrode and electrolyte may result in different decomposition products and hence a multitude of interphase compositions is possible.[128, 129] The coating of artificial interphases with the desired properties is a promising method to improve the performance of solid-state batteries.[127, 128] Nevertheless, for all inorganic solid electrolytes, the thermodynamic compatibility, interfacial instability, and insufficient ability to mechanical accommodate volume changes hinders the use for practical applications.[113]

Compared to inorganic solid electrolytes, organic polymer electrolytes have a better interface contact, processability, economic availability, and a decent stability against lithium.[130] However, especially the often used polyethylene oxide (PEO) electrolytes exhibit an electrochemical stability window that is limited to approximately 4 V, which is too low for high-voltage cathodes, and at room temperature, they have conductivity that is limited to about 10^{-3} S cm^{-1}.[117, 130] The ionic conductivity can be significantly improved when the polymer is soaked by an organic liquid electrolyte to form a gel electrolyte or when a cell with a polymer electrolyte operates at elevated temperatures.[131] In both cases the mechanical strength of the electrolyte is reduced, which is detrimental for the ability to suppress the growth of dendrites.[131] The mechanical strength and the ionic conductivity of polymer electrolytes can be increased when ceramics are added to form a hybrid composite electrolyte. It is known that ceramic additives in PEO electrolytes reduce the formation of crystalized phase, which enhances the ionic conductivity and hence even inactive particles such as Al_2O_3 can be used.[132] Nevertheless, inorganic solid electrolytes such as lithium lanthanum zirconium oxide (LLZO, $Li_7La_3Zr_2O_{12}$) as additive typically result in a superior improvement compared to inactive fillers.[133, 134] Yang *et al.*[134] found that LLZO nanowires result in significantly higher ionic conductivities than LLZO nanoparticles and that only 5 *wt*% of LLZO content result in the best ionic conductivities. The dominant diffusion pathways of

Li^+-ions in such hybrid electrolytes can be mainly through the ceramic particles when high filler contents are used[135] or along the polymer-ceramic interface for low filler content in form of nanowires[134]. The hybrid composite electrolytes improve the mechanical stability and the ionic conductivity compared to pure polymer electrolytes, and they exhibit better interface contact to the electrodes and can better accommodate volume changes when compared to inorganic solid electrolytes. However, compared to solid sulfide electrolytes and liquid electrolytes, their ionic conductivity at room temperature is still significantly lower.[117]

2.3.5 Deposition into Host Frameworks

3D skeletons with high surface area and large pore volumes are used as current collectors to reduce the local current density and accommodate volume changes during cycling.[113, 131, 136] The lower local current densities in these frameworks can reduce the voltage hysteresis, increase the Coulombic efficiency, and result in longer cycle life.[113] The material of such an framework should have high mechanical and electrochemical stability as well as low density to enable high energy densities.[131] For a more homogeneous deposition inside the framework, lithiophilic coatings[137–141] or particles as nucleation seeds[142, 143] can be applied to the host materials. The most commonly used host structures are carbon-based or metallic,[113, 134] but also non-conductive hosts with infused molten lithium have been used.[140] Non-conductive frameworks have the advantage that a deposition on top of the framework is not possible but the deposition has to start at the bottom of the host structure. An alternative to ensure the growth from the bottom of the framework is a framework with a gradient of the interfacial activity, e.g., stacked frameworks with a lithiophilic coating on the bottom layer and a passivating coating on the top layer creates such a gradient.[141] With a growth from the bottom inside a framework, the risk of dendrites short circuiting a cell can be mitigated. However, for conducting frameworks, a large surface area will result in more side reactions, more SEI, and a higher risk of depletion of the electrolyte.[131] Often, it is assumed that a large surface area and the resulting low local current densities should be beneficial because it is assumed at the same time that dendrites grow due to transport limitations in the electrolyte and due to faster transport to the tips.[7, 144–147] If these underlying assumptions (described in detail above in Section 2.2.1 “Transport Limitations of the Electrolyte”) are not valid, e.g. if whiskers grow at low current densities and from their base, it has to be questioned how successful the large-area approach can be. Furthermore, the fundamental assumption that an increased electrode surface area could influence the transport limitations within the electrolyte by prolonging Sand's time seems faulty. For a flat electrode, its surface area is equivalent to the electrolyte cross section. Using a porous host framework to increase the electrode surface, reduces the local current density on its surface, but it does not affect the current density within the electrolyte between the electrodes. Therefore, the cross section of the electrolyte will limit the transport of Li^+-ions between the electrodes and the larger surface area of the porous host framework may hardly influence the limiting current density. Host frameworks may be beneficial for the nucleation of lithium electrodeposits and can prevent volume changes, but the lower local current density that is present due to the increased surface area cannot prevent dendrites by prolonging Sand's time.

2.3.6 Mechanical Suppression

External pressures applied perpendicular to the electrode surface result in longer cycle life and a denser electrodeposition of lithium.[73, 148–155] Typically, the highest applied pressures are in the range between 0.7 MPa and 2.3 MPa[73, 150–154] and pressures up to approximately 1 MPa lead to a better performance in all of these studies, while a further increase of the pressure worsens the performance in some cases but further improves it in other cases. The worse performance of cells with higher externally applied pressures[150, 155] and higher internal pressure due to the growth of the lithium metal anode upon cycling in constant volume cylindrical cells[156] has been attributed to the deformation of the separator. It was shown for LIBs that compressive stresses result in an increase of the internal resistance and capacity fade that has been attributed to the inhibited ion transport through the deformed pore network.[157, 158] Hirai *et al.*[149] applied higher external pressures of up to approximately 12.5 MPa to cells with various electrolyte formulations. Even for the highest applied pressures, they found an improved performance for most of the electrolytes used. However, they typically found the most significant improvement of the cycling efficiency in cells with an applied pressure of 2.5 MPa compared to cells with no pressure applied (no step in between), which is in agreement with other experimental studies where the most significant impact is found for low pressures.[73, 148, 150–152, 155] Different mechanisms for the improved cycle life due to compressive stresses have been suggested: (i) The pressure results in enhanced contact between lithium grains and at the interface of lithium and current collector. Therefore, lithium is not easily isolated during electrodissolution.[149] This is supported by an experiment where a cell without pressure failed during cycling and the capacity could be recovered by applying an external pressure of 1.1 MPa.[150] (ii) Due to the low tensile and creep strength of lithium, even pressures below 1 MPa result in plastic deformation of the lithium metal and hence result in the dense deposition.[148, 150, 153, 154] However, thin lithium needles have high yield strengths of several tens of MPa due to a size effect common to many metals.[159, 160] Consequently, a plastic deformation of very thin needles at stack pressures below 1 MPa seems to be unlikely. (iii) Zhang *et al.*[152] suggested that the local stress at the tip of growing dendrites and protrusions may be high enough to locally block the pores of the separator and hence the Li^+-ion transport. Therefore, the electrodeposition would preferentially occur elsewhere.[152] Additionally, they suggested that creep flattens the protrusions.[152]

2.4 Deformation Mechanisms of Lithium Metal

On several scales, mechanical effects play an important role in the formation of lithium structures. As described in the last section, stack pressure has been reported to be a decisive parameter for the suppression of dendrites on the cell level.[73, 148–153] On a smaller scale it was shown that lithium dendrites can be removed from the electrode by fluid shear forces from the electrolyte, generated by shaking the cell.[23] The mechanical properties of the SEI have been often associated with the onset of dendritic growth.[5, 9] Even at the lowest scales, growth models exist where the formation of dendrites is caused by mechanical stresses.[11, 71]

These observations indicate that the deformation of lithium may play an important role in the formation of the electrodeposits. Sargent and Ashby[161] have constructed a deformation mechanism map for potassium. Additional measurements for lithium and sodium indicate that this map is also applicable for these alkali metals.[161] A simplified version of this map is shown in Figure 2.4. At room temperature, the homologous temperature (temperature divided by the melting temperature T_m) of lithium is approximately 0.65 (highlighted by the red line in Figure 2.4). Due to that high homologous temperature, plastic deformation can occur by high-temperature creep mechanisms at stresses considerably lower than the yield stress known for conventional plasticity. Hereby "conventional plasticity" designates athermal deformation mediated by motion and interaction of dislocations, while "creep" is used to designate mechanisms that are at least partly comprised of thermally activated self-diffusion. The red line in Figure 2.4 shows that dislocation climb (power law creep) is active at room temperatures for stresses almost one order of magnitude below dislocation glide. At even lower stresses diffusion creep is active. Grain boundary diffusion (Coble creep) is already present at far lower temperatures and can be expected to be very facile at the homologous temperature of 0.65. Even deformation by bulk diffusion (Nabarro-Herring creep) is possible at such high homologous temperatures (i.e., room temperature). Gireaud *et al.*[73] have observed an improved cycling performance of lithium metal anodes even at a low stack pressure of 0.2 MPa, which is considerably lower than the yield strength of polycrystalline lithium (approximately 0.8 MPa[162]). The creep mechanisms mentioned here are already active at stresses below the stresses required for conventional plasticity. Creep may affect the morphology of the deposit, which could prevent or mitigate dendrites.

For all temperatures significantly below the melting point, the diffusion parameters for the different pathways are typically in the order $D_S > D_{GB} > D_B$, where D_S, D_{GB}, and D_B represent

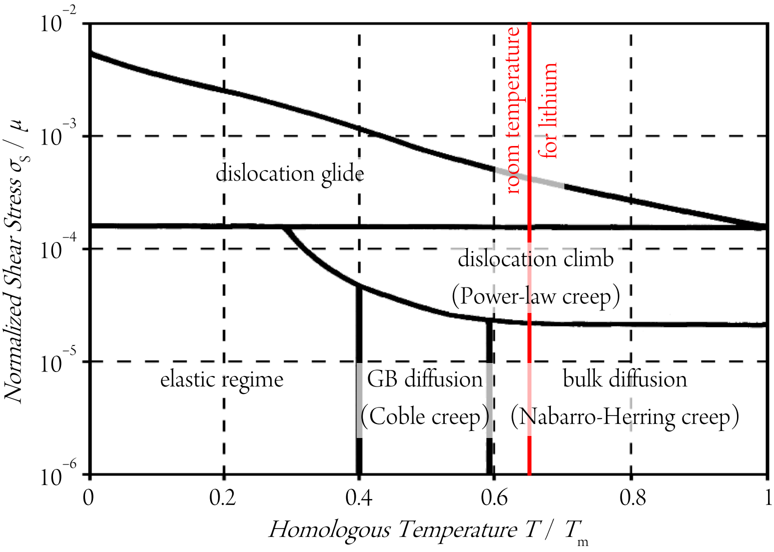

Figure 2.4: Deformation mechanism map for alkali metals. Simplified from Sargent and Ashby.[161]

the surface, grain boundary, and bulk diffusivities, respectively.[163] Therefore, surface diffusion may contribute to the deformation of smaller lithium structures in addition to the processes shown in the deformation map. However, it is well known that impurities can significantly influence surface diffusion.[164] Since the surface of lithium metal in batteries is usually covered with an SEI, the surface diffusivity (interface diffusivity) will also depend on the SEI and hence on the electrolyte used.

2.5 Motivation

As summarized in Section 2.3, many reports can be found that focus on the improvement of LMBs by applying various countermeasures against the growth of lithium dendrites. However, judging strategies to prevent dendrites is difficult as long as the fundamental growth mechanisms are still under debate (see Section 2.2). For example, if the growth at tips is negligible, attempts to shield the electric field there are ineffective. Many theories that describe the growth mechanism of lithium deposits are contradictory or are not compatible with existing experimental observations. In the following common models and theories for growth of lithium dendrites are critically assessed.

2.5.1 Critical Discussion of the Models for Lithium Electrodeposition in Literature

The models based on ionic concentration gradients and spherical diffusion lead to growth directly at the tip of the filaments. However, various experimental studies show that the growth of lithium deposits does not solely occur at tips or does not happen at tips at all.[11, 12, 49, 63, 71, 165] The transport limitations within the SEI may result in the onset of the growth of lithium structures, but these structures have to be extremely small and it is experimentally impossible to observe the evolution of electrodeposits that are only a few nanometers in size under realistic conditions. Therefore, to date it is unclear if these structures grow from their base or at the tip, which would be necessary if the growth is controlled by the transport limitations within the SEI as described by Akolkar's group[68, 69]. The correlation of their model and the experimentally observed electrodeposits is questionable since the model describes the growth in a less than 20 nm thick SEI but the observed structures are more than

100 µm in diameter. Although it cannot be excluded that the transport limitations within the SEI play an important role, it has been shown that they are not necessary to form lithium needles since these can be grown in absence of an SEI by physical vapor deposition.[72] Chen *et al.*[70] proposed that transport limitations in the SEI can result in the growth of needles, but they only deposited a small amount of lithium ($0.125\,\mathrm{mAh\,cm^{-2}}$) during their experiments. Park *et al.*[166] used the same electrolyte, but with $LiNO_3$ as additive. For different current densities, they always found a transition from spherical to fibrous electrodeposition.[166] For the low current densities of $-0.2\,\mathrm{mA\,cm^2}$ and $-0.5\,\mathrm{mA\,cm^{-2}}$, this transition occurred for area specific capacities larger than $0.1\,\mathrm{mAh\,cm^{-2}}$, while the transition occurred later for higher current densities.[166] These observations are not in agreement with growth mechanism of fibers/needles based on the transport limitations within the SEI. Higher current densities would result in an earlier depletion of the Li^+ ions and hence a transition to fibrous growth for lower area specific capacities.

Models based only on the non-uniformity of the SEI cannot explain one dimensional growth of needles with constant diameter as observed in experiments (e.g., by Steiger *et al.*[12]). As freshly deposited metal necessarily exhibits no or only a thin SEI, deposits would grow three-dimensionally when the growth mechanism is dominated by the non-uniformity of the SEI. Yamaki's whisker-like growth model has been criticized by Monroe and Newman[10] for broad assumptions about the flow behavior of lithium. Moreover, it relies on another mechanism for the kinked structures, which are often observed during the electrodeposition of lithium. These structures can be hardly explained by the model. Therefore, Yamaki *et al.*[11] suggested a defect-based growth (e.g., at kinks) when the Li^+-ion transport to the electrode surface is impeded by a dense cover of long whiskers. However, kinks have been observed at small structures on substrates without other structures around, which could hinder the transport of Li^+-ions to the substrate surface.[12, 71, 72] The defect-based lithium insertion can explain growth from the base and at kinks, which are the growth modes that are typically observed when the electrodeposition of lithium is observed at spatial resolutions high enough to determine the details of the growth. However, these observations[12] were exclusively made at low deposition rates.

Deposition rates can vary by several orders of magnitude and it seems plausible that different mechanisms are dominant at different deposition rates. So far, only little work addresses the importance of the different growth modes at different rates or focused on the transition between them. Bai *et al.*[63] and Yamaki *et al.*[11] described the transition between different basic growth mechanisms of lithium electrodeposits. Bai *et al.* observed a transition from mossy lithium growing from the base to a dendritic tip-growth after Sand's time and Yamaki *et al.* described a transition from whisker-like growth to defect-based insertion at the tip and kinks when the electrode is covered with long whiskers, hindering the ion transport to the surface of the electrode. Steiger *et al.*[49] described a transition from the growth of lithium filaments to lithium moss, but both occurred at low deposition rates and were attributed to a defect-based insertion and not a transition in the basic growth mechanism. A major aspect that has not been clarified by Steiger *et al.*[49] is how dendrite growth transitions from the described defect-based insertion at low rates to other mechanisms when stronger concentration gradients/transport limitations appear in the electrolyte at higher rates.

2.5.2 Critical Discussion of Observations of Lithium Electrodeposition in Literature

Experimental studies using *in situ*/*operando* microscopy to study the electrodeposition of lithium can be found in literature: High resolution images of growing lithium structures were obtained by *in situ* scanning electron microscopy (SEM)[167] and *in situ* transmission electron microscopy (TEM).[71, 168–170] Although these studies can contribute to a better understanding, the experiments are usually limited to very thin cells that constrict the growth of dendrites, which is likely to be very different to the growth in practical battery applications. In open cell configurations, the choice of electrolytes is limited to non-volatile ionic liquids, which change the environment compared to most practical applications. Furthermore, it is well known that the growth is influenced by the electron beam.[167, 168] With light microscopy, the growth of lithium can be observed *operando* without the presence of an electron beam. Many studies helped to better understand the growth of lithium deposits and the lithium dissolution.[11, 12, 23, 49, 63, 67, 165, 171, 172] However, the depth of field is limited to about 1 µm or less when optics are chosen that enable microscopy close to the resolution limitations of visible light. The design of the *operando* cell, its optical window, and the electrolyte complicate imaging at the resolution limit. Consequently, most groups report light microscopy at lower resolutions. With these conditions, the depth of field is high and lateral growth can be easily observed but it is not possible to identify small regions where the electrodeposits grow, which is essential for a fundamental understanding of the growth mechanisms. Steiger *et al.*[12, 49, 72] used *operando* light microscopy at the resolution limit of visible light but the observed area was relatively small and related to that the depth of field very limited. Therefore, only structures within the same focal plane were analyzed.

2.6 Objectives of this Work

Despite decades of research on lithium metal anodes for rechargeable batteries, there is no general agreement on the fundamental mechanisms governing the electrodeposition of lithium. The growth of so-called dendrites during the electrodeposition, i.e., the charge of a secondary LMB, hinders the commercialization of such batteries. The goal of this thesis is to study the electrodeposition of lithium experimentally at all rates relevant for practical batteries to gain a better understanding of the fundamental mechanisms controlling the morphology. Based on a better understanding of the mechanisms, this thesis aims to propose new strategies to prevent dendrite growth. In addition to lithium, the electrodeposition of sodium is studied as alternative element for secondary batteries. The comparison of lithium and sodium shall elucidate similarities and differences of both metals when used as anode material.

To overcome the experimental challenges for the *in situ/operando* studies of the electrodeposition (see Section 2.5.2), a dedicated light microscopy setup was purchased and assembled and a custom-build electrochemical cell with a window was developed. The requirements for the experimental setup are the following: (i) The optical resolution has to be close to the physical resolution limit of visible light (~500 nm). (ii) To overcome the limited depth of field, the acquisition of *z*-stacks and the calculation of images with an extended depth of field have to be possible. (iii) The field of view needs to be maximized to obtain statistically relevant data. Ideally, the full electrode surface is observed to exclude misinterpretations due to electrodeposition outside of the field of view. (iv) The acquisition of image stacks has to be fast to enable the observation at very high deposition rates. The details about the experimental setup can be found in Chapter 3.

The main part of this work is structured as follows: Chapter 4 compares the electrodeposition of lithium and sodium and their chemical stability. The work for this chapter was conducted with the light microscope previously used by Steiger *et al.*[12, 49, 72, 173]. The custom-build cell used in this chapter also differs from the cell used in the chapters 5 and 6 (see Section 3.2.2). The fundamental growth mechanism of lithium is analyzed in more detail in the chapters 5 and 6. In Chapter 5, the growth is observed at various rates from the lowest rate at which transport limitations of the electrolyte can be excluded to a 2000 times higher rate at which the cell overpotential indicates a full depletion of the Li^+-ions in the electrolyte at the surface of the lithium metal. For an area specific capacity of $3\,\mathrm{mAh\,cm^{-2}}$, which is a realistic value for a commercial battery, the applied rates correspond to times between less than two minutes and 60 hours to fully charge the battery. Therefore, these rates cover the range of rates that is relevant for practical applications. Chapter 6 focuses on a detailed evaluation of different structures of the electrodeposits. A growth mechanism is suggested that can explain the observations. It relates lithium insertion to crystalline defects such as grain boundaries and dislocations and interrelates growth with the mechanical stress. Chapter 7 summarizes and concludes this thesis.

The results shown in Chapter 4 are partly published as part of collaborative work (see[174, 175]) and the chapters 5 (see[176]) and 6 (see[177]) are also published in peer reviewed journals.

3 Methods

Operando light microscopy was used to observe the growth of lithium and sodium electrodeposits. For additional investigations, selected cells were disassembled in a glove box and after washing in DMC, the substrates with the lithium electrodeposits were transferred into an SEM (Zeiss Merlin). To protect the air sensitive samples, a vacuum transfer system (Leica EM VCT 100) was used for the transfer from the glove box to the SEM.

3.1 Materials

3.1.1 Electrodes

All experimental cells had metallic electrodes of either lithium (99.9 %, Alfa Aesar) or sodium (99.95 %, Alfa Aesar). The sodium metal was pressed into a PE mold to form a bar with a height and width of approximately 1 mm and the electrodes were cut from this bar with a scalpel. To form lithium electrodes, small pieces were directly cut from the lithium ribbon (as delivered). By cutting the electrodes into the desired shapes, it was ensured that the electrodes had freshly cut surfaces without reaction layers. The experiments in Chapter 4 were executed with three electrode setups with all three electrodes either being out of lithium or out of sodium. However, cutting the electrodes with dimensions in the order of 1 mm within the glove box results in significant variation of the shape across the experiments. To observe the electrodeposition onto electrodes with a reproduceable shape, copper blocks (99.9999 % Puratronic, Alfa Aesar) were used as working electrodes in Chapter 5 and 6. These blocks were cut from a 0.5 mm thick foil and subsequently ground and polished (last polish step with a grit size of 4000) to the desired shape as shown in Figure 3.3. The front side facing towards the lithium metal counter electrode was ground at an angle of approximately 10 ° to improve the observation from the top of nucleation and initial growth. The active area was about 0.3 to 0.4 mm^2 in size. Since the Cu electrodes were ground manually, the blocks varied to a certain extent in size and shape but significantly less than for the lithium and sodium electrodes. Their surface can exhibit a slight curvature, which in combination with the illumination in the microscope led to variations in brightness in the images/videos. To remove trace oxides from the copper surface, the blocks were heated to approximately 250 °C in a glove box antechamber in a forming gas atmosphere (5 % hydrogen (H_2) and 95 % argon (Ar)) at 2 mbar.

3.1.2 Electrolytes

For lithium cells used in Chapter 4, 5, and 6, a commercially available electrolyte (1 M $LiPF_6$ in a 1:1 volume ratio mixture of EC and DMC) from Merck, known as LP30, was used. For sodium cells in Chapter 4, the electrolytes 1 M $NaPF_6$ (sodium hexafluorophosphate, 99+ %, Alfa Aesar) in a 1:1 volume ratio mixture of EC (anhydrous, 99 %, Sigma Aldrich) and DMC (anhydrous, 99 %, Sigma Aldrich) and 1 M $NaClO_4$ (sodium perchlorate, anhydrous, 98.0-102.0 %, Alfa Aesar) in PC (propylene carbonate, anhydrous, 99.7 %, Sigma Aldrich) were used. Before mixing with the solvents, the salts were dried under vacuum. $NaPF_6$ was dried at approximately 110 °C for 64 h and $NaClO_4$ at approximately 80 °C for 18 h.

3.2 *Operando* Light Microscopy

Light microscopes and custom-built electrochemical cells were used for the *operando* light microscopy.

3.2.1 Devices

For Chapter 4, an Olympus BXFM microscope was used in the bright field mode to perform *operando* light microscopy. For the subsequent chapters the Olympus microscope was replaced by an optimized Nikon Eclipse LV-UDM microscope. To increase the depth of field (DOF), image stacks were acquired with both microscopes. An objective scanning system with a piezo drive (PIFOC PD72Z2CAA, Physik Instrumente (PI) GmbH & Co. KG) was used for the fast acquisition of large image stacks (typically more than 100 images) on the Nikon microscope. This nanofocus system can be mounted into one position of the nosepiece of the microscope and objectives mounted into the system can be used for the fast acquisition of *z*-stacks. A stack consisting of 100 images could be recorded within as short as approximately 10 s, enabling the *operando* observation at high deposition rates. With this optimized setup, it is possible to observe sample volumes of up to 0.27 mm^3 at a spatial resolution close to the physical resolution limit of light (~500 nm).

The Olympus BXFM was already used previously for light microscopy investigations of the growth of lithium dendrites in our group[12, 49, 72] and for the experiments on sodium presented in Chapter 4, which were partly published as part of cooperative research with other groups[174, 175]. For most of the experiments in Chapter 4, the images are acquired at a reduced spatial resolution. The field of view of this microscope at the highest resolution was too small to observe all relevant areas of the electrodes and therefore the resolution was reduced to capture a larger area. To solve this dilemma of spatial resolution vs. recorded volume, the above-mentioned new microscope was configured and acquired within this thesis. In addition to the fast acquisition of *z*-stacks and the maximization of the field of view, a high dynamic range (range between pure black and pure white) was considered when the microscope components were selected. This is advantageous since the reflective metallic deposits often result in images with high contrast. A larger field of view combined with high resolution was achieved by selecting an objective with lower magnification but similar numeric aperture (*NA*) together with a larger camera sensor with a sufficiently high pixel count to fulfill the Nyquist-Shannon sampling theorem. This fundamental theorem of sampling statistics shows that the sampling rate needs to be at least twice as high as the highest frequency of the signal.[178, 179] For digital imaging, this results in a pixel size that needs to be at least two times smaller than the projection of smallest optically resolved objects on the sensor. The lateral resolution of an objective is based on the minimum distance of two objects that can be distinguished as individuals; this distance can be calculated with the Rayleigh criterion

$$r = \frac{1.22 \cdot \lambda}{2 \cdot \sin\theta \cdot n} = \frac{0.61 \cdot \lambda}{NA},^{[179]} \tag{3.1}$$

where λ is the wavelength, θ is the half-angle of the cone of light that can enter the objective, and n is the refractive index of the imaging medium. The maximum pixel size in *x*- and *y*-direction is calculated with

$$d_{\max} = \frac{M \cdot r}{2} = \frac{M \cdot 0.61 \cdot \lambda}{2 \cdot NA}, \tag{3.2}$$

with the magnification of the objective M.

The combination of the lower magnification of the objective and the larger camera sensor result in an observed area that is more than 40 times larger than with the old microscope while the resolution stays almost the same. This configuration allows to observe the full electrode area of the custom-built electrochemical cell (Section 3.2.2) during the electrodeposition, which is important for the statistical relevance of the data. A calibration scale with 1 µm lines was used to compare the observed area and the resolution of the Olympus BXFM and the Nikon Eclipse LV-UDM (Figure 3.1). Both microscopes were used with their dedicated objectives to observe the electrodeposition at a resolution close to the physical limit. The images acquired with the Nikon microscope and the Olympus microscope are shown in Figure 3.1a and b, respectively. Figure 3.1c and d are magnified areas of the images obtained on both microscopes to compare their resolution. Hardly any differences are noticeable.

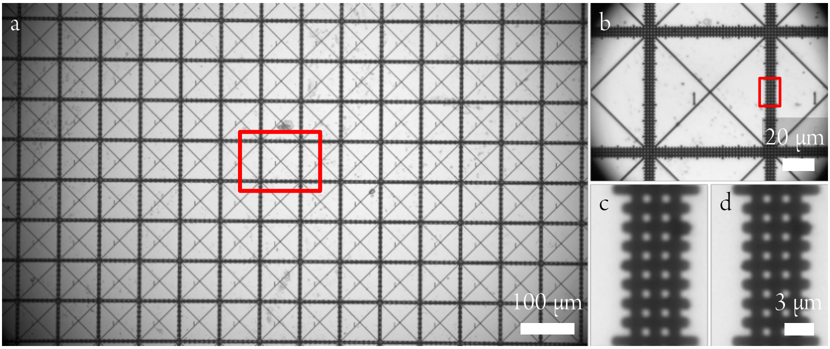

Figure 3.1: Images of a calibration scale with 1 µm lines acquired with the new optimized light microscope from Nikon (a) and the Olympus microscope (b). The red rectangle in (a) marks the field of view of the Olympus microscope shown in (b). A magnification of the marked area in (b) is show for the new (c) and old setup (d) to compare the resolution of both microscopes.

3.2.2 Electrochemical Cell

The electrochemical cells were assembled inside an argon-filled glove box (water (H_2O) and oxygen (O_2) content typically <0.1 ppm). The cells used in Chapter 4 consisted of a borosilicate glass substrate, an O-ring, and a borosilicate glass window, which were clamped between two metal plates to seal the cell. A sputter coater (Leica EM SCD 500) was used to coat three tungsten current collectors onto the glass substrate for the working, counter, and reference electrode. The electrodes were placed onto the current collectors such that the cut edges of the working and counter electrodes were facing each other. The electrodes were slightly pressed onto the current collectors by the cell window when the cell was closed. A schematic of the cell is illustrated in Figure 3.2 in top view. The cell was filled with approximately 200 µl of electrolyte. The short width of the electrodes allowed to observe most of the active working electrode surface at a 10x magnification with the Olympus BXFM.

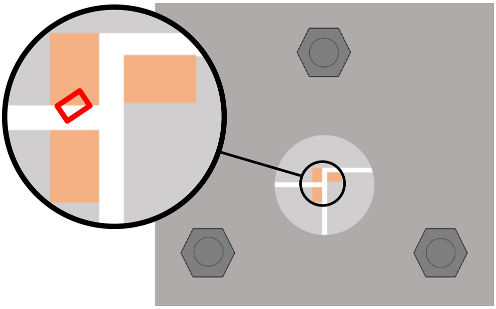

Figure 3.2: Schematic of the light microscopy cell used in Chapter 4. The perforated upper metal plate and three screws to clamp the cell are shown. The current collectors (light grey) and the three electrodes (orange) can be seen through the perforation. The magnified area shows the electrodes in more detail. The upper electrode is the working electrode, the lower one the counter electrode and the reference is on the right. The red box on the working electrode indicates the field of view in the light microscope. The cell was typically rotated to maximize the length of the observed edge. Modified from Mandl *et al.*[175]

For the experiments in Chapter 5 and 6 the cell was optimized: To enable higher current densities for the experiments in Chapter 5, the sputtered current collectors were replaced

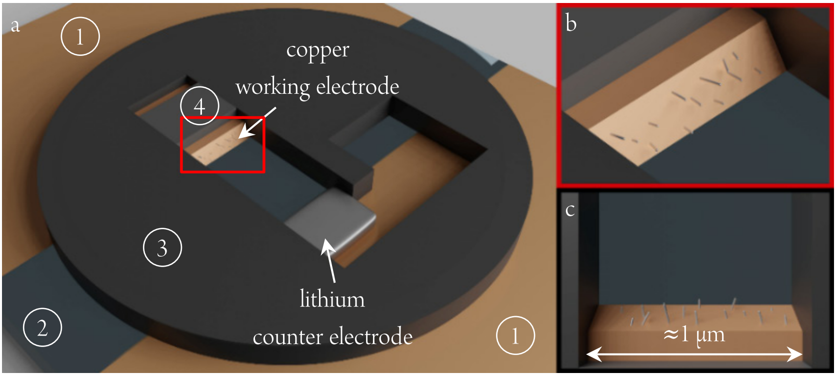

Figure 3.3: (a) Schematic of microscopy cell in 3D view. The copper current collectors (1) are placed on the sapphire substrate (2). The shape cut into the flat rubber sealing (3) defines the shape of the cell and another small piece of the rubber sealing (4) is placed on the working electrode. (b) Magnification of the working electrode with needle-like lithium deposits and (c) the working electrode in top view as observed with the light microscope during *operando* measurements. Reprinted from Becherer *et al.*[176]

with copper foils (10 µm, >99.95 % from h+s Präzisionsfolien GmbH), which were attached to a sapphire substrate. Additionally, the O-ring was replaced by a flat rubber sealing with the shape of the electrodes and the electrolyte compartment cut from it. Depending on the exact shape of the hand-cut rubber sealing, this minimized the electrolyte volume by a factor between 50 and 100. Therefore, side reactions of lithium with electrolyte impurities such as H_2O were significantly reduced. The copper block (see Section 3.1.1) that was used as working electrode was clamped into the slit of the rubber to prevent deposition at the sides of the copper block. Another small piece of the rubber was placed on top of the copper to prevent plating there and to press the block down onto the current collector. The rubber could not be placed directly at the edge of the copper block since it would squeezed into the view onto the deposition area when the cell is sealed and the rubber compressed. In addition to the tilted surface facing the counter electrode, deposition is only possible at a small stripe on the top side of the block. By limiting the areas where electrodeposition can occur, the current densities can be defined more precisely. After filling the cell with electrolyte, the cells were sealed by clamping the sapphire substrate and a sapphire window between the two metal plates as illustrated for the non-optimized cell in Figure 3.2. A schematic of the optimized cell is shown in Figure 3.3. The lithium counter electrode was pressed onto the other current collector either directly with the finger or with a tweezer during assembly to ensure electronic contact. To prevent contamination of the counter electrode, a clean PE foil was placed on the lithium when it was pressed onto the current collector. The thickness of the counter electrode was less than the thickness of the rubber and the electrode was consequently not compressed by the cell window as in the other cell. The distance between the two electrodes varied to a certain extend due to the manual assembly process. The lowest inter-electrode distance in the standard cells used for the experiments of the chapters 5 and 6 was approximately 0.7 mm and the largest distance in the standard cells was about 1.6 mm.

3.2.3 Image Processing

The information obtained from single exposures close to the physical resolution limit of a light microscope is very limited when three-dimensional structures are observed. While the resolution is proportional to NA (see Equation (3.1)), the DOF is inversely proportional to the square of NA ($\mathrm{DOF} = \frac{n \cdot \lambda}{NA^2}$).[180] Figure 3.4a shows a single exposure in the middle of a z-stack during the electrodeposition of lithium in the microscopy cell. Only a few lithium needles along one line are distinguishable since the DOF is only about 1.1 μm. The image with an extended DOF (EDOF) of the z-stack (Figure 3.4b) shows the complete electrode in focus and a large number of needles. One needle that grew in the focus plane of Figure 3.4a is highlighted in both images. The image in Figure 3.4b was calculated from a stack of 146 images with a distance of 2.2 μm in z-direction between the images. This step size results in an undersampling. However, the quality of the images is hardly distinguishable from images calculated of stacks with smaller steps. Therefore, 2.2 μm steps were typically used to acquire z-stacks since it allows faster acquisition of the stacks, and due to the large memory space required for the stacks, it also allows a more frequent acquisition of stacks or longer experiments. The comparison of the two images clearly demonstrates the benefit of the focus stacking to calculate EDOF images.

The EDOF images were calculated with an algorithm based on Laplacian pyramids.[181] The algorithm was implemented in Python and already used for the experiments with the Olympus BXFM microscope (Chapter 4) to compute smaller z-stacks typically consisting of

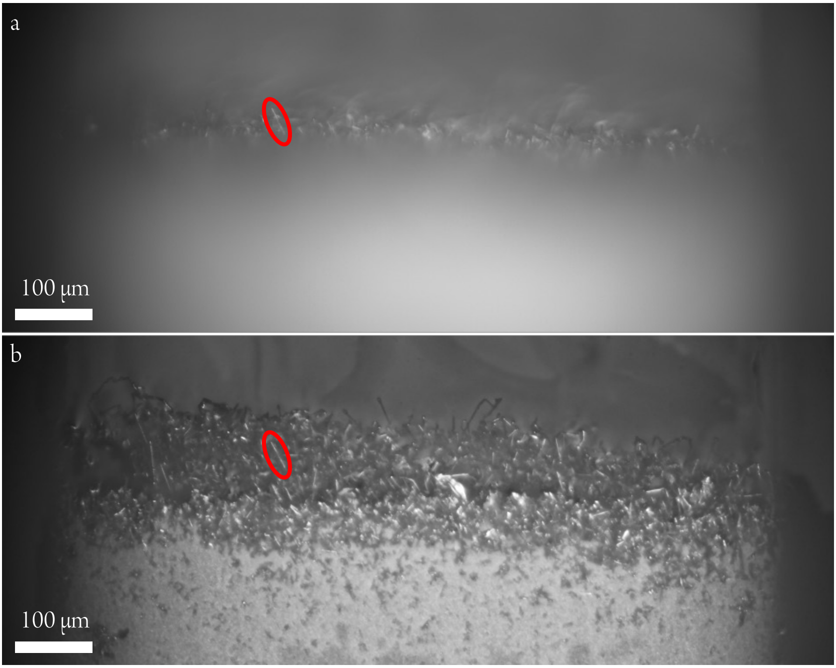

Figure 3.4: (a) Single exposure in the middle of a *z*-stack with only a small region of the electrode in focus. (b) The EDOF image that was calculated from this *z*-stack with the complete electrode in focus. A needle that is in focus in both images is highlighted in both images.

about 30 images. For the experiments on the Nikon Eclipse LV-UDM microscope (chapters 5 and 6), the implementation of the algorithm was optimized to enable the fast computation of larger stacks and large number of stacks on a GPU (graphics processing unit) by using the open-source just-in-time compiler Numba. The calculation of EDOF images is typically also possible with the commercial imaging software of the common microscope manufactures. However, before acquiring the new microscope from Nikon, microscopes of various manufactures were tested, which included the test of the focus stacking algorithms implemented in their software and none of the algorithms reached the performance (speed) and quality (level of detail) of the algorithm based on Laplacian pyramids used here. In case of the algorithm implemented in the Nikon software NIS-Elements, the computation time is significantly slower since it does not use the high-end GPU (NVIDIA GeForce RTX 2080 Ti) that is used for the computation with the self-implemented algorithm. Additionally, there are some differences in the image quality: The algorithm used by the NIS-Elements software is more prone to shadow and highlight clipping and to color artifacts when color images are used and the input images exhibit slight color flare in the out of focus areas. The latter is minuscule for this work since usually grayscale images are used due to the higher dynamic range of the monochrome camera and because the observed area is approximately two times larger than with the color camera. The results from the algorithm implemented in Nikon's NIS-Elements and the self-implemented algorithm are compared in Figure 3.5. To simulate the high contrast during the electrodeposition experiments, an aluminum plate with deep scratches was used for the comparison. A *z*-stack with 274 images and 0.55 µm steps between the focal planes of the images (Nyquist-Shannon sampling) was acquired with the microscope in approximately 38 s. Figure 3.5a shows the EDOF image that was calculated with NIS-Elements in approximately 139 s. The calculation on the GPU with the algorithm based on Laplacian pyramids took only 33 s and the resulting image is shown in Figure 3.5b. Since most of these 33 s is required for the GPU to read the images from the hard drive, the total time can be further decreased when the GPU starts to read the images in parallel to the stack acquisition. With this optimization, the EDOF image can be calculated within about 52 s after the acquisition of the stack starts. Since the image calculated with the algorithm based on Laplacian pyramids did not use the full grayscale (except for a few pixels) the levels were adjusted to increase the contrast; additionally, a gamma correction (nonlinear operation to modify brightness and contrast of an image) of 1.15 was applied. The image calculated in NIS-Elements was not adjusted since it exhibited already slight shadow and more noticeable highlight clipping. This is clearly apparent in the magnification in Figure 3.5c while the full information is preserved Figure 3.5d, which is the magnification of the EDOF image calculated with the Python script. Figure 3.5e and f compare the algorithms for color images. Another aluminum sample was used to acquire *z*-stacks with a color camera. This sample produced color flare in the out of focus areas. Color artifacts can be found in both EDOF images. However, the blue and yellow spots are very dominant in Figure 3.5e (two examples are highlighted by arrows), which was calculated with NIS-Elements, while only slight yellow and green tints are visible in some regions of Figure 3.5f.

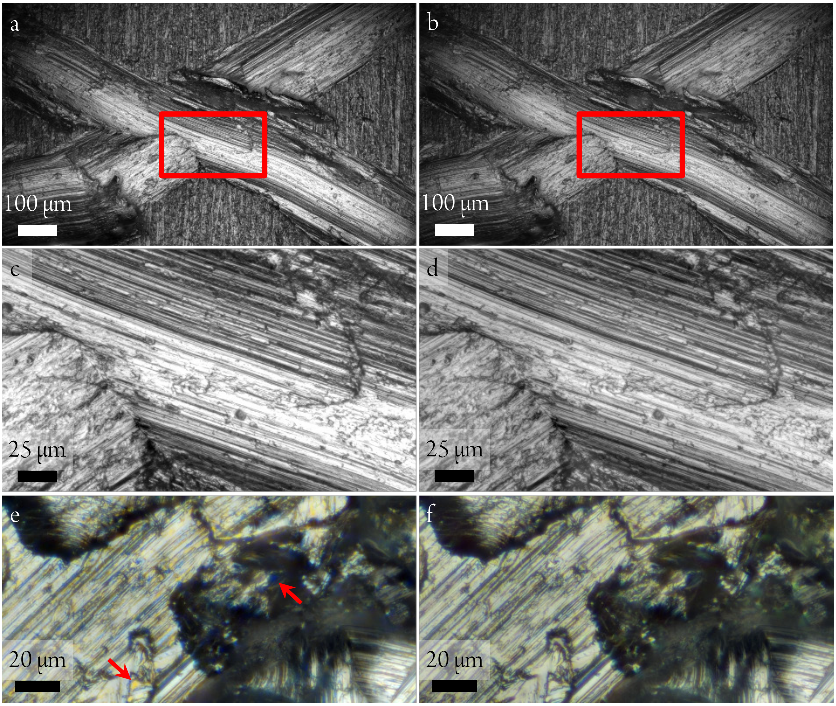

Figure 3.5: EDOF images of an aluminum sample (*z*-stack with 274 images with a 0.55 µm step size) calculated with Nikon's NIS-Elements software (a) and the Python script using an algorithm based on Laplacian pyramids (b). (c) and (d) are magnifications of (a) and (b), respectively. Color EDOF images of another aluminum sample calculated with NIS-Elements (e) and the Python script (f). Two red arrows highlight an example for a yellow and a blue spot in the color image calculated with NIS-Elements.

In addition to the possibility to calculate EDOF images, acquiring *z*-stacks has the benefit that the stacks contain three-dimensional information in addition to the two-dimensional projections acquired by conventional light microscopy. The growth rates of needle-like lithium electrodeposits and of segments in kinked structures are evaluated in Chapter 6. To measure their length and growth velocity, the image stacks of the raw images were evaluated to determine the *z*-coordinates of the measured features in addition to their *x*- and *y*-coordinates. This was done by finding the raw image in which these features are in focus. The error in *z*-direction dominates the total error since the distance *z*-direction between two images of a stack is 2.2 µm and the lateral resolution is about 0.5 µm. Therefore, an uncertainty of the length measurements of needles and segments below 3 µm can be assumed.

3.3 Electrochemical Methods

A potentiostat (CompactStat.e, Ivium Technologies B.V.) was used for the galvanostatic electrodeposition of lithium and sodium.

3.3.1 Electrochemical Pretreatment of the Electrodes

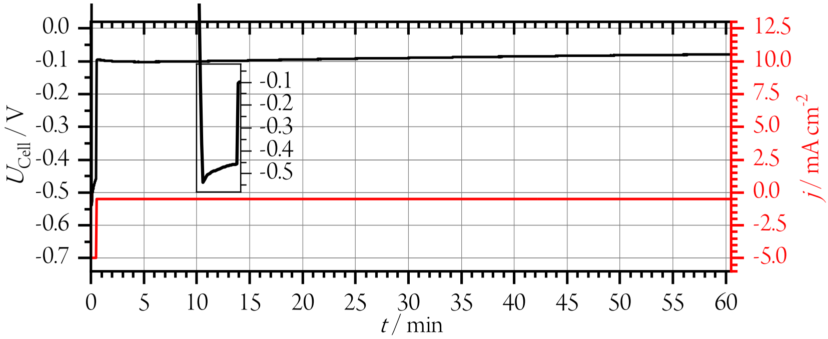

Figure 3.6: Galvanostatic voltage vs. time trace of the pretreatment. The inset shows the voltage trace of the seeding step for the nucleation more detailed.

For the electrodeposition onto the copper blocks in Chapter 5 and 6, an electrochemical pretreatment was performed on each cell before the deposition at different rates was started. With this pretreatment, a dense lithium film was created on the surface of the copper electrodes. The pretreatment consisted of a seeding step of 30 s for the nucleation at -5 mA cm^{-2} and was followed by the deposition of 0.5 mAh cm^{-2} at a rate of -0.5 mA cm^{-2}. Figure 3.6

shows an exemplary voltage trace for the pretreatment. The inset displays the initial 30 s seeding step at $-5\,\mathrm{mA\,cm^{-2}}$ in more detail.

3.3.2 Electrodeposition of Metals

The metals were typically plated by galvanostatic electrodeposition. In Chapter 4 the metals were electrochemically deposited and dissolved, while in Chapter 5 and 6 the electrodeposition of lithium was studied in more detail and electrodissolution was not studied. For the comparison of the electrodeposition at different rates in Chapter 5, $5\,\mathrm{mAh\,cm^{-2}}$ of lithium was typically deposited directly after the pretreatment. The rates were adjusted to constant values between $-0.05\,\mathrm{mA\,cm^{-2}}$ and $-10\,\mathrm{mA\,cm^{-2}}$ in each cell.

For even higher rates, the lithium deposits grow quickly out of the field of view and might short circuit the cell after a short period of time. Therefore, the test cell was modified by increasing the inter-electrode distance to approximately 4 mm and the *operando* observation of the growth was observed with an objective with a lower magnification to apply deposition rates of $-50\,\mathrm{mA\,cm^{-2}}$ and $-100\,\mathrm{mA\,cm^{-2}}$. At $-100\,\mathrm{mA\,cm^{-2}}$ the cell overpotential reached the voltage range of the potentiostat and the deposition changed from galvanostatic to potentiostatic. This deposition was continued until a short circuit occurred.

4 Comparing the Electrochemical Cycling of Lithium and Sodium

In this chapter, the chemical and electrochemical stability of lithium and sodium electrodes are compared. In the first section, the cycling behavior in symmetrical cells with the analogous electrolytes 1 M $LiPF_6$ in EC/DMC (1:1) and 1 M $NaPF_6$ in EC/DMC (1:1) is studied. In the second section, the reactivity of sodium with different carbonate electrolytes is compared. In the last section, 1 M $NaClO_4$ in PC is used as electrolyte to observe the electrodeposition and dissolution of sodium in more detail.

4.1 Cycling Stability of Lithium and Sodium

The electrochemical cycling of lithium and sodium in the analogous electrolytes 1 M $LiPF_6$ in EC/DMC (1:1) and 1 M $NaPF_6$ in EC/DMC (1:1) is compared in this section. These results are published in Electrochimica Acta[175] as part of cooperative research that was initiated by Magdalena Mandl from the Helmholtz Institute Ulm (HIU) and Michael Danzer from the University of Bayreuth.

Figure 4.1 shows snapshots of a sodium electrode during the electrodeposition at $-1\ \mathrm{mA\,cm^{-2}}$. The field of view onto the working electrode is indicated schematically in Figure 3.2. To maximize the view onto the electrodeposits, the cell was rotated that the image diagonal was approximately parallel to the edge of the electrode. The video S6 of the deposition can be found in the supplementary materials[2]. Before this deposition step, the cell has been cycled for two cycles at a current density of $\pm 0.5\ \mathrm{mA\,cm^{-2}}$ (3 h per half-cycle) and an additional dissolution step was performed for three hours at $1\ \mathrm{mA\,cm^{-2}}$. After one hour and 12 minutes, bush-like deposits appeared in Figure 4.1b. Furthermore, detached particles

---

[2] Videos of the sodium deposition (S6) and cycling of lithium (S8) are available online in the supplementary materials of 10.1016/j.electacta.2020.136698.[175]

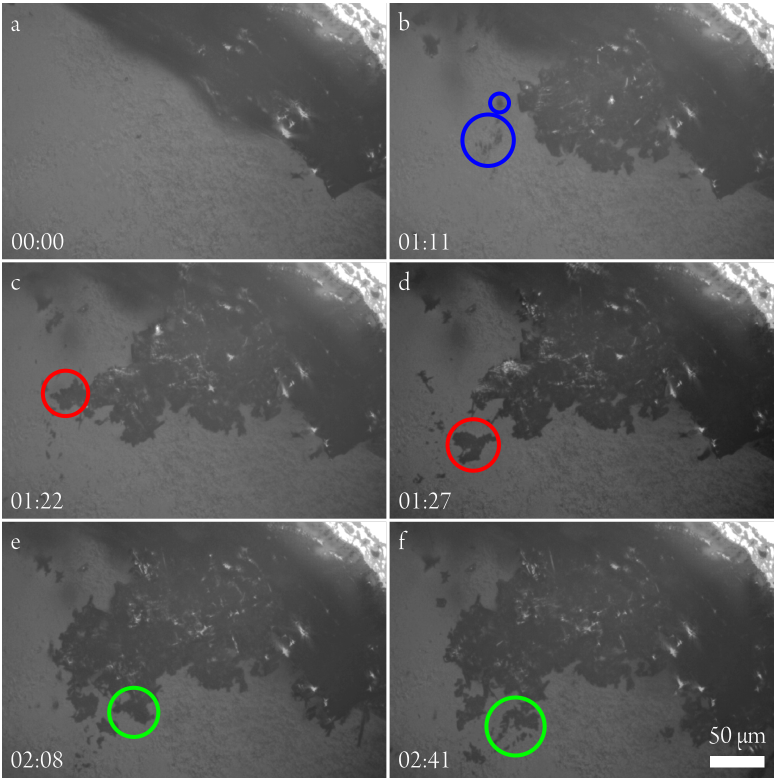

Figure 4.1: An image sequence of a sodium metal electrode during electrodeposition for three hours at a current density of $-1\ \mathrm{mA\,cm^{-2}}$, the deposition time of this half-cycle is given in hh:mm in the lower left of each image. Before the sequence shown, the electrode was cycled at $\pm 0.5\ \mathrm{mA\,cm^{-2}}$ for two cycles and an additional dissolution step at $1\ \mathrm{mA\,cm^{-2}}$ was performed. Each half-cycle lasted for three hours. Modified from Mandl *et al.*[175]

from the fresh deposits (blue circles) were observed. These particles detached from the deposits at the upper edge of the image. Figure 4.1c and d show a large particle (red circles) detaching from the tip of the bush-like deposits. A similar behavior can be seen in Figure 4.1e and f, but the detached particle collapses further into smaller particles (green circles).

After the deposition in Figure 4.1, the cell was cycled for three more half-cycles at ±1 mA cm^{-2}. The subsequent deposition and dissolution at ±1 mA cm^{-2} of the same electrode are shown in Figure 4.2. In Figure 4.2a, the surface of the electrode is fully covered with bush-like sodium deposits and inactive sodium particles. During the electrodeposition, these deposits grow further (end of deposition is shown in Figure 4.2b). In Figure 4.2c the electrode is shown after the last dissolution step. The deposits do not shrink, which suggests that they are already inactive, i.e., their deposition was irreversible.

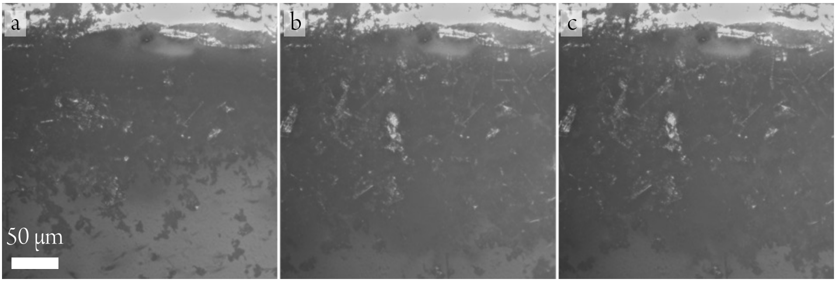

Figure 4.2: *Operando* light microscopy images of the sodium electrode in Figure 4.1 after it was cycled for two cycles at ±0.5 mA cm^{-2} and for two cycles at ±1 mA cm^{-2}. a) Electrode after an additional dissolution step at 1 mA cm^{-2}, b) at the end of the following electrodeposition at −1 mA cm^{-2}, and c) after the final dissolution at 1 mA cm^{-2}. Each half-cycle lasted for three hours. Modified from Mandl *et al.*[175]

To compare these processes with those of lithium plating and stripping, the same experiment was carried out with lithium. Therefore, a cell was assembled with lithium electrodes and LP30 as electrolyte. The cycling behavior of the lithium electrodes was relatively stable and more reversible. Cycling of the lithium cells at ±1 mA cm^{-2} did not result in bush-like electrodeposits. Therefore, higher current densities of ±3 mA cm^{-2} were applied for these experiments.

The second cycle and the subsequent half-cycle (dissolution) of a lithium metal electrode are shown in Figure 4.3 and the second and third cycle are shown in video S8[2]. During each cycle, lithium was dissolved for three hours at 3 mA cm^{-2} and deposited for three hours at

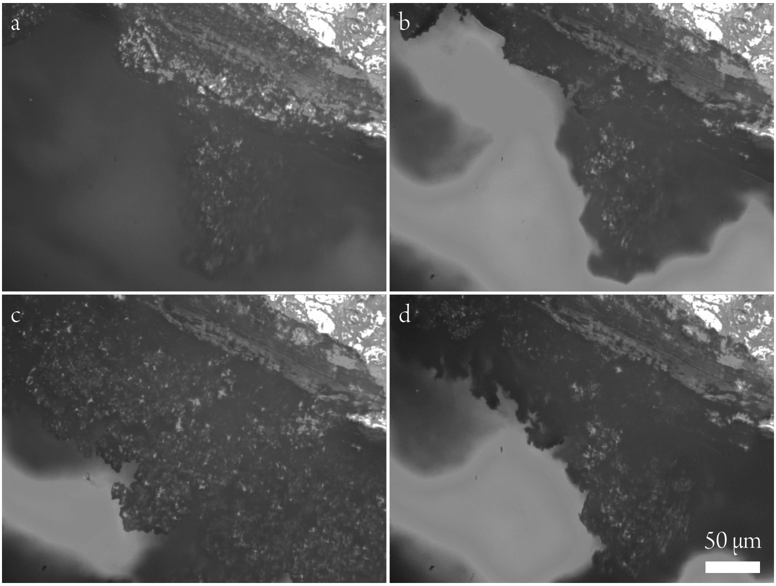

Figure 4.3: Lithium metal electrode that was previously cycled for one cycle at ±3 mA cm^{-2}. a) Electrode at the beginning of the dissolution step (second cycle) at a current rate of 3 mA cm^{-2}. b) Electrode after the lithium dissolution. c) Electrode after the electrodeposition at −3 mA cm^{-2} (end of second cycle). d) Electrode after the lithium dissolution at 3 mA cm^{-2} (third cycle). Each half-cycle lasted for three hours. Modified from Mandl *et al.*[175]

−3 mA cm^{-2}. Between dissolution and deposition as well as after the deposition, the cell was kept at the open circuit voltage (OCV) for 15 min; in this period, a relaxation of the overpotential to 0 V was always observed as it is expected in symmetrical cells. At the beginning of the first dissolution in Figure 4.3a most of the deposits are out of focus. After the dissolution, the deposits that occurred out of focus are mostly dissolved (Figure 4.3b) as visible by the brightness change mainly in the lower left region of the images. This indicates that the plating process is at least partly reversible. After the deposition in the second cycle (Figure 4.3c), the electrode is almost fully covered with mossy deposits that are in focus. After three hours of lithium electrodissolution (Figure 4.3d), the electrode looks quite similar to the end of the previous stripping step (Figure 4.3b). Although visible similarity can be found after one full cycle, the mossy features do not grow and shrink exactly at the same location.

In cells with excessive metal, the observed behavior of lithium, where deposition and dissolution occur in different regions, is not necessarily problematic. As long as the deposited metal is mechanically and electronically connected with the electrode, it is electrochemically accessible during further cycles. Even in cells with perfect Coulombic efficiencies, deposition and dissolution cannot be expected to be symmetrical in time, i.e., the deposits formed in the end of the electrodeposition are dissolved first during the electrodissolution. However, the observation of the detachment of metal, in particular during deposition as observed for sodium in Figure 4.1 and video S6[2], can be directly attributed to deterioration since the detached metal reduces the available capacity of the electrode.

4.2 Reactivity of Sodium with Carbonate Electrolytes

A further cooperative work initiated by Kristina Pfeifer from the group of Sonia Dsoke (IAM-ESS) resulted in a publication in ChemSusChem.[174] This publication focused partly on the chemical reactivity of sodium with different carbonate electrolytes. In this study, three carbonate-based electrolytes were used: (i) 1 M $NaClO_4$ in EC/DMC, (ii) 1 M $NaPF_6$ in EC/DMC, and (iii) 1 M $NaClO_4$ in PC. These electrolytes were prepared by the leading group in this study. All salts were dried under vacuum at 80 °C for 48 h and the EC/DMC-mixtures were mixed in a 1:1 weight ratio. The components used are equivalent to those used for the electrolytes in the other sections and stated in the materials section. All electrolytes were examined by Karl-Fischer titration and were found to contain less than 25 ppm H_2O. The author of this thesis conducted the observations with the light microscope. To give some context to this experiment, a preliminary experiment conducted by the group of Sonia Dsoke is presented in the following paragraph.

A 0.25 g piece of sodium metal with cleaned surfaces was immersed into 5 ml of each electrolyte and stored in the electrolyte for three days.[174] The changes of the electrolyte and the metal were observed visually.[174] For all three electrolytes, the appearance of the electrolyte changed within the three days.[174] In the two EC/DMC-electrolytes, the shiny metallic surface turned mat and the electrolytes became turbid.[174] While there was hardly any color change in 1 M $NaPF_6$ in EC/DMC, the electrolyte additionally turned brown and the metal surface became black in the 1 M $NaClO_4$ in EC/DMC-electrolyte.[174] Compared to the

EC/DMC-electrolytes, the changes in the 1 M $NaClO_4$ in PC solution were more subtle.[174] The metal remained shiny and the electrolyte clear.[174] There was only a slight change in color: the solution had a slightly yellow appearance and the metal became darker.[174]

To investigate the changes in more detail, a piece of sodium in the 1 M $NaClO_4$ in EC/DMC-electrolyte was observed for ten days with the light microscope. Since only the chemical reactions were observed, the cell shown in Section 3.2.2 in Figure 3.2 was simplified: The substrate with the sputtered current collectors was replaced by a PE foil and a piece of sodium was pressed directly onto that foil. Figure 4.4 shows the surface changes of the sodium metal over a period of ten days. It is evident that the metal surface continuously becomes darker over time. It is suggested that these surface changes are based on a solid interphase that is formed by the degradation products of the reactions between electrolyte and sodium metal. This interphase seems to be instable since small particles constantly peel off and float into the electrolyte, which causes an increasing turbidity. The change in turbidity can be clearly observed by the decreasing image intensity in the lower right of the images. Since this part of the images shows the PE foil, which does not react with the electrolyte, and the illumination and exposure time of each image are constant, the decreasing image

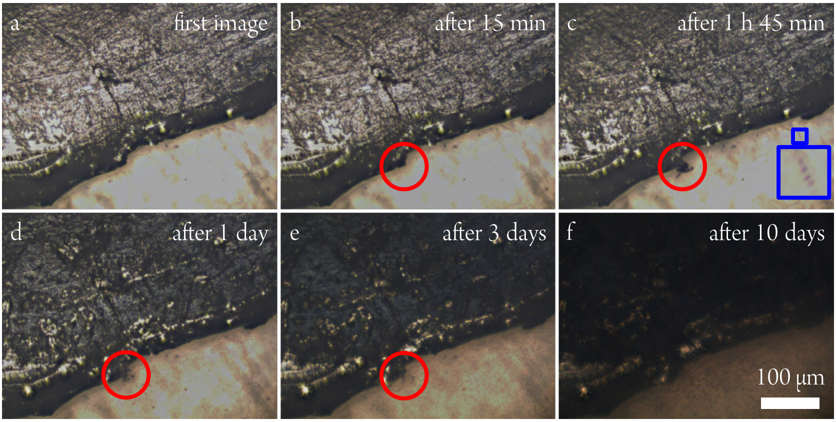

Figure 4.4: Light microscopy images of a piece of sodium on a PE foil (visible in the lower right of each image) in a sealed cell filled with 1 M $NaClO_4$ in EC/DMC. The image series shows the surface changes of the sodium metal time-resolved over a period of ten days. Modified from Pfeiffer *et al.*[174]

intensity can be associated with an incident light beam that is increasingly diffused by the electrolyte. Particles detaching from the bulk sodium into the electrolyte are also directly observed in the images: The red circles highlight a feature that seems to grow between Figure 4.4b and c and breaks off afterwards. It seems unlikely that such large particles grow due to the decomposition products of electrolyte and sodium. Therefore, it is more likely that a sodium particle was only loosely connected to the bulk sodium and moved slightly (e.g., due to stabilizing structures peeling off) and became only visible after this movement. In Figure 4.4c a particle can be directly observed when it floated from the sodium into the electrolyte. The larger blue box is a magnification of the smaller blue box and shows a line of multiple dark spots. This is an artifact from focus stacking. In the raw images, a single particle moves away from the bulk sodium in the timespan that was required to acquire the *z*-stack. The focus plane of each raw image is in a different distance to the particle, resulting in a varying sharpness of the spots in the blue box (Figure 4.4c).

These findings clearly show a high reactivity of sodium with the carbonate electrolyte even when no electrochemical potential is externally applied. 1 M $NaClO_4$ in PC is considerably more stable than the two EC/DMC-electrolytes, but even with this electrolyte changes were observed when sodium was stored in the solution for three days.[174]

4.3 Growth of Individual Sodium Needles

Since 1 M $NaClO_4$ in PC showed the highest stability in contact with sodium, this electrolyte was chosen to observe the growth of individual sodium needles at higher resolution. Figure 4.5 shows a high-resolution image sequence of sodium metal deposition at a low rate of $-20\ \mu A\ cm^{-2}$ in 1 M $NaClO_4$ in PC. The growth of a single needle is clearly observed. At the beginning of the deposition, most of sodium was plated outside of the field of view as the first two images are almost identical. In the following frames, a single needle grows. The growth occurs clearly at the base of the needle as the shape of the tip (red circles) does not change between the frame taken after 1 h 38 min and the last frame take after 4 h 1 min. Furthermore, the feature in the blue circles in the last three frames moves in constant distance to the tip away from the base.

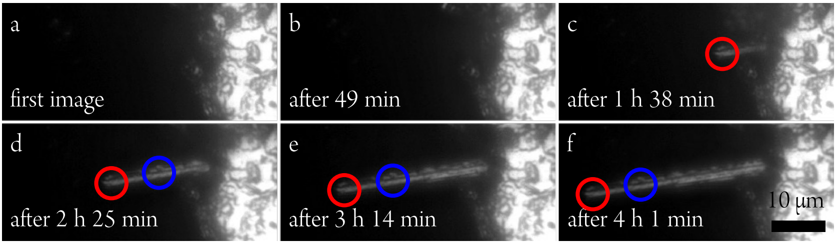

Figure 4.5: Growth of an individual sodium needle during electrodeposition in 1 M $NaClO_4$ in PC at $-20\ \mu A\ cm^{-2}$. The red and blue circle mark features, which do not change their shape and keep the same distance to each other and hence clearly show a growth from the base.

The cell was cycled for a full cycle after the deposition shown in Figure 4.5 at a current rate of $\pm 20\ \mu A\ cm^{-2}$ and three hours per half-cycle, but neither during the dissolution nor the next deposition, the shape of the needle changed. However, in the following dissolution step (also at $20\ \mu A\ cm^{-2}$) a small part in the middle of the needle dissolved. Figure 4.6a shows the electrode at the beginning of this sodium dissolution. In the first hour, sodium was only dissolved from the bulk material as highlighted by the red arrows in Figure 4.6b and c. The dissolution from the needle started afterwards. A section around the middle of the sodium needle dissolved (Figure 4.6d and e). The dissolution from the needle stopped between Figure 4.6d and e. Between Figure 4.6e and f, sodium again only dissolves from the bulk as

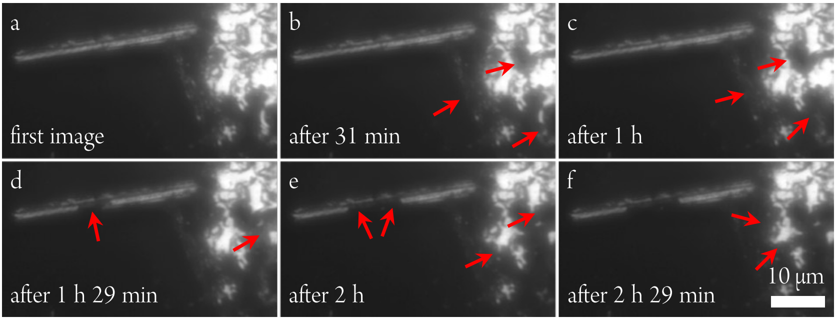

Figure 4.6: Dissolution of bulk sodium and a sodium needle in 1 M NaClO4 in PC at $20\ \mu A\ cm^{-2}$. Red arrows indicate where dissolution occurred in the timespan between each image and the image taken approximately 30 min before.

in the beginning of the dissolution. Wood *et al.*[67] observed a different behavior for lithium and suggested that the electrodissolution of lithium deposits is energetically preferred due to the thinner and more defective SEI compared to the SEI on the bulk lithium. The rather random locations of the electrodissolution of sodium observed here indicates that there is no significant difference between the SEI on bulk sodium and electrodeposits. Therefore, freshly exposed sodium surfaces may passivate quickly in 1 M $NaClO_4$ in PC.

4.4 Conclusion

The comparison between lithium and sodium in Section 4.1 shows that it is not possible to simply replace lithium by sodium and use the analogous sodium salt in the same solvents as electrolyte. Although LP30 (1 M $LiPF_6$ in EC/DMC (1:1)) is not an ideal electrolyte for lithium metal anodes, it allows a stable electrodeposition of lithium and shows at least a partly reversible cycling behavior. In contrast, 1 M $NaPF_6$ in EC/DMC (1:1) is basically not usable for cells with sodium metal anodes since some of the deposits chemically dissolve already during the electrodeposition. A simple experiment to test the applicability of an electrolyte is shown in Section 4.2. By immersing a piece of sodium in an electrolyte and observing the visual changes, the chemical stability of the electrolyte in contact with sodium can be tested. Finding an electrolyte where no visible changes occur during a period of a few days may be a good starting point to continue with further experiments. All of the tested carbonate electrolytes showed visible changes after three days.[174] Since the changes were more subtle for 1 M $NaClO_4$ in PC than for the EC/DMC-electrolytes, this electrolyte was used to study the electrodeposition in more detail in Section 4.3. In these experiments, it was shown for the first time that sodium needles grow from the base. It has been considered before that sodium grows at the base but it was not proven experimentally.[182] The growth of this needle is similar to observations made by Steiger *et al.*[12] for lithium needles, indicating a similar growth mechanism. The observation of the subsequent cycles showed that the electrodissolution occurs at various locations and that these locations can quickly change. The needle grown did not change for a full cycle, while electrodissolution occurred from the bulk sodium. During the second electrodissolution step after the needle had grown, the dissolution started in the middle of the needle, but stopped after about 30 min without any obvious reason. This is in contrast to observation of the cycling behavior of lithium.[67] Wood *et al.*[67] suggested that the electrodissolution from previously grown dendrites is energetically favored and pits in the bulk only start to form when the active lithium in the dendrites depletes. The observations made here, indicate that the electrodissolution occurs at rather random locations. This could be caused by the quick formation of a passivation layer that can easily break and hence exposes unprotected sodium at random locations. If the electrodissolution from deposits is not preferred compared to the dissolution from bulk sodium, as it has been suggested by Wood *et al.*[67] for lithium, excess bulk sodium may convert quickly to porous electrodeposits upon cycling. In such morphologies, so-called dead sodium may form quicker due to electrodeposits that break off the electrode easily. Furthermore, the large surface area of the sodium electrodeposits results in a faster decomposition of the electrolyte. This not very reversible cycling behavior is also supported by low Coulombic efficiencies, which have been reported for this electrolyte.[17]

Since the experience with electrolytes for lithium batteries can hardly be used to conclude on electrolytes that may perform well in sodium batteries, there is a large number of salt-solvent combinations that could improve the performance of sodium batteries. This thesis does not focus on finding an ideal electrolyte, but on the investigation of fundamental growth mechanisms of electrodeposits. The observed growth of a sodium needle exhibits similarities to previous observations of lithium needles by Steiger *et al.*[12]. Since deposition and dissolution are more reliable for lithium and side reactions are less prominent, lithium metal was chosen for further investigations in this thesis.

5 The Electrodeposition of Lithium at Varying Rates

This chapter is published as research article in ChemElectroChem.[176]

5.1 Results

Here the electrodeposition of lithium on lithium on a copper substrate is compared at different rates. Before the experiments, an electrochemical pretreatment was used to cover the electrode with a dense lithium film. This consisted of a seeding step and a deposition of 0.5 mAh cm^{-2} at a rate of −0.5 mA cm^{-2}. After the pretreatment, a different deposition rate was applied to each cell and the deposition was imaged *operando*. The deposition rates investigated in this chapter are −0.05 mA cm^{-2}, −0.5 mA cm^{-2}, −2.5 mA cm^{-2}, −5 mA cm^{-2}, and −10 mA cm^{-2}. Generally, a total charge per area of 5 mAh cm^{-2} (only 4.5 mAh cm^{-2} for −0.5 mA cm^{-2}) was deposited. Additionally, higher deposition rates of −50 mA cm^{-2} and −100 mA cm^{-2} were applied in a test cell with a larger inter-electrode distance to achieve complete lithium ion depletion at the surface of the working electrode.

Figure 5.1a shows a light microscopy image of the electrode after the electrochemical pretreatment. The top of the copper block and the side facing towards the counter electrode are fully covered by lithium. The deposits that are generated during the pretreatment can be seen at higher resolution in Figure 5.1b. The SEM image in Figure 5.1b shows the early stage of a protrusion but away from this site, the result of the pretreatment can be clearly seen: It consists in a surface fully covered by close packed lithium spheres. The growth of the layer during the pretreatment is shown in the Appendix (A.2). The layer thickness measured with the light microscope is approximately in agreement with a layer of randomly close packed equal spheres. It is assumed that the result of each pretreatment of the copper electrode leads to this morphology of the lithium electrode, which consist of densely packed spheres such as the one shown in Figure 5.1b.

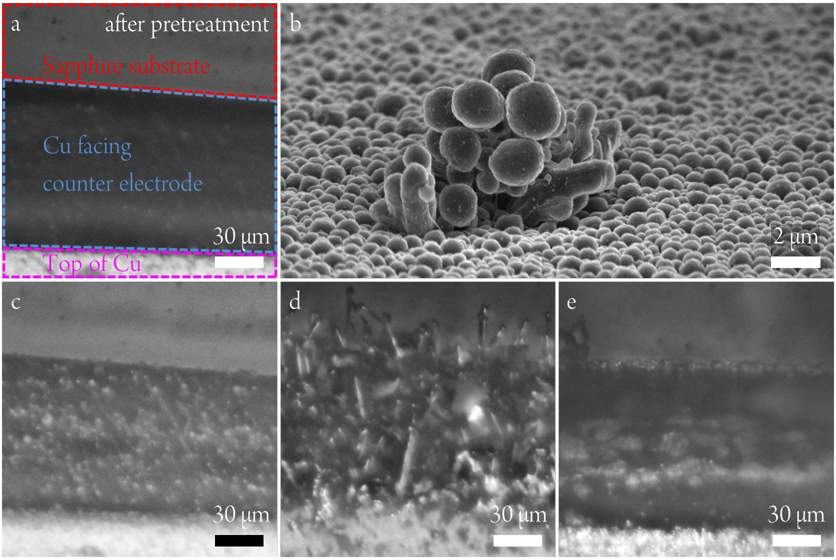

Figure 5.1: (a) Copper electrode after the standard pretreatment (nucleation and the deposition of 0.5 mAh cm^{-2} at −0.5 mA cm^{-2}). The image frame is slightly cropped compared to the schematic in Figure 3.3c. (b) SEM image of initial bush growth at −5 mA cm^{-2} on a dense layer of lithium spheres (5 mAh cm^{-2} deposited after pretreatment). The same area of the electrode from figure a after an additional deposition of 0.5 mAh cm^{-2} (c) and 2.5 mAh cm^{-2} (d) at −0.05 mA cm^{-2}. (e) Copper electrode after pretreatment and the deposition of 0.5 mAh cm^{-2} at −10 mA cm^{-2}. Reprinted from Becherer *et al.*[176]

Figure 5.1c-e compares the lithium deposits that grew after the pretreatment at two very different rates. The growth at the lowest applied deposition rate of −0.05 mA cm^{-2} was observed *operando* with the light microscope and is shown in Figure 5.1c and d and the supporting video SV1[3]. After 10 h at −0.05 mA cm^{-2}, the lithium deposit is considerably rougher compared to the pretreated electrode but evenly distributed over the full electrode and no needles are visible (c). After 50 h of deposition, the electrode is fully covered by long lithium needles (d). In contrast to the rather evenly distributed deposits on the electrode surface at

---

[3] The videos are available online in the supporting information of 10.1002/celc.202100870.[176]

the low rate, the deposition is more localized at higher rates (Figure 5.1e and supporting video SV2[3]). Although the area specific charge in Figure 5.1c and e are the same, the deposits appear to be very different. At the rate of $-10\,\mathrm{mA\,cm^{-2}}$ bushes start to grow at different locations immediately from the beginning of the deposition. In addition to the bush growth in the middle of the electrode (Figure 5.1e), a very fast-growing bush that initiates from the edge of the electrode is visible in the video SV2[3]. It quickly dominates the whole deposition process and soon grows out of the large focus range that was used.

The fast growth of a bush that dominates the deposition was also observed at lower current densities, but did not initiate directly at the start of the deposition as described before for $-10\,\mathrm{mA\,cm^{-2}}$. The *operando* observation of the deposition at $-2.5\,\mathrm{mA\,cm^{-2}}$ is shown in Figure 5.2 and the supporting video SV3[3]. The images in Figure 5.2a, b, and c were recorded after a deposition of charges of $0.67\,\mathrm{mAh\,cm^{-2}}$, $1.33\,\mathrm{mAh\,cm^{-2}}$, and $2\,\mathrm{mAh\,cm^{-2}}$, respectively. Figure 5.2d shows the cell voltage vs. time with marks at the times when the images a-c were taken. An enhanced deposition is apparent at the lower edge of the copper block

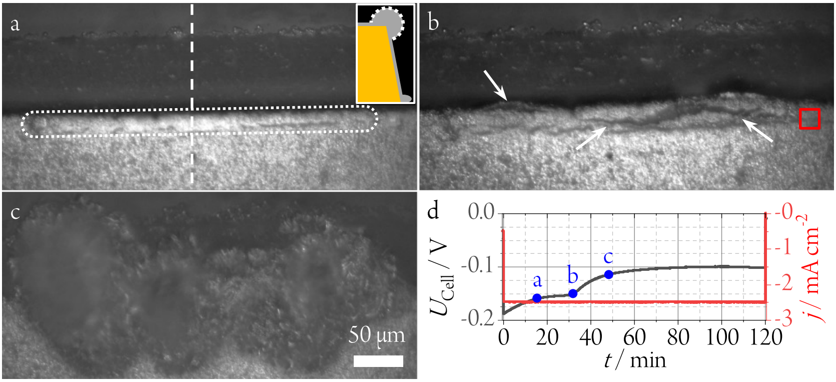

Figure 5.2: *Operando* light microscopy images of the working electrode after 16 min (a), 32 min (b), and 48 min (c) of Li deposition at $-2.5\,\mathrm{mA\,cm^{-2}}$. (d) Galvanostatic voltage vs. time trace with markers that indicate when the images a-c were taken. The short-dashed line (a) highlights the preferred deposition at the upper edge in cylindrical shape and the long-dashed line indicates an exemplary cross section location for the schematic inset (Cu in orange and Li in grey). The arrows (b) highlight the occurring parting in the deposit and the red square marks approximately the location of the SEM image in Figure 5.3c. Modified from Becherer *et al.*[176]

close to the substrate (Figure 5.2a) and especially at the upper edge where a long agglomerate of densely packed electrodeposits (hereinafter simply "dense bush") with a cylindrical shape grows (surrounded by the short-dashed line). To visualize the enhanced deposition, the inset in Figure 5.2a shows a schematic cross section along the long-dashed line. The small bump in the lower right of the inset depicts the deposits at the lower edge and the round lithium deposits at the top of the inset (highlighted with the dashed line) illustrates the enhanced deposition along the upper edge of the copper block in cylindrical shape. The deposition on this dense bush appears faster than in other regions of the electrode, but despite the faster growth, the growth of the dense bush itself is very steady for approximately 30 minutes. However, after slightly more than 30 minutes, a parting in the bush opens up (highlighted by arrows in Figure 5.2b) and the bush starts to grow very fast (Figure 5.2c). The deposition in all other areas of the electrode almost comes to stop after the dense bush parts open and transitions to a fast-growing bush with a more porous structure. The drop in the overpotential of the galvanostatic voltage trace (Figure 5.2d) correlates very precisely with the change from a slow and dense to a fast-growing porous bush. This correlation between cell voltage and deposition morphology was observed in all cells in which a sudden bush growth dominated deposition. In the cell where lithium was deposited at a rate of $-5\ \mathrm{mA\,cm^{-2}}$, the fast bush growth initiated on the top of copper electrode at the edge of the rubber seal (supporting video SV4[3]), which is the location farthest away from the lithium counter electrode. Therefore, it can be excluded that the drop in overpotential is associated with a reduction of the inter-electrode distance. Although the large bushes in the supporting videos SV2[3], SV3[3], and SV4[3] partly grow out of focus, it can be clearly observed that none of them shows a tip-growth behavior but rather a three-dimensional volumetric growth mechanism that was previously reported and compared to the rising dough of a raisin bread.[49] The dominating fast bush growth even occurred at $-0.5\ \mathrm{mA\,cm^{-2}}$ (last 3 s of supporting video SV5[3]), but it was triggered after the deposition of a considerably larger amount of lithium than for the higher rates. For $-0.5\ \mathrm{mA\,cm^{-2}}$, approximately $4.1\ \mathrm{mAh\,cm^{-2}}$ were deposited after the pretreatment before the bush growth started, while it was only about $1.33\ \mathrm{mAh\,cm^{-2}}$ and $1.25\ \mathrm{mAh\,cm^{-2}}$ for $-2.5\ \mathrm{mA\,cm^{-2}}$ and $-5\ \mathrm{mA\,cm^{-2}}$, respectively. At a rate of $-10\ \mathrm{mA\,cm^{-2}}$, the fast bush growth initiated immediately after the start of the deposition.

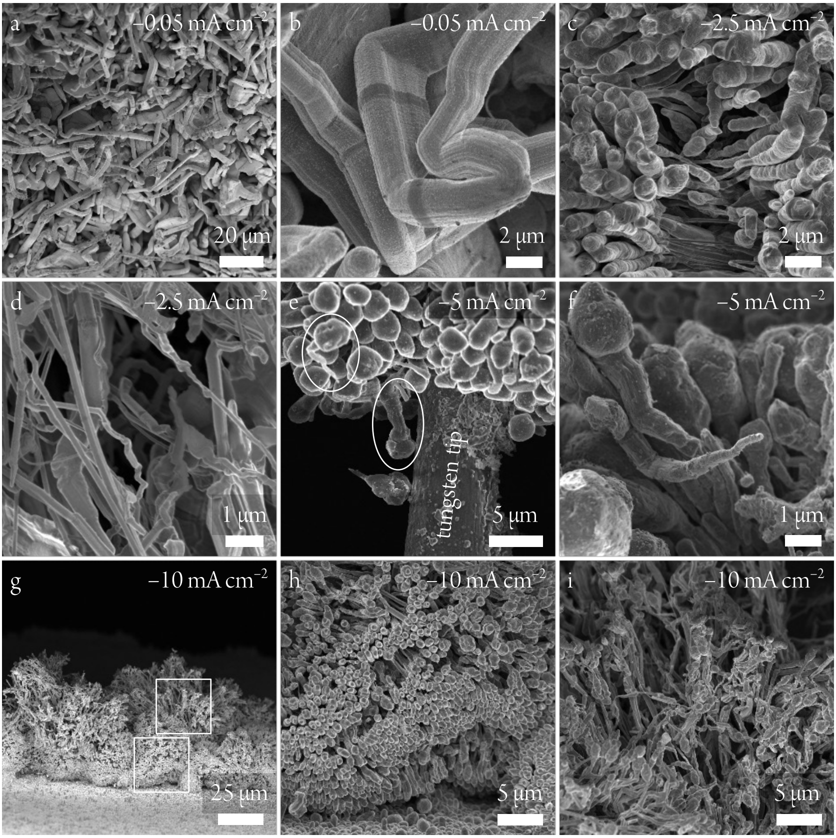

Figure 5.3: SEM images after the electrodeposition of 5 mAh cm^{-2} at various rates. (a) Overview of the morphologies visible after the deposition at −0.05 mA cm^{-2} and (b) an exemplary needle with multiple high-angle kinks. (c) Columnar grown deposits that form a dense structure, which parted open during the deposition at −2.5 mA cm^{-2}. The location of this image is approximated and highlighted by a red square in Figure 5.2b. The orientation of the images is rotated by 90 °: the trench is from the bottom up in figure c and from left to right in Figure 5.2b. (d) The structures in the inside of the fast-grown bush at −2.5 mA cm^{-2}. (e) A dense lithium bush grown at −5 mA cm^{-2} was mechanically opened with a tungsten tip on a micromanipulator. (f) Deposits inside of the bush after it was opened. (g) Overview of a fast-grown bush at −10 mA cm^{-2} and a magnified view on the dense lower part of the bush (h) und the upper part that is porous and unstructured (i). Focus stacking (see Section 3.2.3) was used to increase the DOF in image c (stack with four images) and d (stack with three images). Reprinted from Becherer *et al.*[176]

Figure 5.3 gives an overview of characteristic morphologies of the lithium deposits obtained at different rates. After a deposition at $-0.05\,\mathrm{mA\,cm^{-2}}$ the electrode surface is covered by long needles but also by some lithium flakes with considerably larger dimensions than the diameters of the needles. Some of the needles have multiple kinks (some with high angles) and a few needles are connected to the electrode at both ends to form loops (Figure 5.3a and b). At rates of $-2.5\,\mathrm{mA\,cm^{-2}}$ and higher, deposition was localized and large areas of the electrodes were not altered and still covered with a dense film of lithium spheres, which already grew during the pretreatment, as shown in Figure 5.1b and in the lower part of Figure 5.3g. Bush growth typically initiated at various locations but usually one or only a few bushes dominated the growth when a transition to fast-growing bushes occurs. This transition coincides with a drop in the cell overpotential (Figure 5.2d). A high-resolution image of a small bush that grew at the beginning of the electrodeposition but stopped to grow when other bushes started to dominate the deposition can be seen in Figure 5.1b. Since the fast-growing bushes grew very large and hence were extremely fragile, large parts of them broke off the electrodes and these parts could not be transferred by SEM. Therefore, at the higher rates mainly smaller bushes that grew at the beginning of the deposition and the parts of the fast-grown bushes that were closer to the electrode surface and did not break off were imaged in the SEM. For the electrode on which lithium was deposited at a rate of $-2.5\,\mathrm{mA\,cm^{-2}}$, the large bush shown in Figure 5.2c partly broke off but significant parts remained on the electrode and could be imaged. Figure 5.3c shows the right edge of the parting of the cylindrical bush (Figure 5.2b). Here, the initially dense bush opened but the rapid growth did not occur at the edge of the resulting trench. Outside of the parting, columnar lithium needles are very densely packed. When looking at the trench it becomes apparent that the diameter of these columnar grown deposits reduces significantly towards their base, resulting in shapes that share similarity to baseball bats. In order to better observe the inside of the fast grown bush (Figure 5.2c), the remaining parts of the bush were mechanically opened with a tungsten tip on a micromanipulator (Kleindiek Nanotechnik GmbH) inside the SEM. Figure 5.3d shows the inner part of the bush after opening it. The morphology of the deposits differs significantly to Figure 5.3c and appear much less uniform and less dense. Long fiber-like deposits with extreme aspect ratios and diameters partly below 100 nm grow next to deposits with diameters close to 1 µm. Furthermore, some deposits have long facets, while others are kinked and almost crinkled. For the deposition at $-5\,\mathrm{mA\,cm^{-2}}$ the bush that grew mainly in the first half of the deposition at the lower edge of the electrode (supporting video SV4[3]) was examined. From the outside, the bush appeared very dense and the micromanipulator was again used to examine the inside of the bush. Figure 5.3e shows a lithium deposit together with the tungsten tip that sticks inside. This reveals that deposits contain densely packed spheres at their outside and segments with smaller diameter behind them (highlighted by ellipses). Figure 5.3f was recorded after parts of the bush had been scraped off by the micromanipulator. Generally, the morphology is similar to the one observed at $-2.5\ \mathrm{mA\ cm^{-2}}$ (Figure 5.3c) with the difference that the diameter reduces abruptly behind the spherical tip instead of a more gradual reduction in diameter. Figuratively described: The shape resembles rather a tadpole than a baseball bat. For the deposition at a rate of $-10\ \mathrm{mA\ cm^{-2}}$ the bush in Figure 5.3g-i has been identified to be representative for bush growth at high rate (Appendix A.3). The lower part of the bush close to the electrode surface (Figure 5.3h) is very dense and exhibits broader tips and has reducing diameters towards the inside of the bush. It is similar in morphology to Figure 5.3c and e. The upper part (Figure 5.3i) is less dense with very irregular shapes similar to the fast-grown deposits in Figure 5.3d.

To summarize the different morphologies obtained with the variation of the deposition rate, Figure 5.4 compares the deposition of $1\ \mathrm{mAh\ cm^{-2}}$, $2\ \mathrm{mAh\ cm^{-2}}$, and $3\ \mathrm{mAh\ cm^{-2}}$ at different rates. Each column of the image corresponds to one cell with a fixed deposition rate and each row contains images of these cells after the same amount of area specific charge. After the deposition of $1\ \mathrm{mAh\ cm^{-2}}$ a roughened surface is visible at deposition rates of $-0.05\ \mathrm{mA\ cm^{-2}}$ and $-0.5\ \mathrm{mA\ cm^{-2}}$. For $-0.05\ \mathrm{mA\ cm^{-2}}$ the first lithium needles just form, whereas at $-0.5\ \mathrm{mA\ cm^{-2}}$ some short needles are clearly visible. In contrast to the more evenly distributed deposits at lower rates, a preferred deposition at the upper and the lower edge of the electrode can be observed for $-2.5\ \mathrm{mA\ cm^{-2}}$. At the highest rate of $-10\ \mathrm{mA\ cm^{-2}}$, a fast three-dimensionally growing bush initiates at the beginning of the deposition and quickly dominates the deposition process. After the deposition of $1\ \mathrm{mAh\ cm^{-2}}$ it already covers a significant part of the electrode. The out of focus area of this bush clearly shows growth towards the cell window, i.e., perpendicular to the direction towards the counter electrode. After the deposition of $2\ \mathrm{mAh\ cm^{-2}}$, the electrodes are covered by needles for the lower rates of $-0.05\ \mathrm{mA\ cm^{-2}}$ and $-0.5\ \mathrm{mA\ cm^{-2}}$, but the needles are significantly longer for the lowest rate of $-0.05\ \mathrm{mA\ cm^{-2}}$. In both cases small loops, i.e., kinked deposits that seem to be connected to the electrode at both ends, are visible (insets). At the rate of $-2.5\ \mathrm{mA\ cm^{-2}}$, the

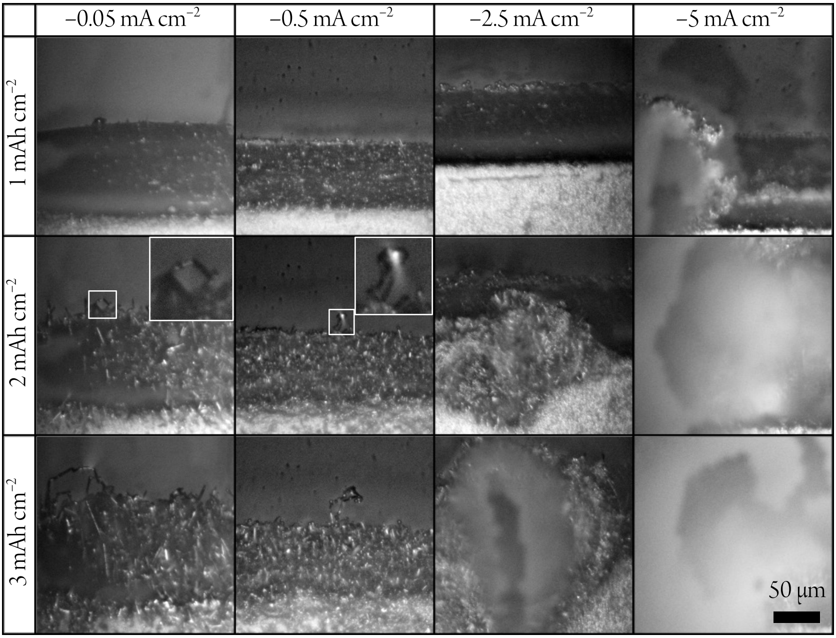

Figure 5.4: Comparison of the electrodeposits after 1 mAh cm^{-2}, 2 mAh cm^{-2}, and 3 mAh cm^{-2} were deposited at −0.05 mA cm^{-2}, −0.5 mA cm^{-2}, −2.5 mA cm^{-2}, and −10 mA cm^{-2}. Reprinted from Becherer *et al.*[176]

bush at the upper edge parts open and a fast-growing bush started to grow (compare Figure 5.2). At −10 mA cm^{-2}, the growth rate of the dominating bush seems to accelerate over time. After the deposition of 2 mAh cm^{-2} the electrode depicted in the image is already fully covered with the bush that grew out of focus. After a deposition of 3 mAh cm^{-2} the electrodes with the two lower deposition rates are still covered by needles, which are significantly longer at the rate of −0.05 mA cm^{-2}. On both electrodes, it is notable that loop-structures grow particularly fast. At the higher rates, the large bushes continue to dominate the growth and at −2.5 mA cm^{-2} the bush also starts to grow out of focus.

Higher current densities were applied in the modified test cell with a larger inter-electrode distance, and an objective with a lower magnification was used to ensure that the deposits did not grow out of the field of view. During the deposition at −50 mA cm^{-2} no significant

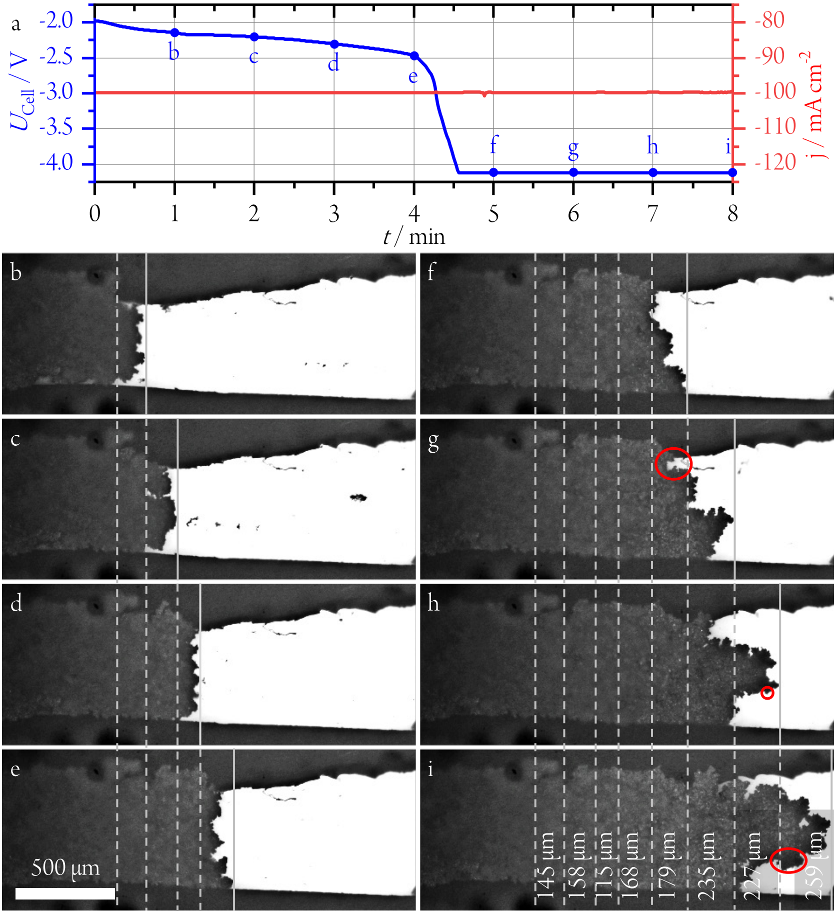

Figure 5.5: (a) Cell voltage at a deposition rate of −100 mA cm^{-2} with marks to indicate when the image stacks (b-i) were acquired. (b-i) The cell with the growing lithium bush. Compared to the standard cells in other images, the images of this cell have been rotated by 90 °clockwise. The Cu block is to the left but outside of the images since the lithium has already grown to a 1.5 mm thick bush during the deposition at −50 mA cm^{-2}. The lithium counter electrode is outside of the images to the right. The dark areas at the top and bottom of each frame is the rubber sealing that borders the cell from all sides. The images were acquired after each full minute from minute 1 to 8 of deposition at −100 mA cm^{-2}. The solid gray lines in all images mark the front of the lithium bush and the dashed lines marks where the front of the bush was in the previous images. Modified from Becherer *et al.*[176]

differences in growth and the galvanostatic voltage trace compared to the deposition at -10 mA cm^{-2} were observed. After the deposition of 16.7 mAh cm^{-2}, the current density was increased to -100 mA cm^{-2} and after slightly more than 4 min a sudden rise in the cell overpotential occurred, which is shown in Figure 5.5a. This behavior clearly indicates the depletion of ions close to the surface of the negative electrode.[62, 63] Charge neutrality requires that both cations and anions change their concentration in the same way. After approximately 4.5 min the deposition changes to a potentiostatic lithium plating as the voltage range of the potentiostat of ±4 V was reached. Nevertheless, the applied current was almost constant within the first 8 min of the deposition and hence the amount of plated lithium per minute was constant in the time span shown. Figure 5.5b-i show the cell during the deposition at -100 mA cm^{-2}. The time between the images is one minute. The solid lines in each image mark the front of the growing bush, while the dashed lines contain the deposition front of the previous images. The front of the bush moves between 115 µm and 259 µm per minute. Except at the front of the bush, the full width of the cell is visually covered by lithium. Furthermore, the height of the deposit exceeds the height of the electrode since the top of the deposit is mostly out of focus. Therefore, the lithium bushes at this high rate have to be very porous since only 1.67 mAh cm^{-2}, corresponding to a dense lithium film of 8.1 µm, are deposited per minute. The bush grows by 586 µm within the first four minutes of the deposition and by 900 µm within the following four minutes, indicating that the electrolyte depletion accelerates the growth. However, no distinctive change in the growth mechanism is apparent in our setup. Surprisingly, even after the depletion of the electrolyte, the deposition does not solely occur at the tip of the growing bush. The tip of the deposits in Figure 5.5g is considerably closer to the counter electrode than all other regions and in the depleted electrolyte a growth solely at that tip could be expected. However, the gap between the lithium and the rubber seal (surrounded by a red line in Figure 5.5g) is closed in Figure 5.5h and i despite being far from the tip of the deposit. Furthermore, the feature surrounded by the red lines in Figure 5.5h and i clearly indicates that growth does not only occur at the tip. The feature is pushed towards the counter electrode, demonstrating the growth that occurs behind this feature. The growth of the feature itself is also not directional towards the counter electrode as one might expect, it grows partly even in the opposite direction, towards the negative electrode. The backward growth can be best seen in video SV6[3]. The video also shows particles that break off from the lithium counter electrode due to its fast dissolution. The motion of these floating particles may be used to infer on convection in the electrolyte.

The large bush broke apart when the cell was opened and washed in DMC. A TEM grid was used to collect various parts from the disconnected deposits. Three SEM images with increasing magnification of an exemplary bush can be found in the Appendix (Section A.4). Just as the other bushes, this bush exhibits a hierarchical structure. This can be seen by comparing Figure A.4a and b, which look similar despite the about ten times higher magnification. Even at this rate, the basic elements of the bush are needles and flakes (Figure A.4c and d). The needles appear to be shorter than the ones found at lower rates and short needles and flakes are sometimes hard to distinguish. Figure A.4d shows a different region of the deposit where the needle-like shapes are more pronounced. These needles are kinked and have facets. The facets are even more notable on the larger flakes. It appears that at short range, the deposits are quite densely packed. Voids exist in agglomerates of these densely packed units and there is an increasing size of voids when the agglomerates get larger. This results in a loosely packed porous and hierarchical structure. In this respect, there seems to be no conceptual difference to bushes grown at lower rates.

5.2 Discussion

Lithium was electrodeposited at different rates. Between the slowest and the most accelerated conditions, the deposition rate was varied by a factor of 2000 and consequently differences in the morphology of the deposits appeared. Surprisingly, also many similarities were found in the deposits and in the growth mode. At low rates, the deposits can be described by a homogeneous distribution of needles that grow from the base. With increasing current density, the deposition became less homogeneous and bushes of interconnected needles grew at various sites. After a certain time or due to further increasing the rate, an abrupt transition from the growth of these dense bushes to fast-growing individual porous bushes was commonly found. The highest rates caused a sudden increase in the cell overpotential. Even at these extreme conditions, no significant change in the growth mode was found. Based on the visual observations, it is inferred on the dominant mechanisms of growth and the findings are related to models available in the literature.

5.2.1 Variation of Rates and Resulting Morphologies

The deposition rate was varied between −0.05 mA cm^{-2} and −100 mA cm^{-2}. At the lowest rates, mainly individual needles grew evenly distributed over the whole electrode surface from the lithium spheres that were deposited during the pretreatment (supporting videos SV1^{3} and SV5^{3}). These needles have facets, indicating crystalline growth with different growth rates along different crystal directions. At early stages, the needles clearly grow from the base, but with longer deposition times, an increasing number of kinked needles and loops appear that also grow between kinks. This indicates a growth mechanism based on the insertion into defects as suggested before.[12] The defects can be in the SEI and/or in the underlying lithium metal. SEI defects might be inhomogeneities in the chemical composition, cracks, or small regions that are very thin. In the lithium, the defects are associated with kinks, which typically contain grain boundaries, i.e., small regions that contain high amounts of dislocations and vacancies. A defect in the SEI and in the lithium crystal might be linked: e.g., the SEI on top of a grain boundary could differ from the one that forms on top of a perfect lithium crystal. This is plausible because the SEI varies depending on the orientation of the underlying lithium.[183] As already observed by Yamaki *et al.*,[11] crystalline defects (tips and kinks) can control later stages of growth. They and others[71, 184] attribute the early growth of the whiskers to a mechanism based on the release of mechanical stresses and the extrusion of metal. This mechanism seems not to be required to nucleate needles as can be seen from experiments where needles directly grow on copper and from experiments where needles form during physical vapor deposition without SEI and electrochemistry.[72]

When comparing the deposition at low rates of −0.05 mA cm^{-2} and −0.5 mA cm^{-2}, it is striking that the individual needles at −0.05 mA cm^{-2} grow considerably larger when equal charge is applied. It is plausible that during very slow deposition, defects in the SEI are less significant since the cracks in the SEI, which are inevitable when the lithium deposits grow, have enough time to heal by creating fresh SEI-layers. Therefore, at very low rates the crystalline growth of lithium appears to dominate the deposition. This supports the previously reported assumption that it is an intrinsic behavior of lithium to form needles at room temperature[72] and indicates that the growth of single crystalline lithium needles is favorable at the lowest deposition rates. As a consequence, concepts that solely use large electrode surface areas (porous nickel, porous copper, lithium particles, large surface area carbon) to reduce the effective current density, may not be effective in preventing needles. At higher rates, defects and inhomogeneities in the SEI might play an increasingly important role in the growth mechanism since their healing does not occur fast enough. This might also be the reason for the observed localized bush growth at rates of $-2.5\,\mathrm{mA\,cm^{-2}}$ and higher. When lithium is deposited fast enough at a location where the SEI is thin and defective, fresh lithium surface is constantly generated, i.e., the SEI remains thin. This could result in a self-amplifying deposition mechanism and hence a deposition occurs on a decreasing number of bushes with increasing rate. Although the growth was observed to increasingly localize with increasing rate, the morphology of the individual deposits changes only slightly and still consists of the same building blocks: agglomerates of needles and some flakes. At higher rates, the deposits appear more disordered, ligament shapes become more rounded and less facetted, the diameters of the needles vary to a greater extent, and especially in dense bushes the diameter of individual needles changes significantly over their length. The ordered regular branching, as is typical, for example, for solidification dendrites, was not found in the experiments. The shape of the bushes suggests that branching rather is of random nature. It was observed that lithium bushes, at all rates, grow non-directionally from the inside. This was already reported for low rates and compared to the raisin bread expansion model.[49] At lower rates, localized bush growth did not occur or only after the deposition of large amounts of lithium. However, the loops observed at low rates show a geometrically similar expansion since they grow between kinks and hence the kinks grow apart from each other. The growth of bushes from the inside and the growth between kinks are hard to explain by the well-known growth models based on effects of the substrate or ion depletion and electrical fields in the electrolyte. Therefore, a defect-driven insertion is suggested as the dominating growth mechanism at all rates.

5.2.2 The Abrupt Transition to Fast Bush Growth

For all cells with current densities between $-0.5\,\mathrm{mA\,cm^{-2}}$ and $-5\,\mathrm{mA\,cm^{-2}}$, a sudden transition to a localized fast bush growth was observed. For the lowest current density of $-0.05\,\mathrm{mA\,cm^{-2}}$, such a transition was not observed and for the higher current densities, these fast-growing bushes occurred already at the beginning of the deposition. In all cases, the transition of the growth mode coincided precisely with a drop in the overpotential. As a depletion of the electrolyte would result in an increase in the cell overpotential, this transition cannot be caused by such a depletion. In one case, the bushes initiated at locations farthest from the counter electrode. Since the voltage drop correlates precisely with the occurrence of the bushes and long before they grow over the front of the copper block, a reduction of the inter-electrode distance can be excluded as cause for the drop in overpotential. It is plausible that a fast-growing bush has not only more surface area, but also more crystalline defects at which lithium can be inserted into the deposits and hence reduces the effective current per defect, resulting in a lower resistance of the cell. Additionally, the SEI on these fresh and fast-growing deposits has to be thin and defective, resulting in a faster transport through the SEI at an increasing number of insertion locations. The almost ignition-like start of the fast bush growth is most likely triggered by sudden exposure of areas without a protective SEI layer. Since the cell geometry is not significantly altered due to the growth of this bush, the drop in overpotential (Figure 5.2d) is caused by larger electrode surface area with thinner SEI. This indicates that a relatively large fraction of the overpotential originated from the SEI and not only from the liquid electrolyte. The importance of the SEI for the growth of dendrites has been emphasized by Cohen *et al.*[9] and Aurbach *et al.*[5]. According to the findings in this work, the morphology of the deposits shows that they are crystalline. The size of the crystallites (e.g., the length of the segments) reduces with increasing rate. During electrochemical or physical vapor deposition of metals, the generation of crystalline defects (e.g., dislocations or GBs) and their healing compete. At low rates, the system is closer to thermodynamic equilibrium and less defects form, which results in larger grains or crystallites. This is also found for the growing lithium structures and emphasizes the importance of crystalline defects. In the experiments of this thesis, the SEI also seems to contribute: Small-scale defects in the SEI but also in the underlying lithium may be responsible for growth of needles with kinks, while larger cracks or delamination of SEI result in the onset of individual fast-growing bushes.

During the deposition at $-5\,\mathrm{mA\,cm^{-2}}$, the fast-growing bushes initiate at the edge of the rubber seal that was placed on top of the copper block and SEM examination of the block revealed deposits underneath the rubber seal (Appendix A.5). It is presumed that before the fast growth was triggered, the seal had been slightly moved or lifted by the deposited lithium and hence the bare copper without a protective SEI was suddenly exposed, allowing the initiation of a fast and localized bush growth. Although this example is very specific to the used *operando* cells, it clearly demonstrates the effect what happens when fresh surfaces are exposed. In real cells, this could be the delamination of protective films, the movement of a separator, or could happen when so-called dead lithium breaks off. Furthermore, during the deposition at $-2.5\,\mathrm{mA\,cm^{-2}}$, fast growth was triggered on a thick layer of lithium that was deposited before and far away from all rubber seals. Here a dense lithium bush opens probably due to mechanical stress that developed during growth, and it is very likely that this results in considerable damage to the SEI. To the best of the authors knowledge, the correlation of the initiation of fast bush growth and a drop in the overpotential was not reported before, which is probably caused by two reasons. First, to detect this very localized phenomenon, the observation of large regions at high resolution is required. Second, at moderate rates this only happens after significant charge has been applied. In many deposition experiments, not enough lithium is deposited to detect this phenomenon. In cells with reasonable capacities (~3 $\mathrm{mAh\,cm^{-2}}$[185]) this effect is expected to be detectable.

5.2.3 The Ionic Depletion of the Electrolyte

The evolution and growth of dendrites is often attributed to the ionic transport within the electrolyte. Transport limitations are obviously relevant for highly diluted solutions as described by Chazalviel[8] and might be relevant for polymer electrolytes as discussed by Monroe and Newman[10]. The transport limitation is described by the limiting current density $J_{\mathrm{lim}} = \frac{2z_C c_0 F D}{L(1\text{-}t_C)}$ [10, 62, 63]. For the high rate cell with an inter-electrode distance of $L = 4.1$ mm, a cationic charge number $z_C = 1$, an initial salt concentration in the electrolyte of $c_0 = 1$ M, the Faraday's constant $F = 96485\,\mathrm{As\,mol^{-1}}$, a salt diffusion coefficient D in a range $2 \dots 4 \cdot 10^{-6}\,\mathrm{cm^2\,s^{-1}}$[118, 186, 187], and a cationic transference number t_C in a range from 0.25 to 0.45[118, 186, 187], the limiting current density J_{lim} is expected to be in the range $1.3 \dots 3.4\,\mathrm{mA\,cm^{-2}}$. No pronounced rise of the cell overpotential, as expected and reported for complete ion depletion,[62, 63] was observed at a current density of $-50\,\mathrm{mA\,cm^{-2}}$, which is significantly higher than the calculated limiting current density. In the next step of the experiment, the current density was increased to $-100\,\mathrm{mA\,cm^{-2}}$. Due to the previous deposition at $-50\,\mathrm{mA\,cm^{-2}}$, the inter-electrode distance L reduced to approximately 2.6 mm at the beginning of the deposition with $-100\,\mathrm{mA\,cm^{-2}}$ (relative to the original surface area) and hence the range for the expected limiting current density changed to $J_{\mathrm{lim}} = 2.0 \dots 5.4\,\mathrm{mA\,cm^{-2}}$.

The theoretical Sand's time $\tau_{\mathrm{Sand}}=\pi D\left(\frac{z_{\mathrm{C}} c_0 F}{2j(1-t_{\mathrm{C}})}\right)^2$ [62–64] is between 2.6 s and 9.7 s for this experiment, but the observed increase in cell potential occurred after approximately 4 minutes. Sand's behavior did not occur at the calculated limiting current density. Instead, it occurred only for higher current densities and significantly later than calculated. This is expected as convection is not negligible in experimental cells with large volumes of liquid electrolyte. Convection is evident in the used cell (supporting video SV6[3]), although the cell is relatively narrow and has a volume that was estimated to be below 3.25 µl. Bai *et al.*[63] performed experiments with larger inter-electrode distance and significantly smaller electrode surfaces in cells that even reduce their diameter towards the middle of the cell. It seems plausible that with their extreme dimensions, convection is almost negligible and hence their experimentally measured Sand's time is closer to the calculated one.

It has been observed – even after the cell overpotential rose abruptly – that a deposition of lithium that is not very directional and does not solely occur at the tip of the deposits. This growth inside the lithium structure (instead of at locations closest to the counter electrode) does not coincide with any model previously reported in literature, where severe depletion inevitably induces tip growth. This indicates that the deposition of lithium is far more complex than described by these models, which are usually based on a one-dimensional ion depletion zone. Moreover, these observations imply that concepts that aim in preventing tip growth[87] may not be effective for preventing dendrites. Even at the extreme conditions with a cell potential of −4 V, where electrolyte depletion is certainly present, the observed deposition does not appear to be dominated by the transport limitations in the liquid electrolyte. A possible explanation for the observed behavior is a very complex geometry of the three-dimensional depletion zone in the electrolyte, which is presumably not homogeneous and not stationary due to the growing structure in combination with convection in the electrolyte. If the electrolyte is not fully depleted within a few small spots, lithium can be deposited from there. If these spots are small, no significant drop in the overpotential would be observed. The growth from the inside of the lithium bushes indicates that even at these extreme conditions the growth mechanism is still governed by the insertion into defects and hence a deposition is not possible at any location of a lithium bush, e.g., the tips of deposits. Since the SEI is inevitably thin on the surfaces of fast-growing bushes, the SEI may not define preferred insertion sites and crystalline defects seem to play an important role in the growth mechanism. One might also imagine that the growth of lithium can occur in regions of ionic depletion due to the surface diffusion of lithium atoms. In this case, the first step of lithium deposition, the electron transfer, happens at another place than the crystallization. This atom diffusion mechanism could explain growth sites in some limited distance away from the electrochemically active sites.

In summary, no significant change in the growth mechanism was observed despite the ionic depletion within the electrolyte.

5.2.4 Implications for Real Cells

The electrodeposition of lithium is important for future lithium metal secondary batteries where it is part of the operating principle but also very critical in the current lithium-ion technology, where lithium dendrites are considered to be a safety risk. In the performed experiments, it was hardly possible to reach ion depletion in commonly used liquid electrolytes for lithium-ion batteries for all current rates that are relevant for practical applications. Even when ion depletion was forced during the *operando* observations, it had only minor impact on the growth mode. Bai *et al.*[63] demonstrated depletion and fractal growth at considerably lower current densities. These differences in the observations are probably caused by convection, which might be negligible in the capillary cells of Bai *et al.* In commercial cells, separators probably suppress convection completely. However, the inter-electrode distance in commercial cells is two to three orders of magnitudes smaller than in the capillary cell of Bai *et al.*, resulting in significantly higher limiting current densities. To estimate the impact of ion depletion in commercial cells, the limiting current density was calculated for an exemplary high power 18650 lithium-ion cell. For the Sony VTC5A cell, used for this calculation, the limiting current density was more than 100 times higher than the maximum continuous charge current density for this cell (see Appendix A.6). Therefore, Sand's behavior seems to be irrelevant for practical cells with liquid electrolytes. This suggests that initiation and growth of the notorious dendrites in lithium-ion cells is not controlled by concentration gradients in the electrolyte. In contrast to the hardly relevant ion depletion, the fast-growing lithium bushes, which can already occur at lower deposition rates, are likely to play a very crucial role and might be the main safety concern of lithium-ion cells and an obstacle in the commercialization of lithium metal anodes in rechargeable batteries. The porous bushes exhibit large surface areas and hence result in a significant electrolyte consumption. Furthermore, they result in an extreme volume expansion, causing mechanical stresses within the cell. Separators damaged by large structures and not by single needles have recently been observed.[188] A major problem is the formation of dead lithium during discharge[49] and a sufficient Coulombic efficiency seems hardly possible when lithium is deposited as bushes.

5.3 Conclusion

Operando light microscopy at the physical resolution limit of light was used to obtain a clear picture of growth modes during electrodeposition of lithium from a liquid electrolyte. The aim of this study was to identify the rate dependence of the growth. An almost flat deposition of lithium spheres was achieved for the deposition of 0.5 mAh cm^{-2} during the pretreatment and at lower rates for another 0.5 … 1 mAh cm^{-2}. However, after the deposition technologically relevant amounts of charge, a flat deposition could not be achieved at any rate in the carbonate-based electrolyte (EC/DMC). In the experiments, the rates were varied by a factor of 2000 and different deposits grew at different rates. The shapes of the deposits vary, but despite the large rate variations, they also show similarities. At all rates a large number of facetted elements can be found in the deposits, indicating crystalline lithium growth. For very low rates, the deposits consist of needles that are quite evenly distributed across the electrode. For increased rates, the needles become shorter and contain more kinks. Lithium insertion happens at the base and at kinks. These sites are defects in the crystalline lithium structure but also in the SEI that probably alleviate lithium insertion. This leads to facetted crystalline lithium segments, which are building blocks of the growing structures. Further increasing the rate causes the formation of bushes that grow from their inside and still contain facetted and kinked elements. In this regime, growth can abruptly localize onto an individual bush, which then dominates the whole deposition process. The results suggest that the exposure of surfaces without SEI can trigger this transition. Here the defects in the SEI are probably considerably larger than the other type of SEI defect, which is found in the altered SEI on top of a kink in a facetted needle. Fresh metal can be exposed by the movement of cell components, delamination of the SEI, or the breakage of a deposit. Bushes, which are based on the crystalline building blocks, are the dominating lithium structures up to highest rate. Even when the voltage indicates ionic depletion within the electrolyte, bushes dominate electrodeposition and their growth mode does not change. This suggests that for the safety of real cells the depletion of cations and the localization of growth onto an individual protrusion is not as relevant as accelerated bush growth.

6 The Growth Mechanism of Lithium Dendrites and its Coupling to Mechanical Stress

This chapter is published as full paper in the Journal of Materials Chemistry A.[177]

6.1 Results

Before each experiment, a dense film of lithium was electrodeposited onto a copper substrate (see Section 3.3.1). In this chapter, the electrodeposition of lithium at −0.05 mA cm^{-2} onto this lithium film is studied. Additional data for −0.5 mA cm^{-2} can be found in the Appendix A.8. During the experiments, many needles grow on the electrode. They evolve in length and some form kinks and generally grow as described in Chapter 5. At later stages of needle growth, it becomes evident that certain structures grow particularly fast. These structures

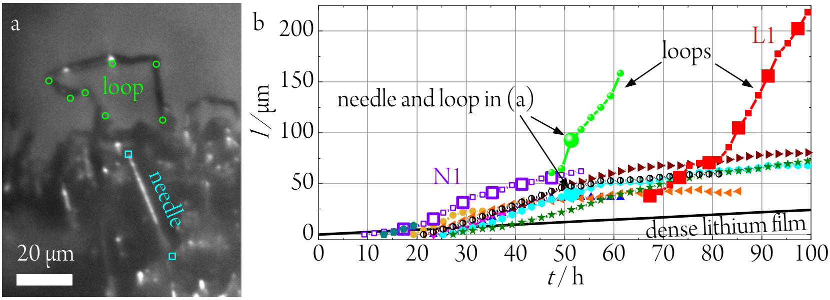

Figure 6.1: (a) A needle and a loop after approximately 51 h deposition at −0.05 mA cm^{-2}. (b) The lengths of ten needles and two loops (represented by different colors) during the lithium electrodeposition at −0.05 mA cm^{-2}. The black line is the calculated thickness of a dense lithium film. Large markers for the needle N1 and the loop L1 indicate when the images in Figure 6.2 and Figure 6.3 were taken. Reprinted from Becherer *et al.*[177]

with multiple kinks are attached to electrode at both ends and from now on will be referred to as loops.

Figure 6.1a shows an exemplary needle and a loop. The cyan squares indicate the base where the needle nucleated and the tip of the needle (cyan plot in Figure 6.1b). The green circles highlight all visible kinks of the loop (green plot in Figure 6.1b). Figure 6.1b shows the evolution of the lengths of ten arbitrarily chosen needles and two loops. The total length of each loop is the sum of the lengths of all visible segments between neighboring kinks calculated from 3D data based on the image stacks (see Section 3.2.3). The segments at the base of loops are typically covered by other lithium deposits and hence are not visible. Therefore, the length of the loops shown in Figure 6.1b is an underestimation of the actual length. The black line in Figure 6.1b is the calculated thickness that a dense lithium film, deposited at the same current density, would have. The growth of both, needles and loops, is considerably faster than the growth of a dense film.

The observed needles nucleated between 9 and 27 hours after the start of the experiment. After nucleation, they typically exhibit accelerating growth that later diminishes and eventually the growth stops (e.g., the orange triangles in Figure 6.1b). The total length of needles that stopped varies between ~20 μm and ~80 μm. The growth of the needle N1 is shown in

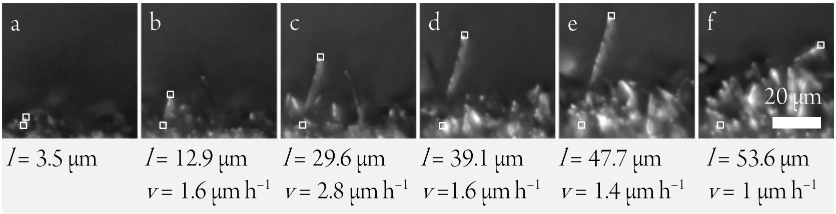

l = 3.5 μm | l = 12.9 μm, v = 1.6 μm h^{-1} | l = 29.6 μm, v = 2.8 μm h^{-1} | l = 39.1 μm, v = 1.6 μm h^{-1} | l = 47.7 μm, v = 1.4 μm h^{-1} | l = 53.6 μm, v = 1 μm h^{-1}

Figure 6.2: (a) Needle N1 after nucleation. (b-f) 6 hours of deposition at −0.05 mA cm^{-2} between the images. White squares in the lower left of each image marks the position of nucleation, while the second square marks the tip of the needle. The larger markers in the N1-plot of Figure 6.1b indicate when the images (a-f) were recorded. Modified from Becherer *et al.*[177]

Figure 6.2 and the supporting video SV1[4], where a growth from the base of the needle is clearly visible. This base growth was typically observed for needles without kinks. The velocities given in Figure 6.2b-f increase initially and decrease later. Between Figure 6.2e and f, a kink appeared and the distance between base and tip does not represent the length of the needle anymore. Kinking of some needles and the blocking of the view onto the tip caused by other deposits complicated the length measurements at later times. In spite of these experimental difficulties, the observed deceleration of the growth as seen in Figure 6.1b, is a real and general trend.

Compared to needles, loops appear later in the experiments. In Figure 6.1b, it becomes apparent that loops can grow significantly faster than the needles. The growth of the loop L1

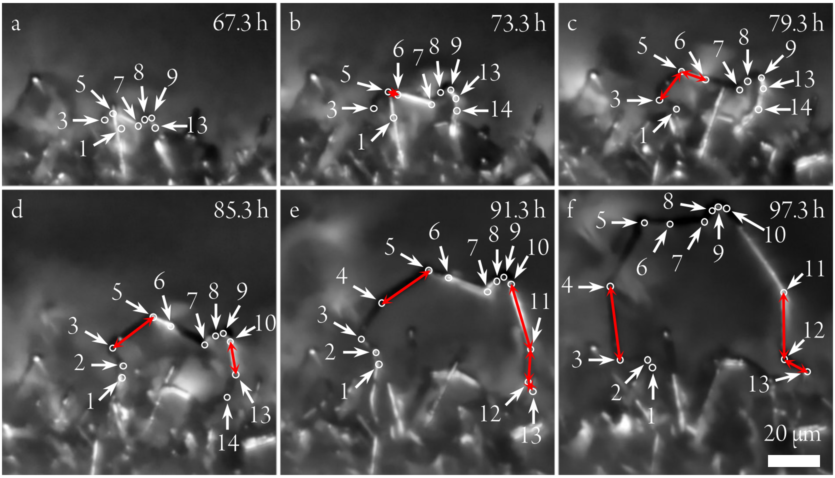

Figure 6.3: (a-f) Growth of the loop L1 at −0.05 mA cm^{-2} with 6 hours of deposition between the images. White circles indicate kinks of the loop. The number of kinks increases over time. Kink 14 is not visible in all of the images as other needles block the view. The larger markers in the L1-plot of Figure 6.1b indicate when the images (a-f) were taken. Reprinted from Becherer *et al.*[177]

---

[4] The videos and the explanatory note to video SV3 are available online in the electronic supplementary information of 10.1039/d1ta10920k[177]

(red plot) is shown in detail in Figure 6.3 and the supporting video SV2[4]. In Figure 6.3, all visible kinks are marked by white circles and numbered. From the images, it becomes clear that the segments grow at different speeds and individual segments dominate the growth. The segments that dominate (red arrows in Figure 6.3) can change over time. For a better visibility of the loop, the same image sequence without the markers is shown in Figure A.7 in Appendix A.7. The fastest growing segments are either next to newly formed kinks (kink 6 in b, kink 10 in d, and kink 4, 11, and 12 in e) or next to segments that grew fast beforehand (segment 3-5 in c and segment 3-4 in f). The segments between kink 7 and 9 hardly grow during the 30 h of deposition shown in Figure 6.3, while some segments reached growth velocities beyond 4 $\mu m\,h^{-1}$ (measured for 2 h intervals), which is significantly faster than the fastest velocities observed for individual needles (up to 3 $\mu m\,h^{-1}$). During deposition, the number of kinks increases. Freshly formed kinks appear either next to another kink (kink 2, 6, and 10) or between two kinks (kink 4, 11, and 12).

The crystal orientations of the segments of a loop that grew during the deposition shown in Figure 6.1, Figure 6.2, and Figure 6.3 were analyzed using electron backscatter diffraction (EBSD) in the SEM. Although the EBSD patterns are weak, as it is expected for lithium, they clearly show that the crystal orientation of each segment is constant but changes at kinks, i.e., GBs are present at the kinks. The supporting video SV3[4] (see also the explanatory note in the electronic supplementary information[4]) shows the EBSD patterns for various measurement points. As shown in Chapter 5 and reported previously[12], the lithium insertion occurs at the kinks and hence at GBs.

Figure 6.4 shows SEM images of kinked lithium structures after 100 h deposition at $-0.05\ mA\,cm^{-2}$. Figure 6.4a contains a small loop where both ends are connected to the surface. It shows an abrupt change in diameter on its right limb. The last segment of the loop in lower right corner of the image appears to be almost parallel to the substrate. The outline of this segment is highlighted by two red lines. Figure 6.4b shows a strongly kinked needle containing segments with different contrast and different diameter. Their surface structure and faceting seem to vary. A striking feature are the periodic fine rings perpendicular to the growth direction. Figure 6.4a and b show dark regions. The image of Figure 6.4c was taken at low accelerating voltage (higher surface sensitivity) and shows these dark regions more clearly. According to energy dispersive X-ray (EDX) analysis (see Figure 6.5),

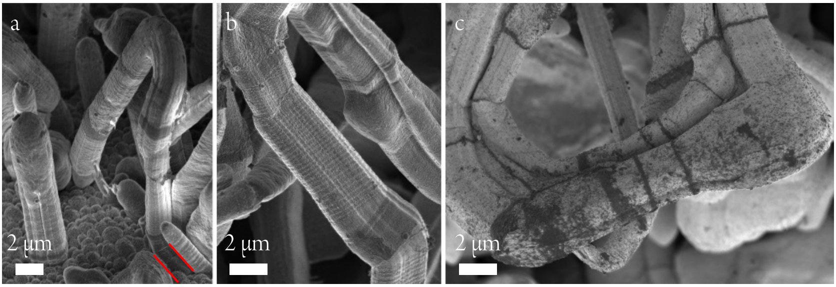

Figure 6.4: Lithium deposits formed at a current density of $-0.05\,\mathrm{mA\,cm^{-2}}$. (a) A small loop and its connection to the substrate. (b) Needles with multiple kinks and defects at the kinks. The different segments exhibit different surface structures. (c) Image of a loop recorded at low acceleration voltage (high surface sensitivity). The images were taken at acceleration voltages of (a) 1.5 kV, (b) 1 kV, and (c) 0.3 kV. Reprinted from Becherer *et al.*[177]

these dark regions contain more oxygen and more carbon than the surrounding surfaces.

Similar observations as descried for the deposition at $-0.05\,\mathrm{mA\,cm^{-2}}$ were made for a ten times higher deposition rate of $-0.5\,\mathrm{mA\,cm^{-2}}$. The results can be found in the Appendix A.8. The general growth behavior was the same. The following minor differences that were observed: (i) the individual needles grow significantly shorter; (ii) loops tend to kink more frequently, which results mostly in shorter segments (see supporting video SV4[4] and Figure A.8b-e); (iii) spherical bulges were regularly observed at kinks (inset Figure A.8e); (iv) an acceleration in the growth rate of the needles was not observed after nucleation; (v) the needles and loops grew significantly faster compared to Figure 6.1b, but slower than expected given the ten times higher rate.

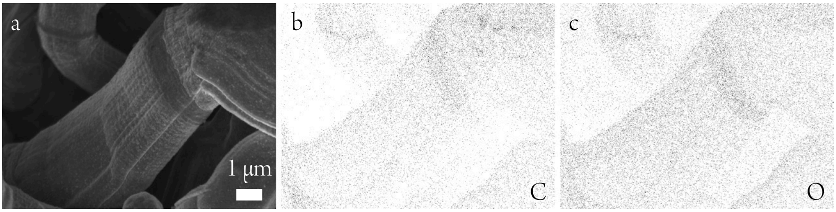

Figure 6.5: Investigation of the chemical composition by EDX. (a) SEM image, (b) map of the carbon distribution, and (c) map of the oxygen distribution. Reprinted from Becherer *et al.*[177]

6.2 Discussion

Experimental evidence at high resolution is hard to obtain for nanoscale lithium deposits in a liquid electrolyte. For example, photons and electrons show little sensitivity for the light element and interfere with the deposition process. In this work, optimized light microscopy at the physical resolution limit is used to observe relatively large areas. While the spatial resolution is limited, electrochemical processes are not distorted. The data clearly show a trend: loops and needles differ. Since it is impossible to measure the local mechanical stresses within tiny lithium structures during the electrodeposition and it is impossible to observe atoms diffusing on dendrites, the discussion has to be based on the indirect evidence as obtained from the measurements. The fundamental growth mechanism that is suggested can also explain observations found in the literature.

6.2.1 Transport Limitations do not Seem to Govern Growth

The growth of individual structures, needles and loops, during the electrodeposition of lithium was investigated by *operando* light microscopy. Root growth and growth at kinks were observed as shown in Chapter 5 and reported before.[11, 12] Growth by insertion into these locations is not in agreement with models based on the ionic mass transport limitations of the electrolyte that result in growth at the tips. Examples of for models based on transport limitations are those valid in diluted solutions at high rate[8] and in polymers electrolytes[10].

The observed growth kinetics does not correspond to the change in ionic concentration that is expected for a galvanostatic experiment. Based on light microscopy, Nishikawa et al.[171, 172] concluded that the ionic transport limits the growth because the length of the deposit scaled with the square-root of time ($\sqrt{t}$) as is characteristic for diffusion. However, other mechanisms like a random-walk movement of a tip of a kinking structure can result in a very similar time dependence.[49] For individual needles, we did not observe such a $\sqrt{t}$ dependence; the length vs. time curve of a needle often has an inflection point (i.e., a maximum growth rate). Given the kinked geometry of needles, loops, and bushes and the location of insertion sites, there seems to be no physical reason to assume that there is a diffusional transport limitation in the solution that causes a simple $\sqrt{t}$ law (a more detailed discussion can be found in the supplementary information of Becherer *et al.*[177]). SEI thicknesses are often assumed to grow with $\sqrt{t}$, but at the active insertion points the lithium surface is renewed continuously, so it is not expected that the SEI thickness grows with a $\sqrt{t}$ law. Therefore, the apparent $\sqrt{t}$ dependence might be rather a coincidence than a diffusion-related effect. In Chapter 5, it is shown that for all battery-relevant deposition rates, ionic transport limitations in the electrolyte anyway only play a minor role compared to the defect related insertion mechanism.

6.2.2 Microstructure, Self-Diffusion, and Deformation of the Lithium Deposits

Here, deformation-mechanism maps (Figure 2.4 in Section 2.4) are used to infer on important diffusion pathways within the lithium structures. These diffusion pathways are expected to be relevant not only for deformation but also for growth. Despite that kinked needles have been reported to be single-crystalline,[189, 190] GBs were observed at kinks in this work (video SV3[4] and explanatory note in the electronic supplementary information[4]). GBs consist of crystalline defects and contain vacancies. High-angle boundaries can be described by amorphous regions and low-angle boundaries are often treated as arrays of dislocations. For lithium, room temperature is approximately $0.65 \cdot T_\mathrm{m}$ (melting temperature in K). Typical deformation mechanism maps of alkali metals[161] (Figure 2.4 in Section 2.4) show that at such high homologous temperatures, deformation is not necessarily based on dislocation glide. Three diffusive processes are already active at lower stresses: These are (i) GB diffusion (in bulk materials known as Coble creep) and (ii) dislocation creep (climb). Since the deposits have very small dimensions (Figure 6.4) and hence exhibit high surface to volume ratios, (iii) surface diffusion may also contribute to the deformation and growth of segments. It may be expected that at room temperature diffusion along the surface is even faster than the already facile GB diffusion. A coupling of the transport paths is very likely. A similar coupling between surface and interface diffusion (interfacial Coble creep) has already been identified for a combination of lithium and a mixed ionic-electronic conductor.[191]

6.2.3 Diffusion Pathways and Their Coupling

From the literature, it is known that most metal atoms can diffuse from the surface into and out of GBs and thereby cause mechanical stresses.[192–194] This has been observed on metal thin films on rigid substrates. During physical vapor deposition of metallic thin films, adatoms migrate into the GBs and cause compressive stresses.[193–195] For thin films on substrates, compressive stress arises due to the mechanical constraints of the growing film that is rigidly attached to a substrate. This is different in the kinked needles where grains are arranged sequentially and can elongate by displacing their neighbors. The observed deposits contain GBs between their segments: EBSD shows that segments that are separated by kinks have different crystal orientations (supporting video SV3[4]). The observation of elongating segments (Figure 6.2 and Figure 6.3, cf. Steiger *et al.*[12]) suggests that growth takes place by lithium insertion into these GBs. During electrodeposition, lithium adatoms are deposited onto the substrate and onto the segments of the needles. On the surface of the segments, there are few defects (e.g., islands with ledges) and the probability for adsorption (i.e., crystal growth) is low. Therefore, adatoms remain mobile and can diffuse towards a GB (Figure 6.6). Inside the GB, atoms have a higher coordination (number of neighbors) than on the surface and adatom insertion into the GB is expected to be energetically favorable due to the higher number of bound electrons compared to an adatom at the surface. Since diffusion is facile there as well, the lithium atom can move along the GB. For example, such a coupled diffusion path of surface and GB diffusion has been identified as a stress relaxation mechanism for copper films at high temperature.[192]

6.2.4 Diffusion, Plasticity, and Insertion Defects – a Possible Growth Mechanism

The GB itself consists of crystalline defects, and plasticity, which causes additional crystalline defects, is introduced into the GBs and the segments by mechanical stresses. Typical defects are dislocations, which are line-like distortions of the crystalline lattice. Along the line of a dislocation, diffusion is enhanced (pipe diffusion) compared to the undistorted bulk. Atoms may move away from the GB into dislocations or vacancies (Figure 6.6) and thereby enter the bulk. Here again, the coordination of the lithium atom is higher and hence the insertion into a defect is energetically favorable. The atom insertion into crystalline defects contributes

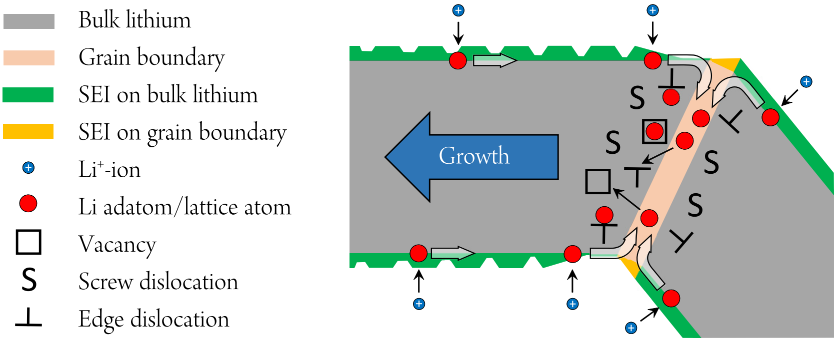

Figure 6.6: Schematic illustration of lithium insertion into a kinked deposit. Adatoms diffuse along the surface into GBs where they then move into crystalline defects and cause growth of the segment on the left side. Reprinted from Becherer *et al.*[177]

to the healing of the defects and causes a growth of a segment. Growth requires the diffusion of atoms to the insertion site, i.e., vacancy diffusion away from it. Vacancies always diffuse from tensile regions to compressive regions. From thin film growth it is known that the diffusion of adatoms into GBs generates extremely high compressive stresses[193, 196] and hence it is likely that the vacancies in the lithium structures diffuse to the GBs where compressive stresses or at least excess atoms are available. This corresponds to the motion of atoms away from the GB and into the crystallite, which may contribute to the growth of the segment. For example, for an edge dislocation in the proximity of a GB, this stress driven insertion could introduce negative climb. Here, an atom is added at the edge of the extra half-plane and the dislocation displaces. With this step, the crystalline lattice as a whole shifts/grows perpendicular to the extra half-plane by a fraction of a Burgers vector (cf. Appendix A.9). Repeated insertion of this type leads to crystal growth along the Burges vector. For a body-centered cubic (bcc) lattice, the Burgers vector lies along the $\langle 111 \rangle$ direction. This growth direction has been observed and reported as predominant in the literature.[160, 189, 190] Maybe instead of the minimization of the surface energy[189, 197], the insertion of atoms into defects determines the growth direction. For single-crystalline whiskers of lithium and tin, growth has been described by the climb of prismatic dislocation loops (Bardeen-Herring climb source).[190, 198] This mechanism is based on climbing dislocations as well and may also be relevant here. In general, defects act as sinks for lithium atoms and thereby continuously heal and reform during growth. Most likely, this healing during ongoing deposition is different from the well-known and more static healing/annealing of defects while no excess atoms are present.

It can be expected that due to geometrical reasons and the resulting stress distribution, the number of defects differs between neighboring segments. Growth may be faster in one of the two segments (e.g., the left segment in Figure 6.6). Instead of healing, dislocations (defects) can minimize the energy by building regular arrays, i.e., low-angle grain boundaries. In polycrystalline bulk materials, this is known as subgrain formation and happens during dynamic recrystallization. In loops, similar processes could lead to the formation of additional kinks. Several freshly formed kinks can be found in Figure 6.3 (e.g., kink 4 formed between Figure 6.3d and e).

The crystalline defects that act as insertion sites might facilitate unidirectional growth. The observations clearly show that segments elongate, but do not grow in their diameter. The high homologous temperature, which enables the facile diffusion of atoms on the faceted surfaces, results in a facetted shape of the segments that is determined by the minimization of surface energy (Wulff construction[199]). Steps and irregularities at the surfaces that can be created by dislocation activity (i.e., lateral growth) may decay. Their atoms may diffuse along the surface to the GB where they are reinserted. In addition, the influence of the mechanically stiff SEI might be of importance in the way that it mechanically restricts lateral growth.

6.2.5 Possible Influence of the SEI

Beside the crystalline effects favoring the insertion at the base and at kinks, the SEI will most likely play an important role. Since it is known that even the crystal orientation of lithium influences the SEI,[183] it is very likely that the SEI on a GB differs significantly from the SEI on bulk lithium. The different surfaces at kinks or in their vicinity, which were shown with surface sensitive SEM images at low acceleration voltages (Figure 6.4b and c) and the differences in the chemical composition (Figure 6.5) support the concept of an altered SEI at the insertion locations. The higher concentration of carbon and oxygen in Figure 6.5 may indicate a higher content of crystalline Li_2CO_3 grains within the SEI on the GBs. Li_2CO_3 was found in the SEI with a similar electrolyte by high-resolution TEM.[189] This most likely affects the transport of lithium ions through the SEI in these regions. Also important seems the fact that the SEI has to rupture frequently in locations where growth occurs and thus the transport to the insertion sites can occur without SEI or through a thin and defective SEI. For example, the periodic rings perpendicular to the growth direction shown in Figure 6.4b could be caused by repetitive changes (e.g., cracking) of the SEI during growth. Slower growth may not result in such patterns since the SEI has sufficient time to recover. The cracking and healing of the SEI during growth of lithium whiskers was observed by Yang et al.[190] in a TEM study where Li_2CO_3 was used as solid electrolyte. They conclude that cracking dominates at high rates, resulting in the axial growth of lithium whiskers, while self-healing of cracks resulted in the growth of spherical particles at lower rates. In this work, it was observed that bulges often form at kinks (inset Figure A.8e) when larger currents are applied. In this case, the transport inside the GB might not be fast enough to accommodate the flux of adatoms from the surface. Often bulges appear at the end of short segments (Figure A.8) in the proximity of other bulges. Therefore, either a short segment is a consequence of the limited transport through a bulge or the slow diffusion at a given location induces a bulge. The electrolyte and additives can strongly influence the SEI composition. Therefore, the transport through the SEI may differ significantly in different electrolytes. Chen *et al.*[70] proposed that the lithium ion depletion within an SEI with a low conductivity of lithium ions can result in dendritic growth, while an SEI with a high conductivity results in spherical deposits. Even when initially spherical lithium is deposited, a transition to the growth of kinked needles can be observed for longer deposition times.[166] After this transition, the mechanism proposed here may play an important role independent of the liquid electrolyte used.

6.2.6 Loop Formation

It was found that loops, which are structures connected to the electrode at both ends, grow significantly faster than individual needles. The formation of features that are connected to the electrode at both ends seems not straightforward. Unfortunately, the initial growth of loops could not be observed. Loops only became visible at later stages of the deposition when the electrode was already covered by lithium needles. Based on the SEM observation in Figure 6.4a, it is assumed that loops can form when needles grow almost parallel to the electrode surface and meet an obstacle, e.g., other needles. The tip of the needle and the obstacle can reduce their surface energy by coalescence. Given the high surface-to-volume ratio of these structures and the high homologous temperature, this type of diffusion bonding is plausible. Continued lithium insertion at the base of the needle may then result in a buckling of the structure and the loop becomes visible. The hypothesis of an obstacle-based loop formation is in agreement with the increasing number of loops that occur at later stages of the deposition when the electrode surface is covered by a sufficient number of potential obstacles.

6.2.7 Loops and Needles Exhibit Different Mechanical Boundary Conditions

The electrochemical conditions for loops are not significantly different from those of needles growing in their vicinity. Mechanically, they are very different: While loops are constrained by being connected to the substrate at both ends, needles can freely elongate and kink since they are connected to the substrate only at one point. These freestanding needles will not develop forces along their segments and consequently their crystalline defects may heal. In contrast, the growth of segments in loops that are attached at both ends inevitably induces tensile and compressive stresses, and depending on the angle at the kinks, different stress concentrations and stress gradients exist. Therefore, significant growth in loops causes plastic deformation, for example at kinks. Plastic deformation is based on dislocation motion. During deformation, dislocations interfere with each other and multiply. For example, mobile dislocations can interfere with the immobile dislocations of GBs and thereby continuously generate crystalline defects, which increase the number of insertion sites. Furthermore, mechanical stress is expected to induce defects in the SEI. Both of these effects together can explain the faster growth of a segment of a loop compared to that of an individual needle. Due to the constraints of a loop, the mechanical stresses of all of the kinks are interlinked and insertion into a given kink might also trigger mechanical effects and insertion at distant kinks. This could additionally fuel loop growth. The observations show that new dominating insertion sites occur in the proximity of rapidly growing segments. It is plausible that the stresses are highest close to the insertion points and that the number of kinks between two insertion sites mitigate the stress on kinks that are farther apart. There is no simple pathway of stress relief in growing loops: Growth induces mechanical stress and this stress enhances insertion. Therefore, the growth of loops may be self-sustaining during the electrodeposition.

The aforementioned arguments may also apply for bushes. In Chapter 5, a strongly accelerating growth of lithium bushes is shown, which grow from their inside, during the electrodeposition at higher rates. Growth in all directions can result in coalescence with other lithium deposits, creating bushes, which are 3D-interconnected structures. The geometrical constraints inside a strongly interlinked bush are even more severe than the constraints in a loop since the 3D confinement of a bush increases the stiffness in three dimensions and geometrical changes induce additional stresses. This means that insertion into kinks leads to a stronger activation of insertion sites. Since the lithium deposits located at the perimeter of the bush are less constrained, little stress is induced in their GBs and growth is slower. Therefore, the insertion into the GBs is only promoted in the inner part of the bush where the ligaments are strongly interlinked, resulting in the observed growth from the inside of the bushes. This effect of an enhanced insertion at deforming GBs appears to be significant since this growth mode is even dominant while the electrolyte ionically depletes (Chapter 5). Models only based on ionic mass transport limitations predict a growth at the tips of the bush. In the experiments in Chapter 5, a three-dimensional growth from the inside of the bush was observed.

6.2.8 Implications of the Discussed Growth Mechanism

Many publications have shown that large area substrates (e.g., porous metals or carbons) minimize dendritic growth.[200–202] A usual interpretation of this effect is the smaller current density at such substrates, which has been suggested to avoid electrolyte depletion. Since results in Chapter 5 indicate that depletion is not dominating the growth, an alternative explanation of the effect is suggested: The larger substrate area results in a large substrate-lithium interface, which might provide large number of insertion sites. Furthermore, similar to the preferred insertion inside a bush, the insertion within a porous and stiff substrate can create mechanical stresses due to the limited space of the pores and the collision of the growing structures with the pore walls. Therefore, lithium growth inside the porous structure can result in plasticity and an enhanced insertion of lithium, while this is not the case for structures growing at the surface of the porous host structure.

It has been reported by several groups that stack pressure can prevent dendrite formation in lithium metal cells with liquid[73, 148–150] or solid[203] electrolytes. In the context of this work this strategy might work best if compressive stresses (pressures) above the yield stress of bulk lithium (<1 MPa[162]) are maintained throughout a cycle, resulting in continuous plasticity of the electrode and a homogeneous generation of insertion sites. A size-dependent yield strength of lithium was observed for micro pillars[159] and for electrochemically grown lithium whiskers[160]. Therefore, small and hence strong features may develop that will not plastically deform due to the stack pressure. Without plasticity, they may not be able to sustain their insertion sites and hence cease growth. Plasticity in large flat regions or in larger features with low yield stress may still be maintained and these regions therefore may bypass the small and strong protrusions during growth. Therefore, stack pressure may prevent the growth of individual needles that could short circuit the cell and additionally facilitates a flat and homogenous deposition.

6.3 Conclusion

Operando light microscopy close to the physical resolution limit of visible light was used to investigate the growth of lithium during electrodeposition. Lithium is inserted into needles and loops at their base and at kinks. EBSD showed that kinks coincide with GBs between lithium segments. The statistically representative data shows that growth of a loop segment can be faster than that of a needle. Loops and needles exhibit similar shapes and hence the observed difference in growth velocity are attributed to different mechanical boundary conditions. While needles are freestanding, loops are held at both ends. Consequently, the growth of loops induces mechanical stresses. The observations suggest that electrodeposition of lithium couples to mechanical stress: Electrodeposition not only generates stresses but is also is affected by them. During electrodeposition, plastic deformation of the lithium may generate insertion sites for lithium that can control the growth of a structure. After the deposition of an adatom, surface diffusion and diffusion along GBs are important transport mechanisms: Coupled diffusion along the surface and in a GB moves lithium atoms inside the lithium structures where they are inserted into the crystal. Here the climb of dislocations and the occupation of vacancies act as sinks for atoms and mediate crystal growth. Maintained plasticity can continuously generate these defects and hence can drive the growth of segments. The Burgers vector in bcc lattices is the $\langle 111 \rangle$ direction. If climb of dislocations controls growth, the segments will be oriented along this direction.

Following these interpretations, two very different strategies may be used to prevent the non-uniform growth of lithium: (i) Shutting down GB diffusion, either by SEI components that block lithium from entering into the GB or by foreign atoms within the GB blocking lithium transport. (ii) Distribute the insertion sites uniformly and facilitate the growth of a large number of lithium grains. This might be accomplished by a uniform stack pressure causing homogeneous plastic deformation.

This chapter highlights the importance of crystalline defects and mechanical stresses for the growth of lithium. Since sodium and potassium also have low melting points, the suggested growth mechanism can be expected to be also relevant for their deposition.

7 Summary

The demand for high performance batteries is steadily rising. A promising approach to significantly increase the energy density (Wh/l) and specific energy (Wh/kg) is the replacement of the graphite anode in LIBs by a lithium metal anode. During the charging process of a lithium metal battery (LMB), lithium metal is electrodeposited. These deposits usually do not form flat films but so-called dendrite structures with large surface-to-volume ratios, resulting in poor cycling stability and potentially in safety hazards. The growth of lithium dendrites is described in the literature by several models. These models are often contradictory and, in many cases, they cannot explain the experimental observations. A growth mechanism that is based on the insertion at defects can describe the electrodeposits that are observed in many *operando* studies. However, the previous *operando* observations of the growth of lithium electrodeposits have been executed (i) at low spatial resolution, (ii) only at low deposition rates, or (iii) in environments far from practical applications. Therefore, it remained unclear how the deposition rate, which can vary in a wide range in battery applications, influences the growth mechanism. This thesis revisits the fundamental phenomenon of dendrite growth and investigates the growth at all rates that are relevant for practical battery applications at a high spatial resolution and inside a liquid electrolyte that is commercially used in batteries.

To elucidate the process of lithium deposition, an *operando* light microscope and a dedicated custom-built electrochemical cell with a window were used. The light microscope was optimized to acquire z-stacks at high speed and to calculate images with an extended depth of field, while maintaining the resolution close to the physical limit. With the acquired z-stacks, it is additionally possible to determine the dimensions of three-dimensional objects within the cell volume instead of only measuring their two-dimensional projections in conventional light microscopy. Furthermore, large areas could be observed to obtain statistically relevant data. Compared to previous studies, these experimental optimizations enabled the observation of large areas, which was even possible at high deposition rates and unprecedented spatial resolution.

The electrodeposition of lithium and sodium was compared in Chapter 4. For this comparison, the analogous electrolytes 1 M $LiPF_6$ in EC/DMC (LP30) and 1 M $NaPF_6$ in EC/DMC were used. While the electrodeposition of lithium results in the growth of somewhat stable lithium bushes, the sodium electrodeposits are extremely fragile and particles break off the growing sodium bush and fall apart. Although lithium and sodium are very similar, this example shows that equivalent cells of lithium and sodium can behave very differently. The use of sodium results in very poor deposition efficiency. 1 M $NaClO_4$ in PC showed a better stability and was used to study the electrodeposition of sodium in more detail. At a low deposition rate of $-20\ \mu A\ cm^{-2}$ a needle growth from the base was clearly observed. This has been predicted but has not been shown experimentally before.[182] The observed growth is very similar to the observations of lithium needles by Steiger *et al.*[12] and hence these observations indicate similarities in the growth of lithium and sodium electrodeposits.

In Chapter 5, all battery-relevant deposition rates were evaluated by applying current densities from $-50\ \mu A\ cm^{-2}$ to $-100\ mA\ cm^{-2}$, which correspond to C-rates that range from C/60 to 33 C for an area specific capacity of $3\ mAh\ cm^{-2}$, which is a realistic value for practical applications. The results show different growth regimes depending on the rate but the fundamental building blocks of the electrodeposits remain the same at all rates. With an increasing deposition rate and for longer deposition times, the electrodeposition localizes. Even these localized electrodeposits grow non-directionally from their inside and not at the tip as predicted by models based on transport limitations within the liquid electrolyte. At the highest rate of $-100\ mA\ cm^{-2}$, the electrolyte ionically depletes after some time, nevertheless the deposition continues by non-directional growth of bushes from their insides.

The growth of the individual structures, namely needles and loops, was evaluated in more detail in Chapter 6. Needle growth dominates the deposition in the beginning. These structures clearly grow from their base. Loops become visible at later stages of the growth and the segments elongate by growth between the kinks. Electron backscatter diffraction indicates that kinks coincide with GBs and that the segments are single crystalline. The segments of a loop grow at very different rates and the dominating segment(s) can change over time. In contrast to needles, the growth rate of loops does not decrease. Furthermore, the individual segments of a loop can grow significantly faster than needles.

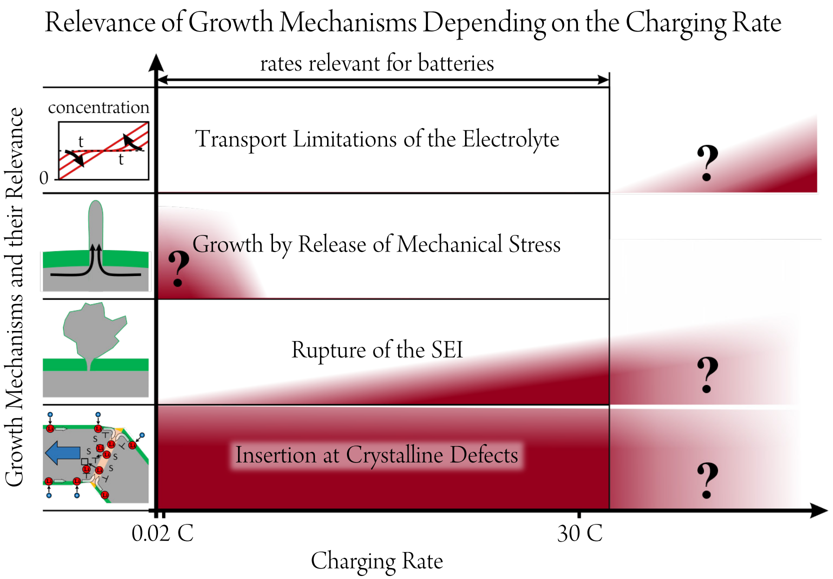

Figure 7.1: Qualitative chart comparing the relevance of growth mechanisms depending on the charging rate. Red areas mark regions where mechanisms could be active and white regions designate where a mechanism was not found to be active. The height of the red area in the vertical direction varies to denote a change in the significance of a mechanism. Areas with question marks were not addressed in this work or can neither be confirmed nor excluded by the observations made.

Figure 7.1 qualitatively compares the relevance of a selection of growth mechanisms for lithium electrodeposits found in the literature and a new growth mechanism that is suggested in this thesis. Red areas mark regions where mechanisms could be active and white regions designate where a mechanism was not found to be active. The height of the red area in the vertical direction varies to denote a change in the significance of a mechanism. Areas with question marks (unknowns) either were not addressed in this thesis or the relevance can neither be confirmed nor excluded. Transport limitations within the liquid electrolyte are probably the most common explanation for dendrite growth in literature. However, the observations in this work strongly indicate that they have no significant relevance for the electrodeposition at charging rates that are of relevance for battery applications in the liquid electrolytes, which are typically used in LIBs. Models based on transport limitations in the electrolyte predict a growth of the electrodeposits at their tip. This was not observed at any rate in this thesis. Even when the overpotential of the cell indicated ionic depletion of the electrolyte, the growth continued non-directional from the inside of the lithium bush. It is likely that transport limitations play a role when rates are applied, which are far outside of the range of typical battery charging rates or in cells with extreme cell geometries that are far from practical applications. This is indicated by the area with a question mark in the upper right of Figure 7.1. The whisker growth by the extrusion of lithium due to the release of mechanical stress can explain the growth of individual needles, which only occur at low deposition rates. Since this model cannot explain the growth of needles with kinks or loops that occur at the same rates, it is questionable if this additional mechanism is required for the growth of needles without kinks. Nevertheless, the mechanism cannot be fully excluded by the observations of this thesis and hence the corresponding region for low deposition rates, in which needles without kink occur, contains a question mark in Figure 7.1. The stability of the SEI is often considered to be an important factor for the growth of dendrites. Although this thesis does not indicate that the SEI directly controls the growth mechanism of lithium electrodeposits, it strongly suggests an influence of the SEI. In many cases, the electrodeposition localized with the occurrence of fast-growing and porous bushes. The initiation of these bushes is attributed to a rupture of the SEI, and the probability of their occurrence increased with the deposition rate. Figure 7.1 shows the growing relevance of the rupture of the SEI with an increase of the charging rate.

Based on the observations made in this work, a new growth mechanism is suggested: As room temperature corresponds to about two-thirds of the melting point of lithium, diffusive processes can be expected to be facile. After the reduction, adatoms are transported to the insertion sites by surface diffusion and subsequent diffusion along the GBs. At the GB, vacancies and dislocations act as sinks for the lithium atoms a that leads to insertion of atoms into segments and to their growth. Plasticity is mediated by dislocations and therefore the presence of plasticity may affect the availability of insertion sites. As Figure 7.1 shows, this proposed mechanism seems to be the only mechanism that is of high relevance at all relevant rates. While needles are only fixed at the electrode at one point and can freely elongate, the growth of a segment in a loop inevitably induces tensile and compressive stresses and hence plasticity. This leads to an increased number of insertion sites so that loops can grow faster and growth of these structures can become self-sustaining during the electrodeposition. While loops are mechanically more constrained than needles, the 3D structure in the inside of an interlinked bush is even stiffer and the growth of a segment inside a bush should cause even more plastic deformation than in a loop. This is in line with the observation that bushes grow from their inside. Since other alkali metals also have low melting points, the suggested growth model may be applicable to them as well. This is in accordance with the observations in Section 4.3, where the growth of a sodium needle is very similar to that of lithium needles.

Based on the growth mechanism developed in this thesis, different approaches that may result in a homogeneous electrodeposition can be deduced. There are two fundamental strategies based on this growth mechanism to achieve a homogeneous electrodeposition: The transport to the insertion sites, i.e., the crystalline defects, has to be inhibited and/or the crystalline defects have to be distributed homogenously on the electrode surface. Figure 7.2a shows the growth mechanism schematically as introduced in Section 6.2.4, and Figure 7.2b

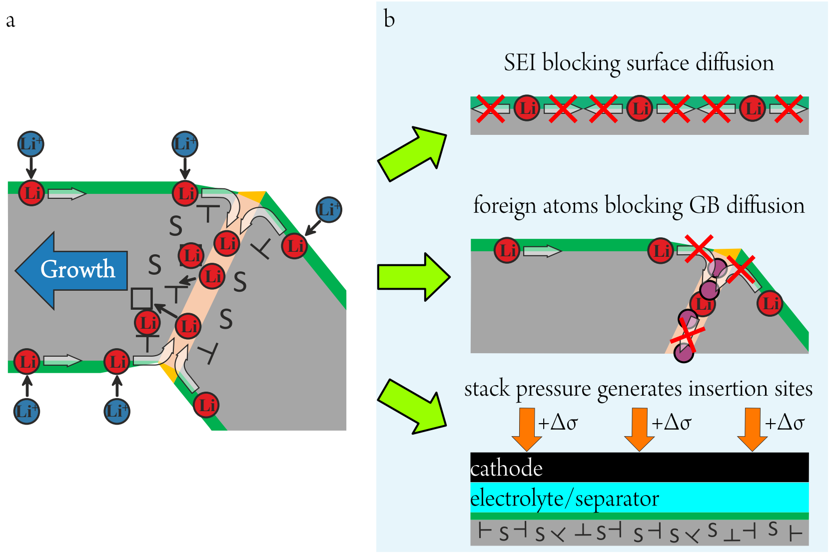

Figure 7.2: (a) Schematic illustration of lithium insertion into a kinked deposit (modified from Becherer *et al.*[177]). (b) Three methods based on the new growth mechanism that may result in a homogeneous electrodeposition in lithium metal batteries.

introduces three possible methods to achieve a homogeneous electrodeposition. The first two methods follow the strategy to inhibit the transport to the insertion sites, while the last method aims at generating homogeneously distributed insertion sites. In the first approach shown in Figure 7.2b an optimized SEI blocks surface diffusion of lithium metal and inhibits the transport to the insertion sites. This could be achieved by modifying the SEI with an additive or a preformed artificial SEI. If the surface diffusion is blocked, growth occurs were the lithium is reduced and hence a homogeneous transport through the liquid electrolyte and the SEI would result in a homogenous growth of the electrodeposits. The use of additives and preformed artificial SEIs to improve the electrodeposition in LMBs are well established in the literature. Various explanations exist but the SEI is rarely considered to block metal diffusion. The second approach shown in Figure 7.2b aims to block the transport to the insertion sites by suppressing the transport into and within the GBs, which could be achieved by foreign atoms (alloying). Small amounts of the alloying element could either be added directly to the metal electrode or by an additive within the liquid electrolyte. The last approach suggested in Figure 7.2b is to apply external pressure to the battery stack to generate plasticity in the whole lithium electrode. Consequently, crystalline defects and hence insertion sites are always present in the proximity of a reduced lithium atom and should result in a homogeneous growth. The positive influence of stack pressure on the electrodeposition in LMBs has been frequently reported. The improvements have been typically attributed to a better contact of lithium structures to each other and to the current collector or to the deformation of lithium protrusions, which results in a flat film. The growth mechanism proposed in this thesis gives a new perspective to the influence of stack pressure on the electrodeposition of lithium. Hopefully this improved understanding will help in the development of countermeasures against dendrites.

For the first time, high-resolution *operando* light microscopy was combined with the electrodeposition of lithium at deposition rates varied by more than three orders of magnitude. These experiments were used to elucidate the mechanisms controlling the electrodeposition at all rates that are relevant for batteries. The results highlight the importance of crystalline defects for the electrodeposition at all rates and the coupling of the electrodeposition and mechanical stresses. The new proposed growth mechanism can guide new strategies to achieve a homogeneous electrodeposition and may result in pathways to the commercialization of LMBs.

Bibliography

[1] K. Ozawa, "Lithium-ion rechargeable batteries with LiCoO2 and carbon electrodes: the LiCoO2/C system," in *Solid State Ionics*, vol. 69, no. 3–4, pp. 212–221, 1994.

[2] B. Dunn, H. Kamath, J.M. Tarascon, "Electrical energy storage for the grid: A battery of choices," in *Science*, vol. 334, no. 6058, pp. 928–935, 2011.

[3] V. Etacheri, R. Marom, R. Elazari, G. Salitra, D. Aurbach, "Challenges in the development of advanced Li-ion batteries: A review," in *Energy Environ. Sci.*, vol. 4, no. 9, pp. 3243–3262, 2011.

[4] M. Lécuyer, J. Gaubicher, A.-L. Barrès, F. Dolhem, M. Deschamps, D. Guyomard, P. Poizot, "A rechargeable lithium/quinone battery using a commercial polymer electrolyte," in *Electrochem. commun.*, vol. 55, pp. 22–25, 2015.

[5] D. Aurbach, E. Zinigrad, Y. Cohen, H. Teller, "A short review of failure mechanisms of lithium metal and lithiated graphite anodes in liquid electrolyte solutions," in *Solid State Ionics*, vol. 148, no. 3–4, pp. 405–416, 2002.

[6] W. Xu, J. Wang, F. Ding, X. Chen, E. Nasybulin, Y. Zhang, J.G. Zhang, "Lithium metal anodes for rechargeable batteries," in *Energy Environ. Sci.*, vol. 7, no. 2, pp. 513–537, 2014.

[7] X.B. Cheng, R. Zhang, C.Z. Zhao, Q. Zhang, "Toward Safe Lithium Metal Anode in Rechargeable Batteries: A Review," in *Chem. Rev.*, vol. 117, no. 15, pp. 10403–10473, 2017.

[8] J.N. Chazalviel, "Electrochemical aspects of the generation of ramified metallic electrodeposits," in *Phys. Rev. A*, vol. 42, no. 12, pp. 7355–7367, 1990.

[9] Y.S. Cohen, Y. Cohen, D. Aurbach, "Micromorphological studies of lithium electrodes in alkyl carbonate solutions using in situ atomic force microscopy," in *J. Phys. Chem. B*, vol. 104, no. 51, pp. 12282–12291, 2000.

[10] C. Monroe, J. Newman, "Dendrite Growth in Lithium/Polymer Systems - A propagation model for liquid electrolytes under galvanostatic conditions," in *J. Electrochem. Soc.*, vol. 150, no. 10, pp. A1377–A1384, 2003.

[11] J.I. Yamaki, S.I. Tobishima, K. Hayashi, K. Saito, Y. Nemoto, M. Arakawa, "A consideration of the morphology of electrochemically deposited lithium in an organic electrolyte," in *J. Power Sources*, vol. 74, no. 2, pp. 219–227, 1998.

[12] J. Steiger, D. Kramer, R. Mönig, "Mechanisms of dendritic growth investigated by in situ light microscopy during electrodeposition and dissolution of lithium," in *J. Power Sources*, vol. 261, pp. 112–119, 2014.

[13] D. Larcher, J.M. Tarascon, "Towards greener and more sustainable batteries for electrical energy storage," in *Nat. Chem.*, vol. 7, no. 1, pp. 19–29, 2015.

[14] S. Wei, S. Choudhury, J. Xu, P. Nath, Z. Tu, L.A. Archer, "Highly Stable Sodium Batteries Enabled by Functional Ionic Polymer Membranes," in *Adv. Mater.*, vol. 29, no. 12, p. 1605512, 2017.

[15] A.A. Yaroshevsky, "Abundances of chemical elements in the Earth's crust," in *Geochemistry Int.*, vol. 44, no. 1, pp. 48–55, 2006.

[16] Z.W. Seh, J. Sun, Y. Sun, Y. Cui, "A highly reversible room-temperature sodium metal anode," in *ACS Cent. Sci.*, vol. 1, no. 8, pp. 449–455, 2015.

[17] P. Schüdel, "Sodium Metal Anodes for Energy Storage," doctoral dissertation, Karlsruhe Institute of Technology, 2017.

[18] R. Cao, K. Mishra, X. Li, J. Qian, M.H. Engelhard, M.E. Bowden, K.S. Han, K.T. Mueller, W.A. Henderson, J.G. Zhang, "Enabling room temperature sodium metal batteries," in *Nano Energy*, vol. 30, pp. 825–830, 2016.

[19] R. Rodriguez, K.E. Loeffler, S.S. Nathan, J.K. Sheavly, A. Dolocan, A. Heller, C.B. Mullins, "In Situ Optical Imaging of Sodium Electrodeposition: Effects of Fluoroethylene Carbonate," in *ACS Energy Lett.*, vol. 2, no. 9, pp. 2051–2057, 2017.

[20] Y. Yui, M. Hayashi, J. Nakamura, "In situ Microscopic Observation of Sodium Deposition/Dissolution on Sodium Electrode," in *Sci. Rep.*, vol. 6, p. 22406,

2016.

[21] B. Ma, Y. Lee, P. Bai, “Dynamic Interfacial Stability Confirmed by Microscopic Optical Operando Experiments Enables High-Retention-Rate Anode-Free Na Metal Full Cells,” in *Adv. Sci.*, vol. 8, no. 12, p. 2005006, 2021.

[22] Y. Deng, J. Zheng, A. Warren, J. Yin, S. Choudhury, P. Biswal, D. Zhang, L.A. Archer, “On the Reversibility and Fragility of Sodium Metal Electrodes,” in *Adv. Energy Mater.*, vol. 9, no. 39, p. 2019, 2019.

[23] Y.S. Hong, N. Li, H. Chen, P. Wang, W.L. Song, D. Fang, “In operando observation of chemical and mechanical stability of Li and Na dendrites under quasi-zero electrochemical field,” in *Energy Storage Mater.*, vol. 11, pp. 118–126, 2018.

[24] “Analytical chemistry division commission on electroanalytical chemistry recommendations for sign conventions and plotting of electrochemical data,” in *Pure Appl. Chem.*, vol. 45, no. 2, pp. 131–134, 1976.

[25] Z. Liu, Y. Jiang, Q. Hu, S. Guo, L. Yu, Q. Li, Q. Liu, X. Hu, “Safer Lithium-Ion Batteries from the Separator Aspect: Development and Future Perspectives,” in *Energy Environ. Mater.*, vol. 4, no. 3, pp. 336–362, 2021.

[26] B. Scrosati, J. Garche, “Lithium batteries: Status, prospects and future,” in *J. Power Sources*, vol. 195, no. 9, pp. 2419–2430, 2010.

[27] P. Verma, P. Maire, P. Novák, “A review of the features and analyses of the solid electrolyte interphase in Li-ion batteries,” in *Electrochim. Acta*, vol. 55, no. 22, pp. 6322–6341, 2010.

[28] E. Peled, D. Golodnitsky, J. Penciner, “The Anode/Electrolyte Interface,” in *Handbook of Battery Materials*, 2nd ed., C. Daniel and J.O. Besenhard, Eds., Weinheim, Germany: Wiley-VCH Verlag & Co. KGaA, 2011, pp. 479–523.

[29] M. Schmitt, P. Scharfer, W. Schabel, “Slot die coating of lithium-ion battery electrodes: Investigations on edge effect issues for stripe and pattern coatings,” in *J. Coatings Technol. Res.*, vol. 11, no. 1, pp. 57–63, 2014.

[30] S.J. An, J. Li, C. Daniel, D. Mohanty, S. Nagpure, D.L. Wood, “The state of

understanding of the lithium-ion-battery graphite solid electrolyte interphase (SEI) and its relationship to formation cycling," in *Carbon*, vol. 105, pp. 52–76, 2016.

[31] M. Armand, P. Axmann, D. Bresser, M. Copley, K. Edström, C. Ekberg, D. Guyomard, B. Lestriez, P. Novák, M. Petranikova, *et al.*, "Lithium-ion batteries – Current state of the art and anticipated developments," in *J. Power Sources*, vol. 479, p. 228708, 2020.

[32] J. Sturm, A. Rheinfeld, I. Zilberman, F.B. Spingler, S. Kosch, F. Frie, A. Jossen, "Modeling and simulation of inhomogeneities in a 18650 nickel-rich, silicon-graphite lithium-ion cell during fast charging," in *J. Power Sources*, vol. 412, pp. 204–223, 2019.

[33] L.K. Willenberg, P. Dechent, G. Fuchs, D.U. Sauer, E. Figgemeier, "High-precision monitoring of volume change of commercial lithium-ion batteries by using strain gauges," in *Sustain.*, vol. 12, no. 2, p. 557, 2020.

[34] M.J. Lain, J. Brandon, E. Kendrick, "Design strategies for high power vs. High energy lithium ion cells," in *Batteries*, vol. 5, no. 4, p. 64, 2019.

[35] C. Pillot, "The rechargeable battery market and main trends 2018-2030," Stockage Batterie, Paris, France, May 28, 2019, https://www.bpifrance.fr/content/download/76854/831358/file/02 - Presentation Avicenne - Christophe Pillot - 28 Mai 2019.pdf (accessed Dec. 13, 2021).

[36] Y. Ding, Z.P. Cano, A. Yu, J. Lu, Z. Chen, "Automotive Li-Ion Batteries: Current Status and Future Perspectives," in *Electrochem. Energy Rev.*, vol. 2, no. 1, pp. 1–28, 2019.

[37] X. Zeng, M. Li, D. Abd El-Hady, W. Alshitari, A.S. Al-Bogami, J. Lu, K. Amine, "Commercialization of Lithium Battery Technologies for Electric Vehicles," in *Adv. Energy Mater.*, vol. 9, no. 27, p. 1900161, 2019.

[38] S. Sripad, A. Bills, V. Viswanathan, "The Iron Age of Automotive Batteries: Techno-economic assessment of batteries with lithium metal anodes paired with iron phosphate cathodes," in *ECSarXiv*, 2021, DOI: 10.1149/osf.io/fx4p9.

[39] Tesla, Inc., “Shareholder Deck - Q3 (Presentation),” Austin, Tx, USA, Oct. 20, 2021, https://tesla-cdn.thron.com/static/TWPKBV_TSLA_Q3_2021_Quarterly_Update_SI1AKE.pdf?xseo=&response-content-disposition=inline%3Bfilename%3D%22TSLA-Q3-2021-Quarterly-Update.pdf%22 (accessed Dec. 14, 2021).

[40] Ford Motor Co., “Capital Markets Day (Transcript),” Dearborn, Mi, USA, May 26, 2021, https://s23.q4cdn.com/799033206/files/doc_downloads/2021/09/Ford-Delivering-Ford-Transcript-Corrected-May-26-2021.pdf (accessed Dec. 14, 2021).

[41] M.N. Obrovac, V.L. Chevrier, “Alloy negative electrodes for Li-ion batteries,” in *Chem. Rev.*, vol. 114, no. 23, p. 11444–11502, 2014.

[42] A. Jain, S.P. Ong, G. Hautier, W. Chen, W.D. Richards, S. Dacek, S. Cholia, D. Gunter, D. Skinner, G. Ceder, *et al.*, “The Materials Project: A materials genome approach to accelerating materials innovation,” in *APL Mater.*, vol. 1, no. 1, p. 11002, 2013.

[43] H. Zhang, Y. Yang, H. Xu, L. Wang, X. Lu, X. He, “Li4Ti5O12 spinel anode: Fundamentals and advances in rechargeable batteries,” in *InfoMat*, vol. 4, no. 4, p. e12228, 2021.

[44] M.N. Obrovac, L. Christensen, D.B. Le, J.R. Dahn, “Alloy Design for Lithium-Ion Battery Anodes,” in *J. Electrochem. Soc.*, vol. 154, no. 9, pp. A849–A855, 2007.

[45] S.T. Boles, M.H. Tahmasebi, “Are Foils the Future of Anodes?,” in *Joule*, vol. 4, no. 7, pp. 1337–1349, 2020.

[46] W.J. Zhang, “A review of the electrochemical performance of alloy anodes for lithium-ion batteries,” in *J. Power Sources*, vol. 196, no. 1, pp. 13–24, 2011.

[47] T. Zheng, D. Kramer, R. Mönig, S.T. Boles, “Aluminum Foil Anodes for Li-ion Rechargeable Batteries: The Role of Li Solubility within β-LiAl,” in *ACS Sustain. Chem. Eng.*, vol. 10, no. 10, pp. 3203–3210, 2022.

[48] J.-G. Zhang, W. Xu, W.A. Henderson, *Lithium Metal Anodes and Rechargeable Lithium Metal Batteries*, 1st ed., ser. Springer Series in Materials Science, vol. 249,

Cham, Switzerland: Springer International Publishing, 2017.

[49] J. Steiger, D. Kramer, R. Mönig, "Microscopic observations of the formation, growth and shrinkage of lithium moss during electrodeposition and dissolution," in *Electrochim. Acta*, vol. 136, pp. 529–536, 2014.

[50] J.-I. Yamaki, S.-I. Tobishima, "Rechargeable Lithium Anodes," in *Handbook of Battery Materials*, 2nd ed., C. Daniel and J.O. Besenhard, Eds., Weinheim, Germany: John Wiley & Sons, Ltd, 2011, pp. 377–404.

[51] I. Yoshimatsu, T. Hirai, J. Yamaki, "Lithium Electrode Morphology during Cycling in Lithium Cells," in *J. Electrochem. Soc.*, vol. 135, no. 10, pp. 2422–2477, 1988.

[52] Z. Li, J. Huang, B. Yann Liaw, V. Metzler, J. Zhang, "A review of lithium deposition in lithium-ion and lithium metal secondary batteries," in *J. Power Sources*, vol. 254, pp. 168–182, 2014.

[53] A.W. Golubkov, D. Fuchs, J. Wagner, H. Wiltsche, C. Stangl, G. Fauler, G. Voitic, A. Thaler, V. Hacker, "Thermal-runaway experiments on consumer Li-ion batteries with metal-oxide and olivin-type cathodes," in *RSC Adv.*, vol. 4, no. 7, pp. 3633–3642, 2014.

[54] J. Landesfeind, J. Hattendorff, A. Ehrl, W.A. Wall, H.A. Gasteiger, "Tortuosity Determination of Battery Electrodes and Separators by Impedance Spectroscopy," in *J. Electrochem. Soc.*, vol. 163, no. 7, pp. A1373–A1387, 2016.

[55] "Datasheet PVDF," 2022, https://www.shop.amsler-frey.ch/en?cmd=generate_datasheet&lang=en&category=55 (accessed Aug. 08, 2021).

[56] "Datasheet Super P," 2021, https://www.imerys.com/public/2022-02/ENSACO-150-210-240-250-260-350-360G-ENSACO-150-250P-SUPERP-SUPERPLi-C-NERGY-SUPERC45-65T-C-NERGY252_276_GB_EN_V_9_0_SDB.pdf (accessed Aug. 08, 2022).

[57] Tesla Inc., "2020 Annual Meeting of Stockholders and Battery Day (Presentation)," Austin, Tx, USA, Sep. 22, 2020, https://tesla-share.thron.com/content/?id=96ea71cf-8fda-4648-a62c-753af436c3b6&pkey=S1dbei4 (accessed Dec. 21, 2021).

[58] K. Tsuruta, M.E. Dermer, R. Dhiman, "A cell with a tabless electrode," 2020, US Patent: US20200144676A1, Tesla Inc., available via: https://patents.google.com/patent/US20200144676A1/en (accessed Jun. 02, 2022).

[59] C. Brissot, M. Rosso, J.N. Chazalviel, P. Baudry, S. Lascaud, "In situ study of dendritic growth in lithium/PEO-salt/lithium cells," in *Electrochim. Acta*, vol. 43, no. 10–11, pp. 1569–1574, 1998.

[60] M. Rosso, T. Gobron, C. Brissot, J.N. Chazalviel, S. Lascaud, "Onset of dendritic growth in lithium/polymer cells," in *J. Power Sources*, vol. 97–98, pp. 804–806, 2001.

[61] H.J.S. Sand, "III. On the concentration at the electrodes in a solution, with special reference to the liberation of hydrogen by electrolysis of a mixture of copper sulphate and sulphuric acid," in *London, Edinburgh, Dublin Philos. Mag. J. Sci.*, vol. 6, no. 1, pp. 45–79, 1901.

[62] C. Brissot, M. Rosso, J.N. Chazalviel, S. Lascaud, "Dendritic growth mechanisms in lithium/polymer cells," in *J. Power Sources*, vol. 81–82, pp. 925–929, 1999.

[63] P. Bai, J. Li, F.R. Brushett, M.Z. Bazant, "Transition of lithium growth mechanisms in liquid electrolytes," in *Energy Environ. Sci.*, vol. 9, no. 10, pp. 3221–3229, 2016.

[64] A.R. Despic, K.I. Popov, "Transport-Controlled Deposition and Dissolution of Metals," in *Modern Aspects of Electrochemistry*, 1st ed., B.E. Conway and J.O. Bockris, Eds., Boston, MA: Springer US, 1972, pp. 199–313.

[65] J.L. Barton, J.O. Bockris, "The electrolytic growth of dendrites from ionic solutions," in *Proc. R. Soc. A Math. Phys. Eng. Sci.*, vol. 268, no. 1335, pp. 485–505, 1962.

[66] R. Akolkar, "Mathematical model of the dendritic growth during lithium electrodeposition," in *J. Power Sources*, vol. 232, pp. 23–28, 2013.

[67] K.N. Wood, E. Kazyak, A.F. Chadwick, K.H. Chen, J.G. Zhang, K. Thornton, N.P. Dasgupta, "Dendrites and pits: Untangling the complex behavior of lithium metal anodes through operando video microscopy," in *ACS Cent. Sci.*, vol. 2, no. 11, pp. 790–801, 2016.

[68] A. Maraschky, R. Akolkar, "Mechanism Explaining the Onset Time of Dendritic Lithium Electrodeposition via Considerations of the Li+ Transport within the Solid Electrolyte Interphase," in *J. Electrochem. Soc.*, vol. 165, no. 14, pp. D696–D703, 2018.

[69] R.N. Wasalathanthri, R. Akolkar, "Perspective—Does the Sand Equation Reliably Predict the Onset of Morphological Evolution in Lithium Electrodeposition?," in *J. Electrochem. Soc.*, vol. 169, no. 9, p. 092519, 2022.

[70] X.R. Chen, Y.X. Yao, C. Yan, R. Zhang, X.B. Cheng, Q. Zhang, "A Diffusion--Reaction Competition Mechanism to Tailor Lithium Deposition for Lithium-Metal Batteries," in *Angew. Chemie - Int. Ed.*, vol. 59, no. 20, pp. 7743 –7747, 2020.

[71] A. Kushima, K.P. So, C. Su, P. Bai, N. Kuriyama, T. Maebashi, Y. Fujiwara, M.Z. Bazant, J. Li, "Liquid cell transmission electron microscopy observation of lithium metal growth and dissolution: Root growth, dead lithium and lithium flotsams," in *Nano Energy*, vol. 32, pp. 271–279, 2017.

[72] J. Steiger, G. Richter, M. Wenk, D. Kramer, R. Mönig, "Comparison of the growth of lithium filaments and dendrites under different conditions," in *Electrochem. commun.*, vol. 50, pp. 11–14, 2015.

[73] L. Gireaud, S. Grugeon, S. Laruelle, B. Yrieix, J.M. Tarascon, "Lithium metal stripping/plating mechanisms studies: A metallurgical approach," in *Electrochem. commun.*, vol. 8, no. 10, pp. 1639–1649, 2006.

[74] A.A. Rulev, Y.O. Kondratyeva, L. V. Yashina, D.M. Itkis, "Lithium Planar Deposition vs Whisker Growth: Crucial Role of Surface Diffusion," in *J. Phys. Chem. Lett.*, vol. 11, no. 24, pp. 10511–10518, 2020.

[75] H. Kuwata, H. Sonoki, M. Matsui, Y. Matsuda, N. Imanishi, "Surface Layer and Morphology of Lithium Metal Electrodes," in *Electrochemistry*, vol. 84, no. 11, pp. 854–860, 2016.

[76] X.Q. Zhang, X.B. Cheng, X. Chen, C. Yan, Q. Zhang, "Fluoroethylene Carbonate Additives to Render Uniform Li Deposits in Lithium Metal Batteries," in *Adv. Funct. Mater.*, vol. 27, no. 10, p. 1605989, 2017.

[77] H. Ota, K. Shima, M. Ue, J. ichi Yamaki, "Effect of vinylene carbonate as additive to electrolyte for lithium metal anode," in *Electrochim. Acta*, vol. 49, no. 4, pp. 565–572, 2004.

[78] Q. Shi, Y. Zhong, M. Wu, H. Wang, H. Wang, "High-capacity rechargeable batteries based on deeply cyclable lithium metal anodes," in *Proc. Natl. Acad. Sci. U. S. A.*, vol. 115, no. 22, pp. 5676–5680, 2018.

[79] C. Yan, Y.-X. Yao, X. Chen, X.-B. Cheng, X.-Q. Zhang, J.-Q. Huang, Q. Zhang, "Lithium Nitrate Solvation Chemistry in Carbonate Electrolyte Sustains High-Voltage Lithium Metal Batteries," in *Angew. Chemie*, vol. 130, no. 43, pp. 14251–14255, 2018.

[80] J. Fu, X. Ji, J. Chen, L. Chen, X. Fan, D. Mu, C. Wang, "Lithium Nitrate Regulated Sulfone Electrolytes for Lithium Metal Batteries," in *Angew. Chemie*, vol. 132, no. 49, pp. 22378–22385, 2020.

[81] W. Li, H. Yao, K. Yan, G. Zheng, Z. Liang, Y.M. Chiang, Y. Cui, "The synergetic effect of lithium polysulfide and lithium nitrate to prevent lithium dendrite growth," in *Nat. Commun.*, vol. 6, p. 7436, 2015.

[82] F.A. Soto, Y. Ma, J.M. Martinez De La Hoz, J.M. Seminario, P.B. Balbuena, "Formation and Growth Mechanisms of Solid-Electrolyte Interphase Layers in Rechargeable Batteries," in *Chem. Mater.*, vol. 27, no. 23, pp. 7990–8000, 2015.

[83] A.L. Michan, B.S. Parimalam, M. Leskes, R.N. Kerber, T. Yoon, C.P. Grey, B.L. Lucht, "Fluoroethylene carbonate and vinylene carbonate reduction: Understanding lithium-ion battery electrolyte additives and solid electrolyte interphase formation," in *Chem. Mater.*, vol. 28, no. 22, pp. 8149–8159, 2016.

[84] U. V. Alpen, A. Rabenau, G.H. Talat, "Ionic conductivity in Li3N single crystals," in *Appl. Phys. Lett.*, vol. 30, no. 12, pp. 621–623, 1977.

[85] T. Lapp, S. Skaarup, A. Hooper, "Ionic conductivity of pure and doped Li3N," in *Solid State Ionics*, vol. 11, no. 2, pp. 97–103, 1983.

[86] Y. Zhu, X. He, Y. Mo, "Strategies Based on Nitride Materials Chemistry to Stabilize Li Metal Anode," in *Adv. Sci.*, vol. 4, no. 8, p. 1600517, 2017.

[87] F. Ding, W. Xu, G.L. Graff, J. Zhang, M.L. Sushko, X. Chen, Y. Shao, M.H. Engelhard, Z. Nie, J. Xiao, *et al.*, "Dendrite-free lithium deposition via self-healing electrostatic shield mechanism," in *J. Am. Chem. Soc.*, vol. 135, no. 11, pp. 4450–4456, 2013.

[88] Y. Zhang, J. Qian, W. Xu, S.M. Russell, X. Chen, E. Nasybulin, P. Bhattacharya, M.H. Engelhard, D. Mei, R. Cao, *et al.*, "Dendrite-free lithium deposition with self-aligned nanorod structure," in *Nano Lett.*, vol. 14, no. 12, pp. 6889–6896, 2014.

[89] A.A. Rulev, A. V. Sergeev, L. V. Yashina, T. Jacob, D.M. Itkis, "Electromigration in Lithium Whisker Formation Plays Insignificant Role during Electroplating," in *ChemElectroChem*, vol. 6, no. 5, pp. 1324–1328, 2019.

[90] M. Ue, K. Uosaki, "Recent progress in liquid electrolytes for lithium metal batteries," in *Curr. Opin. Electrochem.*, vol. 17, pp. 106–113, 2019.

[91] H. Yang, J. Li, Z. Sun, R. Fang, D.W. Wang, K. He, H.M. Cheng, F. Li, "Reliable liquid electrolytes for lithium metal batteries," in *Energy Storage Mater.*, vol. 30, pp. 113–129, 2020.

[92] G.G. Eshetu, T. Diemant, S. Grugeon, R.J. Behm, S. Laruelle, M. Armand, S. Passerini, "In-Depth Interfacial Chemistry and Reactivity Focused Investigation of Lithium-Imide- and Lithium-Imidazole-Based Electrolytes," in *ACS Appl. Mater. Interfaces*, vol. 8, no. 25, pp. 16087–16100, 2016.

[93] R. Miao, J. Yang, Z. Xu, J. Wang, Y. Nuli, L. Sun, "A new ether-based electrolyte for dendrite-free lithium-metal based rechargeable batteries," in *Sci. Rep.*, vol. 6, p. 21771, 2016.

[94] Y. Yamada, A. Yamada, "Review—Superconcentrated Electrolytes for Lithium Batteries," in *J. Electrochem. Soc.*, vol. 162, no. 14, pp. A2406–A2423, 2015.

[95] K. Yoshida, M. Nakamura, Y. Kazue, N. Tachikawa, S. Tsuzuki, S. Seki, K. Dokko, M. Watanabe, "Oxidative-stability enhancement and charge transport mechanism in glyme-lithium salt equimolar complexes," in *J. Am. Chem. Soc.*, vol. 133, no. 33, pp. 13121–13129, 2011.

[96] S. Jiao, X. Ren, R. Cao, M.H. Engelhard, Y. Liu, D. Hu, D. Mei, J. Zheng, W. Zhao,

Q. Li, *et al.*, "Stable cycling of high-voltage lithium metal batteries in ether electrolytes," in *Nat. Energy*, vol. 3, no. 9, pp. 739–746, 2018.

[97] L. Suo, Y.S. Hu, H. Li, M. Armand, L. Chen, "A new class of Solvent-in-Salt electrolyte for high-energy rechargeable metallic lithium batteries," in *Nat. Commun.*, vol. 4, p. 1481, 2013.

[98] J. Qian, W.A. Henderson, W. Xu, P. Bhattacharya, M. Engelhard, O. Borodin, J.G. Zhang, "High rate and stable cycling of lithium metal anode," in *Nat. Commun.*, vol. 6, p. 6362, 2015.

[99] Q. Ma, Z. Fang, P. Liu, J. Ma, X. Qi, W. Feng, J. Nie, Y.S. Hu, H. Li, X. Huang, *et al.*, "Improved Cycling Stability of Lithium-Metal Anode with Concentrated Electrolytes Based on Lithium (Fluorosulfonyl)(trifluoromethanesulfonyl)imide," in *ChemElectroChem*, vol. 3, no. 4, pp. 531–536, 2016.

[100] X. Fan, L. Chen, X. Ji, T. Deng, S. Hou, J. Chen, J. Zheng, F. Wang, J. Jiang, K. Xu, *et al.*, "Highly Fluorinated Interphases Enable High-Voltage Li-Metal Batteries," in *Chem*, vol. 4, no. 1, pp. 174–185, 2018.

[101] J. Liu, Z. Bao, Y. Cui, E.J. Dufek, J.B. Goodenough, P. Khalifah, Q. Li, B.Y. Liaw, P. Liu, A. Manthiram, *et al.*, "Pathways for practical high-energy long-cycling lithium metal batteries," in *Nat. Energy*, vol. 4, no. 3, pp. 180–186, 2019.

[102] S. Chen, J. Zheng, D. Mei, K.S. Han, M.H. Engelhard, W. Zhao, W. Xu, J. Liu, J.G. Zhang, "High-Voltage Lithium-Metal Batteries Enabled by Localized High-Concentration Electrolytes," in *Adv. Mater.*, vol. 30, no. 21, p. 1706102, 2018.

[103] X. Ren, S. Chen, H. Lee, D. Mei, M.H. Engelhard, S.D. Burton, W. Zhao, J. Zheng, Q. Li, M.S. Ding, *et al.*, "Localized High-Concentration Sulfone Electrolytes for High-Efficiency Lithium-Metal Batteries," in *Chem*, vol. 4, no. 8, pp. 1877–1892, 2018.

[104] S. Chen, J. Zheng, L. Yu, X. Ren, M.H. Engelhard, C. Niu, H. Lee, W. Xu, J. Xiao, J. Liu, *et al.*, "High-Efficiency Lithium Metal Batteries with Fire-Retardant Electrolytes," in *Joule*, vol. 2, no. 8, pp. 1548–1558, 2018.

[105] S. Lin, H. Hua, Z. Li, J. Zhao, "Functional Localized High-Concentration Ether-Based Electrolyte for Stabilizing High-Voltage Lithium-Metal Battery," in *ACS*

Appl. Mater. Interfaces, vol. 12, no. 30, pp. 33710–33718, 2020.

[106] X.B. Cheng, C. Yan, X. Chen, C. Guan, J.Q. Huang, H.J. Peng, R. Zhang, S.T. Yang, Q. Zhang, "Implantable Solid Electrolyte Interphase in Lithium-Metal Batteries," in *Chem*, vol. 2, no. 2, pp. 258–270, 2017.

[107] G. Ma, Z. Wen, M. Wu, C. Shen, Q. Wang, J. Jin, X. Wu, "A lithium anode protection guided highly-stable lithium-sulfur battery," in *Chem. Commun.*, vol. 50, no. 91, pp. 14209–14212, 2014.

[108] Y.J. Zhang, W. Wang, H. Tang, W.Q. Bai, X. Ge, X.L. Wang, C.D. Gu, J.P. Tu, "An ex-situ nitridation route to synthesize Li3N-modified Li anodes for lithium secondary batteries," in *J. Power Sources*, vol. 277, pp. 304–311, 2015.

[109] N.W. Li, Y.X. Yin, C.P. Yang, Y.G. Guo, "An Artificial Solid Electrolyte Interphase Layer for Stable Lithium Metal Anodes," in *Adv. Mater.*, vol. 28, no. 9, pp. 1853–1858, 2016.

[110] H.K. Jing, L.L. Kong, S. Liu, G.R. Li, X.P. Gao, "Protected lithium anode with porous Al2O3 layer for lithium-sulfur battery," in *J. Mater. Chem. A*, vol. 3, no. 23, pp. 12213–12219, 2015.

[111] A.C. Kozen, C.F. Lin, A.J. Pearse, M.A. Schroeder, X. Han, L. Hu, S.B. Lee, G.W. Rubloff, M. Noked, "Next-Generation Lithium Metal Anode Engineering via Atomic Layer Deposition," in *ACS Nano*, vol. 9, no. 6, pp. 5884–5892, 2015.

[112] L. Chen, J.G. Connell, A. Nie, Z. Huang, K.R. Zavadil, K.C. Klavetter, Y. Yuan, S. Sharifi-Asl, R. Shahbazian-Yassar, J.A. Libera, *et al.*, "Lithium metal protected by atomic layer deposition metal oxide for high performance anodes," in *J. Mater. Chem. A*, vol. 5, no. 24, pp. 12297–12309, 2017.

[113] Y. Zhang, T.T. Zuo, J. Popovic, K. Lim, Y.X. Yin, J. Maier, Y.G. Guo, "Towards better Li metal anodes: Challenges and strategies," in *Mater. Today*, vol. 33, pp. 56–74, 2020.

[114] C. Monroe, J. Newman, "The Impact of Elastic Deformation on Deposition Kinetics at Lithium/Polymer Interfaces," in *J. Electrochem. Soc.*, vol. 152, no. 2, pp. A396–A404, 2005.

[115] B. V. Lotsch, J. Maier, “Relevance of solid electrolytes for lithium-based batteries: A realistic view,” in *J. Electroceramics*, vol. 38, no. 2–4, pp. 128–141, 2017.

[116] Z. Zhang, Y. Shao, B. Lotsch, Y.S. Hu, H. Li, J. Janek, L.F. Nazar, C.W. Nan, J. Maier, M. Armand, *et al.*, “New horizons for inorganic solid state ion conductors,” in *Energy Environ. Sci.*, vol. 11, no. 8, pp. 1945–1976, 2018.

[117] Z. Wu, Z. Xie, A. Yoshida, Z. Wang, X. Hao, A. Abudula, G. Guan, “Utmost limits of various solid electrolytes in all-solid-state lithium batteries: A critical review,” in *Renew. Sustain. Energy Rev.*, vol. 109, pp. 367–385, 2019.

[118] A. Nyman, M. Behm, G. Lindbergh, “Electrochemical characterisation and modelling of the mass transport phenomena in LiPF6-EC-EMC electrolyte,” in *Electrochim. Acta*, vol. 53, no. 22, pp. 6356–6365, 2008.

[119] S. Wenzel, D.A. Weber, T. Leichtweiss, M.R. Busche, J. Sann, J. Janek, “Interphase formation and degradation of charge transfer kinetics between a lithium metal anode and highly crystalline Li7P3S11 solid electrolyte,” in *Solid State Ionics*, vol. 286, pp. 24–33, 2016.

[120] S. Wenzel, S. Randau, T. Leichtweiß, D.A. Weber, J. Sann, W.G. Zeier, J. Janek, “Direct Observation of the Interfacial Instability of the Fast Ionic Conductor Li10GeP2S12 at the Lithium Metal Anode,” in *Chem. Mater.*, vol. 28, no. 7, pp. 2400–2407, 2016.

[121] R. Koerver, I. Aygün, T. Leichtweiß, C. Dietrich, W. Zhang, J.O. Binder, P. Hartmann, W.G. Zeier, J. Janek, “Capacity Fade in Solid-State Batteries: Interphase Formation and Chemomechanical Processes in Nickel-Rich Layered Oxide Cathodes and Lithium Thiophosphate Solid Electrolytes,” in *Chem. Mater.*, vol. 29, no. 13, pp. 5574–5582, 2017.

[122] R. Kanno, M. Murayama, “Lithium Ionic Conductor Thio-LISICON: The Li2S-GeS2-P2S5 System,” in *J. Electrochem. Soc.*, vol. 148, no. 7, pp. A742–A746, 2001.

[123] Z. Liu, W. Fu, E.A. Payzant, X. Yu, Z. Wu, N.J. Dudney, J. Kiggans, K. Hong, A.J. Rondinone, C. Liang, “Anomalous high ionic conductivity of nanoporous β-Li3PS4,” in *J. Am. Chem. Soc.*, vol. 135, no. 3, pp. 975–978, 2013.

[124] S. Hori, K. Suzuki, M. Hirayama, Y. Kato, R. Kanno, “Lithium superionic conductor Li9.42Si1.02P2.1S9.96O2.04 with Li10GeP2S12-type structure in the Li2S-P2S5-SiO2 pseudoternary system: Synthesis, electrochemical properties, and structure-composition relationships,” in *Front. Energy Res.*, vol. 4, p. 28, 2016.

[125] A. Hayashi, S. Kama, F. Mizuno, K. Tadanaga, T. Minami, M. Tatsumisago, “Characterization of Li2S-P2S5 glass-ceramics as a solid electrolyte for lithium secondary batteries,” in *Solid State Ionics*, vol. 175, no. 1–4, pp. 683–686, 2004.

[126] S. Boulineau, M. Courty, J.M. Tarascon, V. Viallet, “Mechanochemical synthesis of Li-argyrodite Li 6PS 5X (X = Cl, Br, I) as sulfur-based solid electrolytes for all solid state batteries application,” in *Solid State Ionics*, vol. 221, pp. 1–5, 2012.

[127] Y. Zhu, X. He, Y. Mo, “Origin of Outstanding Stability in the Lithium Solid Electrolyte Materials: Insights from Thermodynamic Analyses Based on First-Principles Calculations,” in *ACS Appl. Mater. Interfaces*, vol. 7, no. 42, pp. 23685–23693, 2015.

[128] Y. Zhu, X. He, Y. Mo, “First principles study on electrochemical and chemical stability of solid electrolyte-electrode interfaces in all-solid-state Li-ion batteries,” in *J. Mater. Chem. A*, vol. 4, no. 9, pp. 3253–3266, 2016.

[129] W.D. Richards, L.J. Miara, Y. Wang, J.C. Kim, G. Ceder, “Interface Stability in Solid-State Batteries,” in *Chem. Mater.*, vol. 28, no. 1, pp. 266–273, 2016.

[130] R. Chen, Q. Li, X. Yu, L. Chen, H. Li, “Approaching Practically Accessible Solid-State Batteries: Stability Issues Related to Solid Electrolytes and Interfaces,” in *Chem. Rev.*, vol. 120, no. 14, pp. 6820–6877, 2020.

[131] C. Yang, K. Fu, Y. Zhang, E. Hitz, L. Hu, “Protected Lithium-Metal Anodes in Batteries: From Liquid to Solid,” in *Adv. Mater.*, vol. 29, no. 36, p. 1701169, 2017.

[132] F. Croce, L. Persi, F. Ronci, B. Scrosati, “Nanocomposite polymer electrolytes and their impact on the lithium battery technology,” in *Solid State Ionics*, vol. 135, no. 1–4, pp. 47–52, 2000.

[133] J.H. Choi, C.H. Lee, J.H. Yu, C.H. Doh, S.M. Lee, “Enhancement of ionic conductivity of composite membranes for all-solid-state lithium rechargeable

batteries incorporating tetragonal Li7La3Zr2O12 into a polyethylene oxide matrix," in *J. Power Sources*, vol. 274, pp. 458–463, 2015.

[134] T. Yang, J. Zheng, Q. Cheng, Y.Y. Hu, C.K. Chan, "Composite Polymer Electrolytes with Li7La3Zr2O12 Garnet-Type Nanowires as Ceramic Fillers: Mechanism of Conductivity Enhancement and Role of Doping and Morphology," in *ACS Appl. Mater. Interfaces*, vol. 9, no. 26, pp. 21773–21780, 2017.

[135] J. Zheng, M. Tang, Y.Y. Hu, "Lithium Ion Pathway within Li7La3Zr2O12-Polyethylene Oxide Composite Electrolytes," in *Angew. Chemie - Int. Ed.*, vol. 55, no. 40, pp. 12538–12542, 2016.

[136] B. Horstmann, J. Shi, R. Amine, M. Werres, X. He, H. Jia, F. Hausen, I. Cekic-Laskovic, S. Wiemers-Meyer, J. Lopez, *et al.*, "Strategies towards enabling lithium metal in batteries: interphases and electrodes," in *Energy Environ. Sci.*, vol. 14, no. 10, pp. 5289–5314, 2021.

[137] Z. Liang, D. Lin, J. Zhao, Z. Lu, Y. Liu, C. Liu, Y. Lu, H. Wang, K. Yan, X. Tao, *et al.*, "Composite lithium metal anode by melt infusion of lithium into a 3D conducting scaffold with lithiophilic coating," in *Proc. Natl. Acad. Sci. U. S. A.*, vol. 113, no. 11, pp. 2862–2867, 2016.

[138] Y. Zhang, W. Luo, C. Wang, Y. Li, C. Chen, J. Song, J. Dai, E.M. Hitz, S. Xu, C. Yang, *et al.*, "High-capacity, low-tortuosity, and channel-guided lithium metal anode," in *Proc. Natl. Acad. Sci. U. S. A.*, vol. 114, no. 14, pp. 3584–3589, 2017.

[139] Y. Zhang, C. Wang, G. Pastel, Y. Kuang, H. Xie, Y. Li, B. Liu, W. Luo, C. Chen, L. Hu, "3D Wettable Framework for Dendrite-Free Alkali Metal Anodes," in *Adv. Energy Mater.*, vol. 8, no. 18, p. 1800635, 2018.

[140] Y. Liu, D. Lin, Z. Liang, J. Zhao, K. Yan, Y. Cui, "Lithium-coated polymeric matrix as a minimum volume-change and dendrite-free lithium metal anode," in *Nat. Commun.*, vol. 7, p. 10992, 2016.

[141] J. Yun, B.K. Park, E.S. Won, S.H. Choi, H.C. Kang, J.H. Kim, M.S. Park, J.W. Lee, "Bottom-Up Lithium Growth Triggered by Interfacial Activity Gradient on Porous Framework for Lithium-Metal Anode," in *ACS Energy Lett.*, vol. 5, no. 10, pp. 3108–3114, 2020.

[142] K. Yan, Z. Lu, H.W. Lee, F. Xiong, P.C. Hsu, Y. Li, J. Zhao, S. Chu, Y. Cui, "Selective deposition and stable encapsulation of lithium through heterogeneous seeded growth," in *Nat. Energy*, vol. 1, no. 3, p. 16010, 2016.

[143] C. Yang, Y. Yao, S. He, H. Xie, E. Hitz, L. Hu, "Ultrafine Silver Nanoparticles for Seeded Lithium Deposition toward Stable Lithium Metal Anode," in *Adv. Mater.*, vol. 29, no. 38, p. 1702714, 2017.

[144] Q. Lu, A. Yang, A. Omar, Q. Ma, F. Tietz, O. Guillon, D. Mikhailova, "Recent Advances in Stabilization of Sodium Metal Anode in Contact with Organic Liquid and Solid-State Electrolytes," in *Energy Technol.*, vol. 10, no. 7, p. 2200149, 2022.

[145] X. Shen, H. Liu, X.B. Cheng, C. Yan, J.Q. Huang, "Beyond lithium ion batteries: Higher energy density battery systems based on lithium metal anodes," in *Energy Storage Mater.*, vol. 12, pp. 161–175, 2018.

[146] L. Wang, Z. Zhou, X. Yan, F. Hou, L. Wen, W. Luo, J. Liang, S.X. Dou, "Engineering of lithium-metal anodes towards a safe and stable battery," in *Energy Storage Mater.*, vol. 14, pp. 22–48, 2018.

[147] H. Liu, X.-B. Cheng, Z. Jin, R. Zhang, G. Wang, L.-Q. Chen, Q.-B. Liu, J.-Q. Huang, Q. Zhang, "Recent advances in understanding dendrite growth on alkali metal anodes," in *EnergyChem*, vol. 1, no. 1, p. 100003, 2019.

[148] D.P. Wilkinson, H. Blom, K. Brandt, D. Wainwright, "Effects of physical constraints on Li cyclability," in *J. Power Sources*, vol. 36, no. 4, pp. 517–527, 1991.

[149] T. Hirai, I. Yoshimatsu, J. Yamaki, "Influence of Electrolyte on Lithium Cycling Efficiency with Pressurized Electrode Stack," in *J. Electrochem. Soc.*, vol. 141, no. 3, pp. 611–614, 1994.

[150] X. Yin, W. Tang, I.D. Jung, K.C. Phua, S. Adams, S.W. Lee, G.W. Zheng, "Insights into morphological evolution and cycling behaviour of lithium metal anode under mechanical pressure," in *Nano Energy*, vol. 50, pp. 659–664, 2018.

[151] A.J. Louli, M. Genovese, R. Weber, S.G. Hames, E.R. Logan, J.R. Dahn, "Exploring the Impact of Mechanical Pressure on the Performance of Anode-Free Lithium Metal Cells," in *J. Electrochem. Soc.*, vol. 166, no. 8, pp. A1291–A1299, 2019.

[152] X. Zhang, Q.J. Wang, K.L. Harrison, K. Jungjohann, B.L. Boyce, S.A. Roberts, P.M. Attia, S.J. Harris, "Rethinking How External Pressure Can Suppress Dendrites in Lithium Metal Batteries," in *J. Electrochem. Soc.*, vol. 166, no. 15, pp. A3639–A3652, 2019.

[153] C. Zhang, Y. Liu, X. Jiao, S. Xiong, J. Song, "In Situ Volume Change Studies of Lithium Metal Electrode under Different Pressure," in *J. Electrochem. Soc.*, vol. 166, no. 15, pp. A3675–A3678, 2019.

[154] W. Chang, T. Xu, D. Steingart, "Chemo-Mechanical Effects of Stack Pressure and Temperature on Anode-Free Lithium Metal Batteries," in *J. Electrochem. Soc.*, vol. 169, p. 090530, 2022.

[155] K.L. Harrison, S. Goriparti, L.C. Merrill, D.M. Long, B. Warren, S.A. Roberts, B.R. Perdue, Z. Casias, P. Cuillier, B.L. Boyce, *et al.*, "Effects of Applied Interfacial Pressure on Li-Metal Cycling Performance and Morphology in 4 M LiFSI in DME," in *ACS Appl. Mater. Interfaces*, vol. 13, no. 27, pp. 31668–31679, 2021.

[156] D. Wainwright, R. Shimizu, "Forces generated by anode growth in cylindrical Li/MoS2 cells," in *J. Power Sources*, vol. 34, no. 1, pp. 31–38, 1991.

[157] C. Peabody, C.B. Arnold, "The role of mechanically induced separator creep in lithium-ion battery capacity fade," in *J. Power Sources*, vol. 196, no. 19, pp. 8147–8153, 2011.

[158] J. Cannarella, C.B. Arnold, "Ion transport restriction in mechanically strained separator membranes," in *J. Power Sources*, vol. 226, pp. 149–155, 2013.

[159] C. Xu, Z. Ahmad, A. Aryanfar, V. Viswanathan, J.R. Greer, "Enhanced strength and temperature dependence of mechanical properties of Li at small scales and its implications for Li metal anodes," in *Proc. Natl. Acad. Sci. U. S. A.*, vol. 114, no. 1, pp. 57–61, 2017.

[160] L. Zhang, T. Yang, C. Du, Q. Liu, Y. Tang, J. Zhao, B. Wang, T. Chen, Y. Sun, P. Jia, *et al.*, "Lithium whisker growth and stress generation in an in situ atomic force microscope–environmental transmission electron microscope set-up," in *Nat. Nanotechnol.*, vol. 15, no. 2, pp. 94–98, 2020.

[161] P.M. Sargent, M.F. Ashby, "Deformation mechanism maps for alkali metals," in

Scr. Metall., vol. 18, no. 2, pp. 145–150, 1984.

[162] A. Masias, N. Felten, R. Garcia-Mendez, J. Wolfenstine, J. Sakamoto, “Elastic, plastic, and creep mechanical properties of lithium metal,” in *J. Mater. Sci.*, vol. 54, no. 3, pp. 2585–2600, 2019.

[163] R.W. Balluffi, R.F. Mehl, “Grain boundary diffusion mechanisms in metals,” in *Metall. Trans. A*, vol. 13, no. 12, pp. 2069–2095, 1982.

[164] A. Kapoor, R.T. Yang, C. Wong, “Surface Diffusion,” in *Catal. Rev.*, vol. 31, no. 1–2, pp. 129–214, 1989.

[165] O. Crowther, A.C. West, “Effect of electrolyte composition on lithium dendrite growth,” in *J. Electrochem. Soc.*, vol. 155, no. 11, pp. A806–A811, 2008.

[166] S.H. Park, Y.J. Lee, “Morphological control of electrodeposited lithium metal: Via seeded growth: Stepwise spherical to fibrous lithium growth,” in *J. Mater. Chem. A*, vol. 9, no. 3, pp. 1803–1811, 2021.

[167] C.-Y. Tang, S.J. Dillon, “In Situ Scanning Electron Microscopy Characterization of the Mechanism for Li Dendrite Growth,” in *J. Electrochem. Soc.*, vol. 163, no. 8, pp. A1660–A1665, 2016.

[168] A.J. Leenheer, K.L. Jungjohann, K.R. Zavadil, J.P. Sullivan, C.T. Harris, “Lithium electrodeposition dynamics in aprotic electrolyte observed in situ via transmission electron Microscopy,” in *ACS Nano*, vol. 9, no. 4, pp. 4379–4389, 2015.

[169] B.L. Mehdi, J. Qian, E. Nasybulin, C. Park, D.A. Welch, R. Faller, H. Mehta, W.A. Henderson, W. Xu, C.M. Wang, *et al.*, “Observation and quantification of nanoscale processes in lithium batteries by operando electrochemical (S)TEM,” in *Nano Lett.*, vol. 15, no. 3, pp. 2168–2173, 2015.

[170] C.-Y. Chen, T. Tsuda, Y. Oshima, S. Kuwabata, “In Situ Monitoring of Lithium Metal Anodes and Their Solid Electrolyte Interphases by Transmission Electron Microscopy,” in *Small Struct.*, vol. 2, no. 6, p. 2100018, 2021.

[171] K. Nishikawa, T. Mori, T. Nishida, Y. Fukunaka, M. Rosso, T. Homma, “In Situ Observation of Dendrite Growth of Electrodeposited Li Metal,” in *J. Electrochem. Soc.*, vol. 157, no. 11, p. A1212, 2010.

[172] K. Nishikawa, T. Mori, T. Nishida, Y. Fukunaka, M. Rosso, “Li dendrite growth and Li+ ionic mass transfer phenomenon,” in *J. Electroanal. Chem.*, vol. 661, no. 1, pp. 84–89, 2011.

[173] J. Steiger, “Mechanisms of Dendrite Growth in Lithium Metal Batteries,” doctoral dissertation, Karlsruhe Institute of Technology, 2015.

[174] K. Pfeifer, S. Arnold, J. Becherer, C. Das, J. Maibach, H. Ehrenberg, S. Dsoke, “Can Metallic Sodium Electrodes Affect the Electrochemistry of Sodium-Ion Batteries? Reactivity Issues and Perspectives,” in *ChemSusChem*, vol. 12, no. 14, pp. 3312–3319, 2019.

[175] M. Mandl, J. Becherer, D. Kramer, R. Mönig, T. Diemant, R.J. Behm, M. Hahn, O. Böse, M.A. Danzer, “Sodium metal anodes: Deposition and dissolution behaviour and SEI formation,” in *Electrochim. Acta*, vol. 354, p. 136698, 2020.

[176] J. Becherer, D. Kramer, R. Mönig, “Similarities in Lithium Growth at Vastly Different Rates,” in *ChemElectroChem*, vol. 8, no. 20, pp. 3882–3893, 2021.

[177] J. Becherer, D. Kramer, R. Mönig, “The Growth Mechanism of Lithium Dendrites and its Coupling to Mechanical Stress,” in *J. Mater. Chem. A*, no. 10, pp. 5530–5539, 2022.

[178] C.E. Shannon, “Communication in the Presence of Noise,” in *Proc. IRE*, vol. 37, no. 1, pp. 10–21, 1949.

[179] W.G. Jerome, “Confocal Digital Image Capture,” in *Basic Confocal Microscopy*, 2nd ed., W.G. Jerome and R.L. Price, Eds., Cham, Switzerland: Springer, 2018, pp. 155–186.

[180] D.B. Murphy, M.W. Davidson, “Diffraction and Spatial Resolution,” in *Fundamentals of Light Microscopy and Electronic Imaging*, 2nd ed., D.B. Murphy and M.W. Davidson, Eds., Hoboken, New Jersey: Wiley-Blackwell, 2012, pp. 103–114.

[181] W. Wang, F. Chang, “A Multi-focus Image Fusion Method Based on Laplacian Pyramid,” in *J. Comput.*, vol. 6, no. 12, pp. 2559–2566, 2011.

[182] B. Lee, E. Paek, D. Mitlin, S.W. Lee, “Sodium Metal Anodes: Emerging Solutions

to Dendrite Growth," in *Chem. Rev.*, vol. 119, no. 8, pp. 5416–5460, 2019.

[183] Y. Zhang, V. Viswanathan, "Not all fluorination is the same: Unique effects of fluorine functionalization of ethylene carbonate for tuning solid-electrolyte interphase in li metal batteries," in *Langmuir*, vol. 36, no. 39, pp. 11450–11466, 2020.

[184] X. Wang, W. Zeng, L. Hong, W. Xu, H. Yang, F. Wang, H. Duan, M. Tang, H. Jiang, "Stress-driven lithium dendrite growth mechanism and dendrite mitigation by electroplating on soft substrates," in *Nat. Energy*, vol. 3, no. 3, pp. 227–235, 2018.

[185] P. Zou, Y. Sui, H. Zhan, C. Wang, H.L. Xin, H. Cheng, F. Kang, C. Yang, "Polymorph Evolution Mechanisms and Regulation Strategies of Lithium Metal Anode under Multiphysical Fields," in *Chem. Rev.*, vol. 121, no. 10, pp. 5986–6056, 2021.

[186] C. Capiglia, Y. Saito, H. Kageyama, P. Mustarelli, T. Iwamoto, T. Tabuchi, H. Tukamoto, "7Li and19F diffusion coefficients and thermal properties of non-aqueous electrolyte solutions for rechargeable lithium batteries," in *J. Power Sources*, vol. 81–82, pp. 859–862, 1999.

[187] L.O. Valøen, J.N. Reimers, "Transport Properties of LiPF6-Based Li-Ion Battery Electrolytes," in *J. Electrochem. Soc.*, vol. 152, no. 5, pp. A882–A891, 2005.

[188] K.L. Jungjohann, R.N. Gannon, S. Goriparti, S.J. Randolph, L.C. Merrill, D.C. Johnson, K.R. Zavadil, S.J. Harris, K.L. Harrison, "Cryogenic Laser Ablation Reveals Short-Circuit Mechanism in Lithium Metal Batteries," in *ACS Energy Lett.*, vol. 6, no. 6, pp. 2138–2144, 2021.

[189] Y. Li, Y. Li, A. Pei, K. Yan, Y. Sun, C.L. Wu, L.M. Joubert, R. Chin, A.L. Koh, Y. Yu, *et al.*, "Atomic structure of sensitive battery materials and interfaces revealed by cryo–electron microscopy," in *Science*, vol. 358, no. 6362, pp. 506–510, 2017.

[190] T. Yang, H. Li, Y. Tang, J. Chen, H. Ye, B. Wang, Y. Zhang, C. Du, J. Yao, B. Guo, *et al.*, "In situ observation of cracking and self-healing of solid electrolyte interphases during lithium deposition," in *Sci. Bull.*, vol. 66, no. 17, pp. 1754–1763, 2021.

[191] Y. Chen, Z. Wang, X. Li, X. Yao, C. Wang, Y. Li, W. Xue, D. Yu, S.Y. Kim, F. Yang, *et al.*, "Li metal deposition and stripping in a solid-state battery via Coble creep," in *Nature*, vol. 578, no. 7794, pp. 251–255, 2020.

[192] D. Weiss, H. Gao, E. Arzt, "Constrained diffusional creep in UHV-produced copper thin films," in *Acta Mater.*, vol. 49, no. 13, pp. 2395–2403, 2001.

[193] E. Chason, B.W. Sheldon, L.B. Freund, J.A. Floro, S.J. Hearne, "Origin of Compressive Residual Stress in Polycrystalline Thin Films," in *Phys. Rev. Lett.*, vol. 88, no. 15, p. 156103, 2002.

[194] D. Magnfält, G. Abadias, K. Sarakinos, "Atom insertion into grain boundaries and stress generation in physically vapor deposited films," in *Appl. Phys. Lett.*, vol. 103, no. 5, pp. 4–7, 2013.

[195] C.W. Pao, S.M. Foiles, E.B. Webb, D.J. Srolovitz, J.A. Floro, "Thin film compressive stresses due to adatom insertion into grain boundaries," in *Phys. Rev. Lett.*, vol. 99, no. 3, pp. 036102-1–4, 2007.

[196] J. Leib, R. Mönig, C. V. Thompson, "Direct evidence for effects of grain structure on reversible compressive deposition stresses in polycrystalline gold films," in *Phys. Rev. Lett.*, vol. 102, no. 25, p. 256101, 2009.

[197] Y. He, X. Ren, Y. Xu, M.H. Engelhard, X. Li, J. Xiao, J. Liu, J.G. Zhang, W. Xu, C. Wang, "Origin of lithium whisker formation and growth under stress," in *Nat. Nanotechnol.*, vol. 14, no. 11, pp. 1042–1047, 2019.

[198] B.Z. Lee, D.N. Lee, "Spontaneous growth mechanism of tin whiskers," in *Acta Mater.*, vol. 46, no. 10, pp. 3701-3714, 1998.

[199] G. Wulff, "XXV. Zur Frage der Geschwindigkeit des Wachsthums und der Auflösung der Krystallflächen," in *Zeitschrift für Krist. - Cryst. Mater.*, vol. 34, no. 1–6, p. 449, 1901.

[200] Y.X. Zhan, P. Shi, X.Q. Zhang, F. Ding, J.Q. Huang, Z. Jin, R. Xiang, X. Liu, Q. Zhang, "The Insights of Lithium Metal Plating/Stripping in Porous Hosts: Progress and Perspectives," in *Energy Technol.*, vol. 9, no. 2, p. 2000700, 2021.

[201] J. Zheng, M.S. Kim, Z. Tu, S. Choudhury, T. Tang, L.A. Archer, "Regulating

electrodeposition morphology of lithium: Towards commercially relevant secondary Li metal batteries," in *Chem. Soc. Rev.*, vol. 49, no. 9, pp. 2701–2750, 2020.

[202] H. Yang, C. Guo, A. Naveed, J. Lei, J. Yang, Y. Nuli, J. Wang, "Recent progress and perspective on lithium metal anode protection," in *Energy Storage Mater.*, vol. 14, pp. 199–221, 2018.

[203] P. Barai, K. Higa, V. Srinivasan, "Impact of External Pressure and Electrolyte Transport Properties on Lithium Dendrite Growth," in *J. Electrochem. Soc.*, vol. 165, no. 11, pp. A2654–A2666, 2018.

[204] K.W. Desmond, E.R. Weeks, "Random close packing of disks and spheres in confined geometries," in *Phys. Rev. E - Stat. Nonlinear, Soft Matter Phys.*, vol. 80, no. 5, p. 051305, 2009.

[205] "18650 Rechargeable Battery: Sony VTC5A," Sony Energy Device Corporation, 2014, https://enerpower.de/wp/wp-content/uploads/2016/04/Specification-US18650VTC5A.pdf (accessed Nov. 04, 2021).

List of Figures

List of Tables

List of Publications

1. K. Pfeifer, S. Arnold, **J. Becherer**, C. Das, J. Maibach, H. Ehrenberg, S. Dsoke, "Can Metallic Sodium Electrodes Affect the Electrochemistry of Sodium-Ion Batteries? Reactivity Issues and Perspectives," in *ChemSusChem*, vol. 12, no. 14, pp. 3312–3319, 2019.

   The co-author Julian Becherer carried out the experiment to observe the reactivity of sodium metal and the organic electrolyte with a light microscope.

2. M. Mandl, **J. Becherer**, D. Kramer, R. Mönig, T. Diemant, R.J. Behm, M. Hahn, O. Böse, M.A. Danzer, "Sodium metal anodes: Deposition and dissolution behaviour and SEI formation," in *Electrochim. Acta*, vol. 354, p. 136698, 2020.

   The co-author Julian Becherer carried out the in situ light microscopy of the sodium electrodeposition, prepared the figures and the initial draft of the sections about the light microscopy experiments, and reviewed the full manuscript before submission.

3. **J. Becherer**, D. Kramer, R. Mönig, "Similarities in Lithium Growth at Vastly Different Rates," in *ChemElectroChem*, vol. 8, no. 20, pp. 3882–3893, 2021.

4. **J. Becherer**, D. Kramer, R. Mönig, "The Growth Mechanism of Lithium Dendrites and its Coupling to Mechanical Stress," in *J. Mater. Chem. A*, no. 10, pp. 5530–5539, 2022.

Acronyms and Symbols

Acronyms

Al	aluminum
Al_2O_3	aluminum oxide
Ar	argon
bcc	body-centered cubic
BTFE	bis(2,2,2-trifluoroethyl) ether
Cs	cesium
$CsPF_6$	cesium hexafluorophosphate
Cu	copper
CV	cyclic voltammetry
DMC	dimethyl carbonate
DME	1,2-dimethoxyethane
DOF	depth of field
DOL	1,3-dioxolane
DX	1,4-dioxane
EBSD	electron backscatter diffraction
EC	ethylene carbonate

EDOF	extended depth of field
EDX	energy dispersive X-ray
EV	electric vehicle
FEC	fluoroethylene carbonate
GB	grain boundary
GPU	graphics processing unit
H_2	hydrogen
H_2O	water
HOMO	highest occupied molecular orbital
IUPAC	International Union of Pure and Applied Chemistry
LCO	lithium cobalt oxide
LFP	lithium iron phosphate
Li	lithium
$LiAsF_6$	lithium hexafluoroarsenate
LIB	lithium-ion battery
LiBOB	lithium bis(oxalato)borate
LiDFOB	lithium difluoro(oxalato)borate
LiF	lithium fluoride
LiFSI	lithium bis(fluorosulfonyl)imide

Li_3N	lithium nitride
$LiNO_3$	lithium nitrate
LiN_xO_y	lithium oxynitride
$LiPF_6$	lithium hexafluorophosphate
Li_3PO_4	lithium phosphate
Li_2S	lithium sulfide
Li_2S_x	lithium polysulfides ($2 \leq x \leq 8$)
LiTFSI	lithium bis(trifluoromethanesulfonyl)imide
LLZO	lithium lanthanum zirconium oxide ($Li_7La_3Zr_2O_{12}$)
LMB	lithium metal battery
LMNO	lithium manganese nickel oxide
LP30	1 M $LiPF_6$ in a 1:1 volume ratio mixture of EC and DMC
LTO	lithium titanate
$NaPF_6$	sodium hexafluorophosphate
$NaClO_4$	sodium perchlorate
NCA	lithium nickel cobalt aluminum oxide
NMC	lithium nickel manganese cobalt oxide
O_2	oxygen
PC	propylene carbonate

PE	polyethylene
PEO	polyethylene oxide
PP	polypropylene
PVDF	polyvinylidene fluoride
SEI	solid-electrolyte interphase
SEM	scanning electron microscope
Si	silicon
SIB	sodium-ion battery
TEM	transmission electron microscope
tetraglyme	tetraethylene glycol dimethyl ether
triglyme	triethylene glycol dimethyl ether
VC	vinylene carbonate

Constants

F	96485.332	$\mathrm{As\,mol^{-1}}$
π	3.14159 …	

Latin Symbols and Variables

c_0	initial ion concentration in the electrolyte	$\mathrm{M = mol\,l^{-1}}$
D	salt diffusion coefficient	$\mathrm{cm^2\,s^{-1}}$

D_S	surface diffusivity	cm^2 s^{-1}
D_GB	grain boundary diffusivity	cm^2 s^{-1}
D_B	bulk diffusivity	cm^2 s^{-1}
d_max	maximum pixel size	
j	current density	mA cm^{-2}
J_lim	limiting current density	mA cm^{-2}
L	inter electrode distance	μm, mm
l	length of a needle or a loop	μm
M	magnification of an objective	
m	mass	G
n	refractive index	
NA	numerical aperture	
Q	capacity	mAh
r	*lateral resolution*	Nm
t	time	S
t_C	cationic transference number	
T_m	melting temperature	K
U_Cell	potential of electrochemical cell	mV, V
V	Volume	cm^3

z_C	cationic charge number	

Greek symbols and variables

θ	half-angle of the cone of light	°
λ	wavelength	nm
μ	shear modulus	$N\ m^{-2}$
ρ	density	$g\ cm^{-3}$
σ_S	shear stress	$N\ m^{-2}$
τ_{Sand}	Sand's time	s
ϕ	porosity	

A Appendix

A.1 Replacing the Graphite Anode by Lithium Metal: Calculations of Energy Density and Specific Energy

In Table 2.1 in Section 2.1.2 parameters of three commercially available 18650 cells analyzed by Golubkov *et al.*[53] are shown. Here, the benefits with respect to the energy density and the specific energy of replacing the graphite anode by a lithium metal anode for one exemplary cell are estimated. For this estimation, the cell with an LCO/NMC blend cathode is used and the following assumptions are made:

- The measured volume of the anode coating ($6.0\,\mathrm{cm}^3$[53]), including the pores, is replaced by a lithium film ($1.3\,\mathrm{cm}^3$, see Table 2.1 in Section 2.1.2) on the current collector.
- The same amount of lithium is additionally stored in the cathode (100 % excess lithium). To accommodate this amount of lithium and to account for not completely dense electrodeposits during charge, it is assumed that the volume should be 1.5 times larger than the initial lithium film on the current collector. Therefore, a free volume of $\Delta V = 6.0\ \mathrm{cm}^3 - 2.5 \cdot 1.3\ \mathrm{cm}^3 = 2.75\ \mathrm{cm}^3$ is generated to increase the cell capacity.
- The thickness of the cathode coating is unchanged and the additional volume is used to elongate the electrode stack (electrodes, current collectors, and separator).
- Additional pore volume in cathode and separator will be estimated and filled with additional electrolyte.
- The volume to accommodate the lithium during charge is also filled by electrolyte.
- Other components are unchanged.

When the electrode stack is elongated, the uncoated parts of the current collector do not need to increase in length. Therefore, the current collectors and separators need to be elongated with respect to the coated parts of the current collectors. For simplicity, the factor a is only calculated for the cathode although it would vary slightly for the anode. It is the ratio between the area of cathode coating and twice the area of the aluminum current collector, which is coated on both sides ($a = \frac{715\ \text{cm}^2}{2 \cdot 403\ \text{cm}^2} = 0.887$)[53]. A simplified schematic for a current collector coated on one side is shown in Figure A.1).

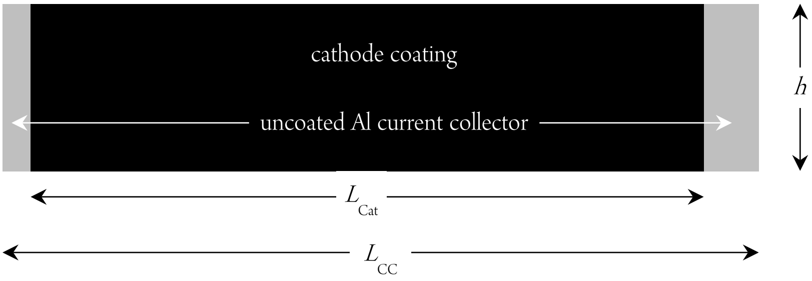

$$a = \frac{L_{\text{Cat}} \cdot h}{L_{\text{CC}} \cdot h}$$

Figure A.1: Schematic of a one-sided coated current collector.

The additional capacity ΔQ that can be stored in the free volume ΔV of 2.75 cm^3, is calculated with

$$\Delta Q = Q_0 \cdot \frac{\Delta V}{V_{\text{Stack}}} = Q_0 \cdot \frac{\Delta V}{V_{\text{cat, coat}} + 2.5 \cdot V_{\text{Li}} + a \cdot (V_{\text{Al}} + V_{\text{Cu}} + V_{\text{sep}})}\ , \tag{A.1}$$

were Q_0 is the capacity of the cell (2600 mAh) and V_{Stack} is the volume of the electrode coatings (in the charged state to accommodate the additional lithium), the coated parts of the current collectors, and the part of the separator between the coatings. $V_{\text{cat, coat}}$ is the measured volume of the cathode coating (6.5 cm^3),[53] V_{Li} is the volume of the lithium anode from Table 2.1 in Section 2.1.2 (1.3 cm^3), and V_{Al}, V_{Cu}, and V_{sep} (0.6 cm^3, 0.3 cm^3, and 1.8 cm^3)[53] are the volumes of the aluminum foil, copper foil, and separator, respectively. The additional capacity for the free volume of 2.75 cm^3 is approximately 590 mAh and hence the capacity would increase by 22.6 % when the lithium metal anode with 100 % excess lithium is used. Since graphite has an average electrode potential of 125 mV versus Li$^+$/Li,[41] the average cell voltage of ~3.8 V[53] would additionally increase by approximately 3.3 %. Therefore, the energy density of such a cell would be about 26.7 % higher than of the cell with the graphite anode. To calculate the specific energy, the mass difference of the cell with graphite anode and the cell with lithium anode and a longer electrode stack needs to be estimated:

$$\begin{aligned}
\Delta m = {} & 0.226 \cdot \big(m_{\mathrm{cat}} + m_{\mathrm{Li}} + a \cdot (m_{\mathrm{Al}} + m_{\mathrm{Cu}} + m_{\mathrm{sep}}) \\
& + (a \cdot V_{\mathrm{sep,\,pore}} + V_{\mathrm{cat,\,pore}} + 1.5 \cdot V_{\mathrm{Li}} - V_{\mathrm{an,\,pore}})) \cdot \rho_{\mathrm{electrolyte}}\big) + m_{\mathrm{Li}} - m_{\mathrm{an}} \\
= {} & 0.226 \cdot \big(m_{\mathrm{cat}} + m_{\mathrm{Li}} + a \cdot (\rho_{\mathrm{Al}} \cdot V_{\mathrm{Al}} + \rho_{\mathrm{Cu}} \cdot V_{\mathrm{Cu}} + \rho_{\mathrm{sep}} \cdot (1 - \phi_{\mathrm{sep}}) \cdot V_{\mathrm{sep}}) \\
& + (a \cdot \phi_{\mathrm{sep}} \cdot V_{\mathrm{sep}} + (V_{\mathrm{cat,\,coat}} - V_{\mathrm{cat,}}) + 1.5 \cdot V_{\mathrm{Li}} - (V_{\mathrm{an,\,coat}} - V_{\mathrm{an}})) \cdot \rho_{\mathrm{electrolyte}}\big) \\
& + m_{\mathrm{Li}} - m_{\mathrm{an}}
\end{aligned} \tag{A.2}$$

Here, the masses of the cathode m_{cat} (18.3 g), the lithium anode m_{Li} (0.7 g), and the anode m_{an} (8.1 g) are taken from Table 2.1 in Section 2.1.2 and the masses of the current collectors are calculated with their volumes and the densities ρ_{Al} = 2.7 g cm^{-3} and ρ_{Cu} = 8.96 g cm^{-3}. To calculate the mass of the separator, a density of ρ_{sep} = 0.91 g cm^{-3}, which is in the density range of PE and PP, and a porosity ϕ_{sep} of 40 % are assumed. The mass of the additional electrolyte is estimated with an assumed density of $\rho_{\mathrm{electrolyte}}$ = 1.3 g cm^{-3}, the pore volume of the separator, and the difference of the volume of the cathode coating V_{cat} and the volume of the cathode active material from Table 2.1 in Section 2.1.2 (V_{cat} = 4.0 cm^3).. With these values, the estimation in Equation (A.2) results in a mass reduction of $\Delta m \approx -1.3$ g. This results in a mass reduction of about 3 % and hence an increase in the specific energy of approximately to 30 %.

A.2 Growth During Pretreatment

During the pretreatment, the electrode grows in thickness by 5.5 μm and 3.8 μm at the upper and the lower edge, respectively. A charge of 0.5 mAh cm^{-2} is equivalent to a dense lithium film of a thickness of 2.43 μm. Taking into consideration that the deposit consists of spheres covering the copper electrode and the three-dimensional random close packing density of equal spheres, which is approximately 0.64[204], a close packed layer of spheres would correspond to a layer with a thickness of 3.8 μm. This roughly agrees with the height measurement performed by light microscopy (Figure A.2).

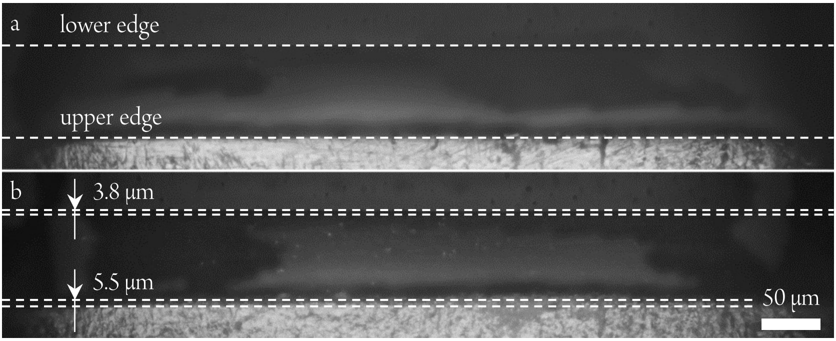

Figure A.2: Copper working electrode of exemplary cell. (a) Front of a bare copper block before and (b) after the pretreatment, consisting of the nucleation at −5 mA cm^{-2} for 30 s and the deposition of 0.5 mAh cm^{-2} lithium at −0.5 mA cm^{-2}. Cloudy appearing areas on Cu surface are artefacts of the stacking algorithm from out of focus images when the image that is in focus has low contrast in that area. The dashed lines show the lower edge of the copper electrode (directly on the cell substrate) and the upper edge of the electrode. Reprinted from Becherer *et al.*[176]

A.3 Identification of Representative Structures for SEM Investigation

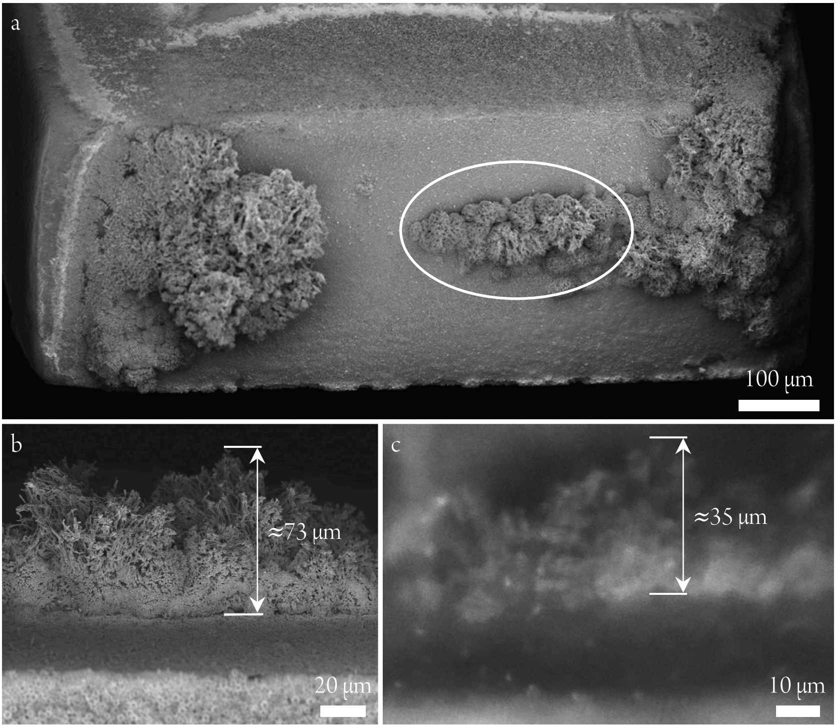

Figure A.3: (a) SEM overview image of the full copper electrode after the deposition of 5 mAh cm^{-2} lithium at −10 mA cm^{-2}. The bush on the left grew under a gas bubble and was not observed with the *operando* light microscopy. The dominating bush grew from the here shown right edge of the electrode and most of it broke off during disassembly and washing of the cell. Bushes in the middle of the electrode (surrounded by a white line) seem to be mostly intact and as observed during *operando* light microscopy. (b) SEM image of a lithium bush after the deposition of 5 mAh cm^{-2} at −10 mA cm^{-2} in top view as observed in the light microscope. (c) *Operando* light microscopy image of same bush after the deposition of 1.25 mAh cm^{-2} at −10 mA cm^{-2} before another bush blocked the view. Reprinted from Becherer *et al.*[176]

The electrode on which lithium was deposited at −10 mA cm^{-2} is shown in Figure A.3. The bushes in the middle of the electrode (highlighted in Figure A.3a) were observed during *operando* light microscopy (Figure 5.1e and in the video SV2[3] left of the gas bubble). During light microscopy, the view on this structure was blocked by the dominating bush after a deposition of 1.25 mAh cm^{-2} at −10 mA cm^{-2}. Figure A.3b and c compare the images of the bush that were taken in the SEM after disassembly and the full deposition of 5 mAh cm^{-2} at −10 mA cm^{-2} and an image from *operando* light microscopy, just before the view was blocked by the dominating bush. It can be seen that the bush height approximately doubles during the deposition of 3.75 mAh cm^{-2} after the last image stack was taken before the view was blocked. Assuming that the growth rate on this bush does not accelerate or even reduces due to the growth of the dominating bush, it is likely that nothing broke off during disassembly and washing of the electrode. Although this bush was not the bush that dominated the growth, it grew relatively fast especially during the initial phase of the deposition. Therefore, it was chosen as a representative bush for fast growth since the structure seems to be mostly intact. A further indication that the bush was intact when it was observed in the SEM is the similar outline of the bush in both images.

A.4 SEM Images of Lithium Deposits Grown at Rates Resulting in Ionic Depletion

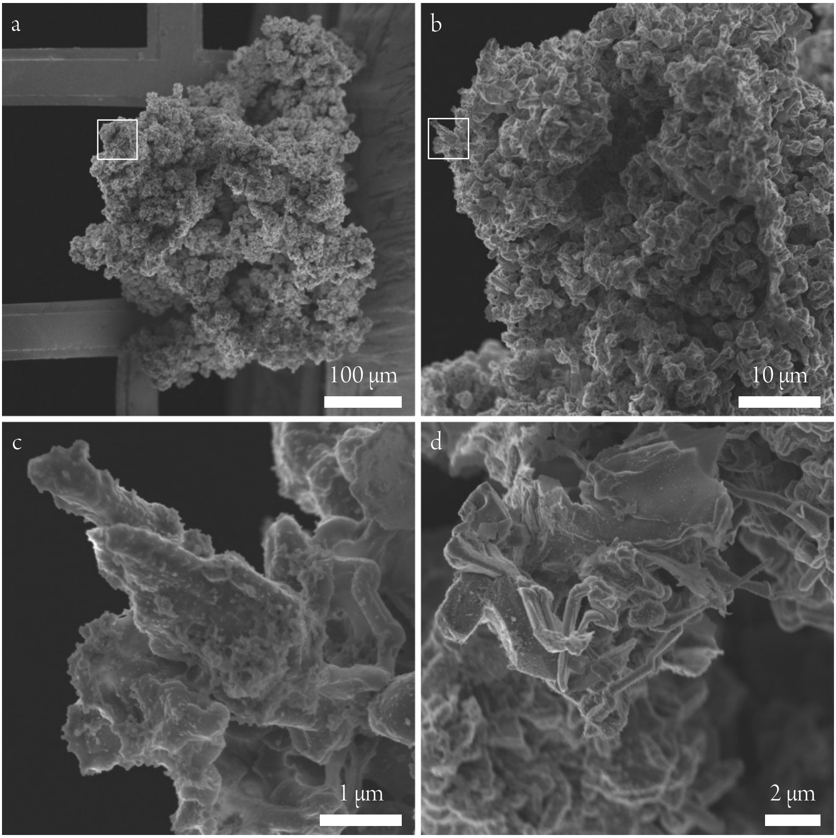

Figure A.4: SEM images of lithium deposits grown at $-50\,\mathrm{mA\,cm^{-2}}$ or $-100\,\mathrm{mA\,cm^{-2}}$. (a-c) hierarchical structure of a lithium bush on a TEM grid. The white boxes in a and b indicate the region that is shown at an about ten times higher magnification in the next image. (d) A different region of the deposits that exhibits more pronounced facets. Reprinted from Becherer *et al.*[176]

A.5 Lithium Deposition Under the Rubber Seal

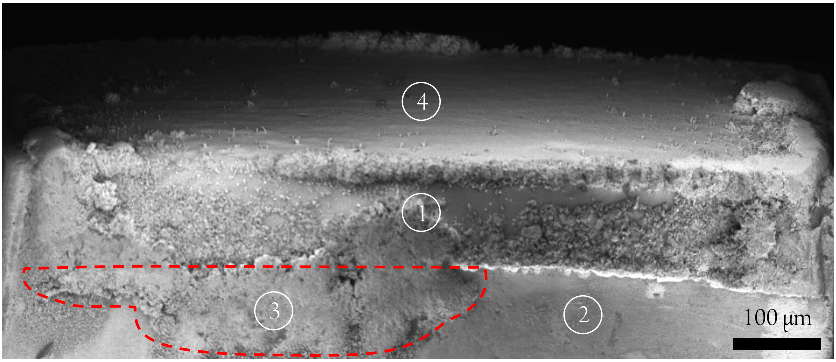

Figure A.5: Overview of the copper electrode after the deposition at a current density of $-5\,\mathrm{mA\,cm^{-2}}$. Growth under rubber block is apparent. On the right side of the block, a clear edge between the free area with lithium deposits (1) and the bare copper (2) that was protected by the rubber is visible. On the left side lithium deposits (3, surrounded by the dashed line) cover the area where the edge was expected, which clearly shows the growth under the rubber block. The lithium deposits on the front side (4), which was facing the counter electrode, is shown in the upper part of the image. Modified from Becherer *et al.*[176]

A.6 Calculation of the Limiting Current Density for a Commercial 18650 Li-Ion Cell

The calculation of the limiting current density is performed for a commercially available high-power lithium-ion cell. The cell that was chosen for this exemplary calculation is the Sony VTC5A from 2015, the data necessary for the calculation are acquired from the datasheet[205] and a publication in which the cell was further analyzed[34].

- Rated capacity: 2500 mAh[205]
- Continuous maximum charge current: 6.0 A[205]

- Cathode area: 1024 cm^2[34] (anode area was not measured but it is assume that it has a similar area)
- Separator thickness (inter-electrode distance L): 8 µm[34]

Since the electrolyte of the cell is unknown, the salt diffusion coefficient D and the cation transference number t_C are expected to be in the range of 1 M electrolytes typically used in lithium-ion batteries. Therefore, the ranges 2 … $4 \cdot 10^{-6}\ \text{cm}^2\ \text{s}^{-1}$ and 0.25 … 0.45 are used for the diffusion coefficient and the transference number, respectively.[118, 186, 187]

With the cationic charge number $z_C = 1$, the assumed initial salt concentration in the electrolyte $c_0 = 1$ M, the Faraday's constant F = 96485 As mol^{-1}, the limiting current density can be calculated with

$$J_{\text{lim}} = \frac{2 z_C c_0 F D}{L(1 - t_C)}, \text{[10, 62, 63]} \tag{A.3}$$

which results in 643 … 1754 mA cm^{-2} depending on the real electrolyte parameters. This limiting current density would be equal to a C-rate in the range between 263 C and 719 C, while the maximum continuous charge current only corresponds to 2.4 C. The tortuosity of the separator and the complex behavior of the lithium oxidation at the porous cathode were ignored for the estimation made here. However, the difference between the estimated C-rate that would correspond to the limiting current density and the maximum continuous charge current for the high-power VTC5A cell is so significant that these simplifications will most likely not change the fundamental result. The temperature has also an influence on the estimation but will also not change the result significantly. The salt diffusion coefficient changes with the temperature and reduces the limiting current density. But at 0 °C, which is the lowest recommended charge temperature for the VTC5A, the maximum continuous charge current reduces also by a factor of 1.5 to 3, depending on the upper limited charge voltage.[205] According to Valøen and Reimers[187], the salt diffusion coefficient of a typical battery electrolyte ($LiPF_6$ in PC/EC/DMC) drops to approximatly $1 \cdot 10^{-6}\ \text{cm}^2\ \text{s}^{-1}$, which is by a factor of two lower than the lowest assumed salt diffusion coefficient in the calculation above. Therefore, Sand's behavior seems even at low temperatures to be irrelevant for practical cells with liquid electrolytes.

A.7 Loop Growth

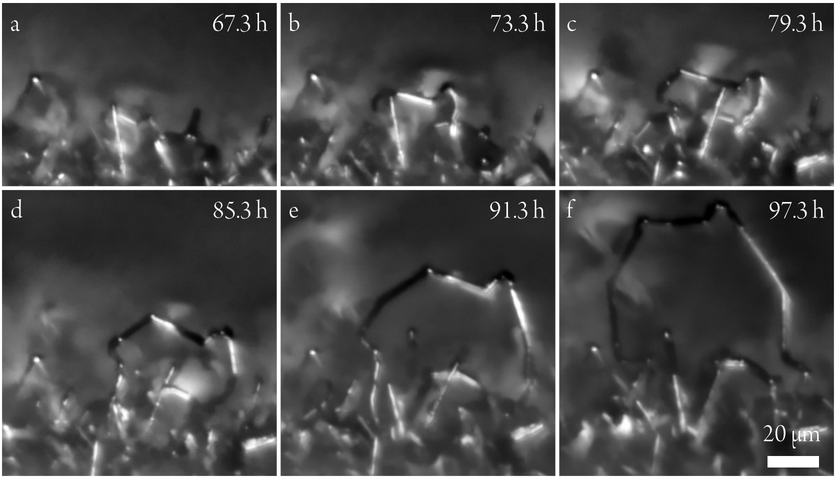

Figure A.7: (a-f) Growth of the lithium loop L1 at −0.05 mA cm^{-2} with 6 hours of deposition between the images. Figure 6.3 without markers and numbers at the kinks. Modified from Becherer *et al.*[177]

A.8 Growth of Basic Structures at −0.5 mA cm^{-2}

Figure A.8a (next page) shows the development of the length of ten needles and two loops during the deposition at −0.5 mA cm^{-2}. The evaluated needles initiated between ~1 h and 10 min and ~3 h and 10 min after the pretreatment was completed. They stopped to grow at total needle lengths varying between 9 µm and 32 µm, which is significantly shorter than the needles that grew at −0.05 mA cm^{-2}. The loops initiated later during the deposition, and they could be observed already for shorter loop length than the loops grown at −0.05 mA cm^{-2} since the needles blocking the view were shorter. Both loops grow considerably faster than the needles. Both loops reduce the growth rate significantly after approximately 8 hours, which is in good agreement with the initiation of a fast-growing bush that dominates the deposition (indicated by the red vertical line). The initiation of such fast-growing bushes was investigated in more detail in Chapter 5. Figure A.8b-e shows four images of the loop L1. The large markers of the L1-plot in Figure A.8a indicate when the images b to e were taken. The segments between the numbered kinks 5 to 7 hardly grow during the deposition. Between the first two images, the segment between kink 1 and 4 also hardly changes, but after the new kinks 3 and 2 are formed, significant growth occurs at these insertion sites. In the right part of the loop, a large number of new kinks continuously forms but hardly any long segments grow. At most of these kinks, bulges occur. These bulges are better visible in the inset in Figure A.8d with no markers.

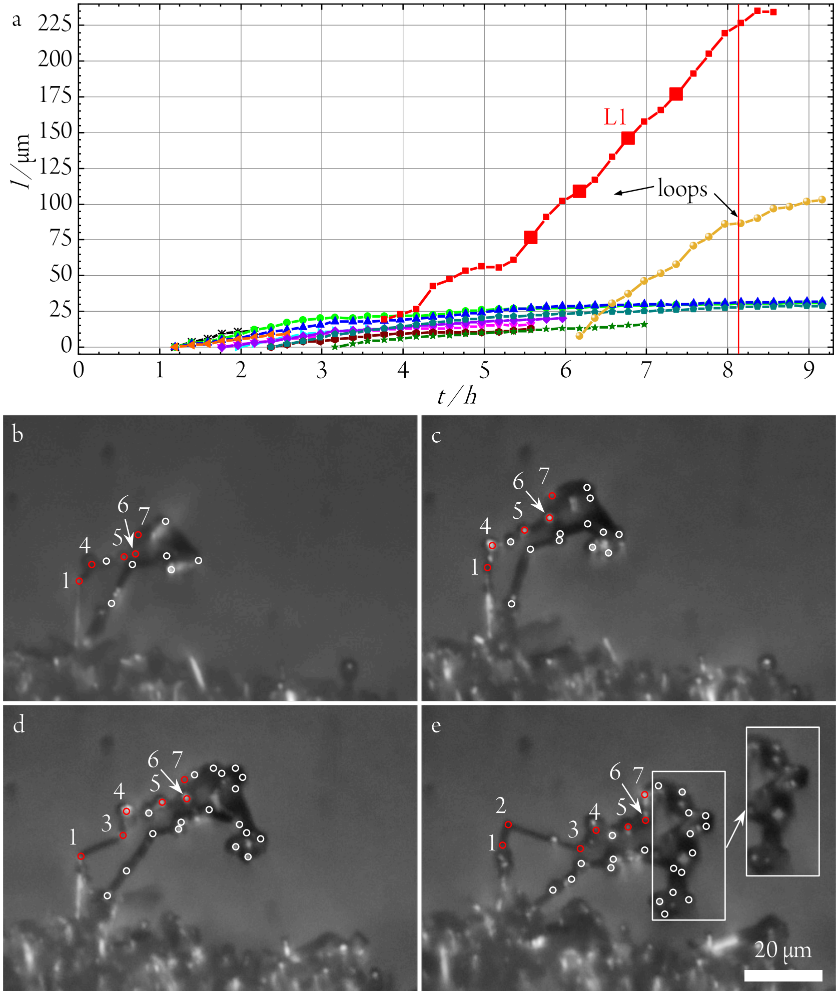

Figure A.8: (a) Length development of ten needles and two loops during the lithium electrodeposition at −0.5 mA cm^{-2}. Large markers for the loop L1 indicate when the images in the images b-e were taken. The red vertical line indicates the initiation of a fast-growing bush dominating the deposition. (b-e) Growth of the loop L1 in figure a with 36 min of deposition between the images. White circles indicate kinks of the loop; red circles indicate the numbered kinks that are referred to in the text. The number of kinks increases over time. The inset in figure e shows a part of the loop with no marks for a better visibility of the bulges. Modified from Becherer *et al.*[177]

A.9 Insertion at an Extra Half-Plane Resulting in Growth Along the Burgers Vector

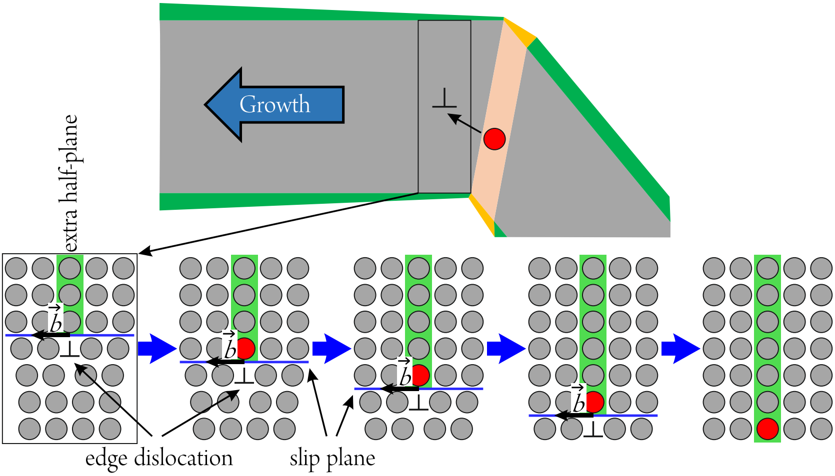

Figure A.9: Schematic illustration of growth by the climb of edge dislocations. The inserted atoms at the edge dislocation are highlighted in red, the slip plane is indicated by a blue line, and the extra half-plane is highlighted in green. Reprinted from Becherer *et al.*[177]

The lower part of Figure A.9 shows the insertion mechanism of atoms at the edge dislocation of an extra half-plane. This is known as dislocation climb. The atoms at the lower edge of the plane are inserted subsequently. In the last illustration on the right, the plane reaches the surface of the crystal and hence the defect is healed and a full new plane has grown. This results in a growth of one lattice plane along the Burgers vector $\vec{b}$, which corresponds to a $\langle 111 \rangle$ direction in bcc crystals. Plasticity due to the growth stresses may continuously generate new defects of this type, facilitating the growth in this direction.

A.10 Suggestions for Futher Experiments

The results from this thesis and the lithium deposition by thermal evaporation in vacuum shown in previous work from our group[72] indicate that the basic growth mechanism of lithium is not controlled by electrochemistry and that lithium intrinsically tends to form needles at room temperature. However, it has been shown in literature that the SEI can significantly influence the morphology of lithium electrodeposits. Furthermore, the potentially hazardous transition to the fast growth of porous bushes observed in this thesis is attributed to large-scale ruptures of the SEI. Therefore, future work could focus in more detail on the influence of the SEI by admixing additives to the commercial electrolyte LP30 used here or by comparing different electrolyte compositions during electrodeposition at various rates.

Another approach to further study the growth mechanism could be the comparison of the electrodeposition of different metals that are relevant for battery technology. Other alkali metals also have low melting points and facile diffusion can be expected. For sodium and potassium, room temperature corresponds even to 79 % and 87 % of the melting point, respectively. In contrast, alkaline earth metals have significantly higher melting points and different growth mechanisms can be expected. At room temperature, the homologous temperature of magnesium is only 0.32 and for calcium 0.26.

The growth mechanism proposed in this thesis shows a strong dependence on plastic deformation, and it is suggested that a mechanical pressure that is applied to the electrode may result in a uniform distribution of insertion sites and hence a homogeneous electrodeposition. A positive influence of stack pressure applied to LMBs has been shown in literature (Section 2.3.6). However, applying pressure to an electrode has not been combined with the *operando* observation of the electrodeposition and hence it is difficult to infer on the mechanism that yields this improved cycling behavior. A schematic cross section of an *operando* cell that combines the high-resolution light microscopy used in this thesis and external pressure applied to a lithium working electrode is shown in Figure A.10. The copper block is replaced by a second piece of lithium metal as working electrode, and instead of a

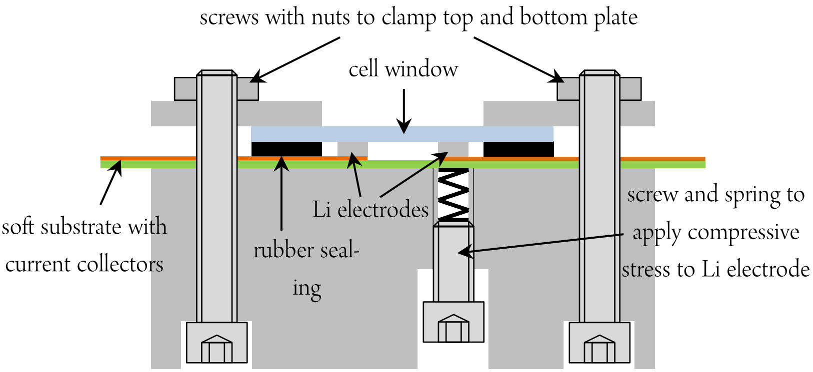

Figure A.10: Schematic illustration of the cross section of a modified *operando* cell that allows to apply mechanical stress on one of the lithium electrodes.

sapphire substrate, a soft substrate, such as a PE foil, is used. The base plate of the cell contains a screw and a spring to apply the mechanical pressure to the lithium anode through the PE substrate.

If the pressure applied in such a setup results in a more homogeneous deposition than without applying pressure, the suggested growth mechanism would be strongly supported. In contrast to experiments that apply pressure to cells, the pressure is applied directly to the electrode and perpendicular to the expected direction of growth towards the counter electrode. Therefore, the explanations for the better cycling behavior due to stack pressure found in literature (Section 2.3.6) would not apply in this experiment, while the uniform generation of insertion sites is rather independent of the direction of the applied pressure. These additional experimental studies can further augment to a fundamental understanding of the electrodeposition in metal batteries.